University of Alberta

Comparison of Time- Resolved Micromagnetic Dynamics Experiments on $Ni_{80}Fe_{20}$ and Landau-Lifshitz-Gilbert Micromagnetic Simulation

by

Gregory Edward Ballentine

A thesis submitted to the Faculty of Graduate Studies and Research in partial
fulfillment of the requirements for the degree of Doctor of Philosophy

Department of Physics

Edmonton, Alberta

Fall, 2002

University of Alberta

Library Release Form

Name of Author: Gregory Edward Ballentine

Title of Thesis: Comparison of Time Resolved Micromagnetic Dynamics Experiments on $Ni_{80}Fe_{20}$ and Landau-Lifshitz-Gilbert Micromagnetic Simulation

Degree: Doctor of Philosophy

Year this Degree Granted: 2002

Department of Physics
University of Alberta
Edmonton, Alberta, Canada
T6G 2J1

Date:

University of Alberta

Comparison of Time- Resolved Micromagnetic Dynamics Experiments on $Ni_{80}Fe_{20}$ and Landau-Lifshitz-Gilbert Micromagnetic Simulation

by

Gregory Edward Ballentine

A thesis submitted to the Faculty of Graduate Studies and Research in partial fulfillment of the requirements for the degree of Doctor of Philosophy

Department of Physics

Edmonton, Alberta

Fall, 2002

University of Alberta

Faculty of Graduate Studies and Research

The undersigned certify that they have read, and recommend to the Faculty of Graduate Studies and Research for acceptance, a thesis *entitled Comparison of Time Resolved Micromagnetic Dynamics Experiments on* $Ni_{80}Fe_{20}$ *and Landau-Lifshitz-Gilbert Micromagnetic Simulation* submitted by *Gregory Edward Ballentine* in partial fulfillment of the requirements for the degree of *Doctor of Philosophy.*

Dr. M. R. Freeman (supervisor)

Dr. W. J. McDonald (chair & examiner)

Dr. A. Meldrum (examiner)

Dr. P-N. Roy (examiner)

Dr. R. D. Sydora (examiner)

Dr. J. P. Whitehead (external examiner)

Date:

Abstract

Magnetization dynamics in lithographically patterned thin-film permalloy ($Ni_{80}Fe_{20}$) microstructures are studied using time resolved scanning Kerr microscopy (TR-SKEM). This is a technique combining ultrafast lasers with scanning probe microscopes to observe repetitive non-equilibrium dynamic magnetization states. These observations are compared to a finite element micromagnetic simulation based on the Landau-Lifshitz-Gilbert (LLG) equation. This is a stringent test for the LLG equation, as it will show how well it can reproduce experimental micromagnetics.

Micromagnetic dynamic experiments tested fall into two classes ferromagnetic resonance and magnetization reversal. Ferromagnetic resonance is a low amplitude excitation where the magnetic spins are saturated in one direction and then caused to oscillate at their resonance frequency by a transient magnetic field perpendicular to their saturation direction. Magnetization reversal is a large amplitude excitation where the spin direction in the ferromagnet changes by 180°. The same simulation with the parameters measured with our system ($4\pi M_s$=10.8 kOe and α=0.008) is quite successful in reproducing experimental behaviour.

Convergence between experimental and numerical micromagnetics is seen in many problems. One large cause of discrepancy, the non-repeatability of dynamics due to Brownian motion of magnetization vectors is studied with simulation. These simulations can be used as a guide to understand the magnetization dynamics experiments in cases where the dynamics are not repetitive.

Acknowledgements

I would like to thank Mark Freeman who has been a very good supervisor, advisor and mentor throughout my years at the University of Alberta. As well I would like to thank the members of his groups, the condensed matter groups and the department in general for their hospitality, advice, discussions, teaching and support.

I would like to thank my parents Leslie and Terry for their love and support and for raising a son with the curiosity to look at the world and ask questions.

Finally, I would like to thank Nora Munoz for her love, encouragement, support and willingness to proofread this entire document in its early stages.

Table of Contents

List of Figures

List of Symbols

α	Gilbert's damping constant
α_{ik},α_e	Bar'yaktar damping terms
β	stochastic integral parameter
χ	magnetic susceptibility
γ	gyromagnetic ratio
γ'	Landau-Lifshitz gyromagnetic ratio
Δ	domain wall width
Δt	change in time
δ	wavevector
ε	dielectric constant
η	stochastic variable
Φ_d	scalar potential from demagnetizing field
φ	generic parameter
$\phi_{m.n}$	angular coordinate
κ	term in Polder susceptibility tensor
λ	Weiss constant
λ	Landau-Lifshitz damping frequency
λ_v	volume charge density
μ	micro (x 10^{-6})
μ	permeability
μ_o	permeability of free space
μm	micrometers
π	ratio of a circle's area to squared radius
θ	angular coordinate
θ_o,θ_k	angular coordinate
σ	conductivity
σ_s	surface charge density
τ	torque
τ	time
τ,τ_s	switching time
ω	frequency
Ψ	trial wave function
ψ	scalar potential
a	lattice constant
A	exchange constant
A	initial magnetization angle
AMR	anisotropic magnetoresistance
b	time varying portion of magnetic induction
B_e	magnetic induction due to exchange
BEMM	ballistic electron magnetic microscopy
c	speed of light in a vacuum
CD	compact disk

CMR	colossal magnetorsistance
Co	cobalt
CPU	central processing unit
d	thickness
d	distance
D	displacement current
DC	direct current
e	number with a natural logarithm of one
E	electric field
exp	experiment
f	frequency
f_o	characteristic frequency
$F(\omega)$	Fourier transform
Fe_2O_3	iron oxide
FFT	fast Fourier transform
FFTW	faster Fourier transform in the west
FMR	ferromagnetic resonance
GaAs	gallium arsenide
GMR	giant magnetoresistance
$\mathbf{h}$	time varying portion of magnetic field
$\mathbf{H}$	magnetic field
$\mathbf{H_b}$	biasing magnetic field
$\mathbf{H}_d$	demagnetizing magnetic field
$\mathbf{H_{eff}}$	effective magnetic field
$\mathbf{H_i}$	induced magnetic field
$\mathbf{H}_L$	longitudinal magnetic field
$\mathbf{H_o}$	static component of magnetic field
$\mathbf{H_o}$	applied magnetic field
$\mathbf{H_T}$	transverse magnetic field
$\mathbf{H_{th}}$	thermal magnetic field
H_ϕ,H_θ	magnetic field along ϕ or θ direction
H_x	x-component of magnetic field
H_y	y-component of magnetic field
H_z	z-component of magnetic field
Hz	hertz
i	imaginary number ($\sqrt{-1}$)
I_p,I_s	incident light intensities
J	current density
J,J_{mn}	exchange integral
k	kilo ($x10^3$)
k	wavevector
k,k_B	Boltzmann’s constant
K_{ij}	demagnetizing coefficient
keV	kiloelectron volts
kHz	kilohertz
$k_{neighbour}$	number of nearest neighbours

k_u,K	uniaxial anisotropy constant
L	angular momentum
l_{ex}^A	exchange length due to anisotropy
l_{ex}^D	exchange length due to demagnetizing
LLG	Landau-Lifshitz-Gilbert
m	magnetization
m	time varying portion of magnetization
M	Mega ($x10^6$)
M,M_i,M_j	magnetization
m_D	Doring mass
MHz	megahertz
MIT	Massachusetts Institute of Technology
M_o	static component of magnetization
M_s	saturation magnetization
M_x	x-component of magnetization
M_y	y-component of magnetization
M_z	z-component of magnetization
MTJ	magnetic tunnel junction
n	surface normal
n	quantum number
n	index of refraction
N	number of cells
Nd	neodymium
nm	nanometer
ns	nanosecond
N_x,N_y,N_z	demagnetizing factors
Oe	Oersted
p	polarization state of light
P	probability
PC	photoconductive switch
ps	picoseconds
Pt	platinum
Q′	distance vector
r	position vector
r_{ij}	distance vector
R_K,R_N	reflected electric field vectors
R_p,R_s	reflected light intensities
RKKY	Ruderman-Kittel-Kasuya-Yosida
s	polarization state of light
S	surface
S,S_m,S_n	spins
Sapph	sapphire
SEM	scanning electron microscope
SGI	Silicon Graphics Incorporated
SHMOKE	second harmonic magnetoptical Kerr effect
Si	silicon

sim	simulation
SiO_2	silicon oxide
SLAC	Stanford Linear Accelerator Center
t	time
t	thickness
t_N	Neel time
T	temperature
T	switching time
T_1,T_2	Bloch-Bloembergen relaxation times
TEM	transmission electron microscope
Ti	titanium
TR-SKEM	time resolved scanning Kerr effect microscopy
v	velocity
V	voltage
V	volume
V_{LOR}	velocity of electrons due to Lorentz force
w	width
w	volume energy density
w_d	volumed demagnetizaing energy density
w_{ex}	volume exchange energy density
w_u	volume anisotropy energy density
w_z	volume Zeeman energy density
x	Cartesian coordinate
y	Cartesian coordinate
YAG	yttrium aluminum garnet
z	Cartesian coordinate
z	number of nearest neighbors

1. Magnetism

The most significant trend in electronics in the past half century is the reduction in size and increase in speed of devices. This has lead to a great deal of interest in micro [1] and nano [2] electronics and magnetism.[3] This trend is pushing our physics knowledge. Advances in fundamental magnetism research has lead to new phenomena such as giant [4] and colossal [5] magnetoresistance (GMR and CMR respectively - large changes in electrical resistance depending upon magnetization directions in the device) and oscillatory magnetic coupling (between ferromagnetic and antiferromagnetic) of ultrathin films.[6] This has opened the possibility for many new magnetoelectronic devices [7] which use the new freedom in functionality from combining both spin (magnetic) and charge (electronic) information.

1.1 Fundamental Motivations

The advances touched upon in the preceeding paragraph (GMR, CMR and oscillatory magnetic coupling) are of huge fundamental importance and each has spawned a new sub-field in physics. These are examples of the major advances that are occurring in magnetism today.

Magnetism is a phenomenon that is often studied on the mesoscale. It is an inherently quantum mechanical phenomenon (Bohr -van Leeuwen theorem) [8] but occurs in systems which are too large to give a full quantum mechanical treatment. Most of the current theoretical framework in magnetism is semi-classical. The push toward the nanoscale will test the semi-classical framework and cause it to break down in many instances. It will force the development of a newer, richer theoretical framework and it will lead to new phenomena as we see quantum mechanics on a macroscopic scale. Examples of this, which are already being studied, include spin injection [9], spin coherence [10], and quantum entanglement.[11]

Many very conceptually simple problems which still exist in magnetism. This thesis is partly devoted to the problem of how ferromagnets reverse magnetization direction.

This simple question has largely remained unanswered over the last 50 years and is an example of one of the fundamental issues remaining in magnetism.

Magnetism is a rich and often non-linear theory, with lots of possibility for advancement. Techniques used to study it often have broad application to solid state physics and material science as a whole, but are often first attempted in the "test-bed" of magnetism.

For all these reasons and more, magnetism is an area of physics which is very active and is likely to have fundamental advances in the future.

1.2 Applied Motivations

Magnetoelectronics is making a wide impact in industry. Ultrahigh density and high speed magnetic recording exist today.[12] They are being improved at very quick rates to make computer hard drives smaller, faster and able to store more information.

The read portion of a magnetic recording head has undergone significant modification recently. It has gone from an inductive reading device, to an anisotropic magnetoresistance (AMR) device, to a giant magnetoresistance (GMR) device in less than a decade. All the time it has been shrinking in size while maintaining the same absolute sensitivity.

On the write side, the challenges are material issues (for example finding high magnetic moment materials) as well as magnetic dynamic problems (such as head switching characteristics). The density of information storage (bits per square inch) has not only maintained a Moore's Law pace (shrinking in size and doubling in complexity every 18 months), it has improved from that pace due to the introduction of a GMR reader in 1997-98. Currently, 48.8 Gb/in^2 has been demonstrated in a commercial product.[13] As information gets written into smaller and smaller bits, fundamental limits are looming on the horizon. The magnetic elements in which information is stored will reach the superparamagnetic limit around 100-150 Gb/in^{2,}, where thermal fluctuations are a dominant enough energy term to switch magnetization thus destroying recorded information. In order to solve this problem, work is underway to use patterned media, media with higher anisotropy or media with increased saturation magnetization using higher moment writers, or “perpendicular” recording which allows a larger volume bit at the same areal density.

New devices like magnetic tunnel junctions (MTJ) may soon be available in magnetic RAM to challenge traditional silicon memory. MTJs are a sandwich of two ferromagnetic layers with a thin insulating layer between them, serving as a tunnelling barrier. The resistance in the tunnel barrier depends upon the magnetic arrangement of the two ferromagnetic layers. When the spins are aligned, the resistance is smaller than when they are anti-aligned. In this geometry, the currents will run perpendicular to the plane, as opposed to parallel to the plane as in traditional magnetic recording, making higher density possible. Work is also being done to adapt traditional GMR memory to use current perpendicular to the plane. The development of new memory devices involves many pressing issues regarding uniformity, reliability, reproducibility and integration into silicon processing steps, .

Fundamental changes in computer architecture may occur if magnetic memory and semiconductor logic can be better integrated into spintronic devices. Topics such as spin transport, spin injection and possibly spin transistors [14] must be addressed for this to happen.

1.3 Ferromagnetism

Ferromagnets have a spontaneous magnetic moment, even in zero applied magnetic field. The spontaneous magnetic moment suggests that electron spins and magnetic moments are arranged in a regular manner. Weiss [15] gave the first explanation of this using the mean field approximation. He proposed that each magnetic atom experiences a field proportional to the magnetization

$$B_e = \lambda M \tag{1.1}$$

where λ is a constant, independent of temperature. This is the earliest formulation of what today is known as the exchange field. This formulation is very successful in explaining the saturation magnetization of the ferromagnet as a function of temperature.

Above a critical temperature, known as the Curie temperature, the spontaneous magnetization vanishes and the sample “separates” into a disordered paramagnetic state.

Weiss also postulated that a ferromagnetic material breaks up into microscopic domains where each domain has a spontaneous magnetization but is oriented in different directions, so that on the macroscale the magnetization is lower than the saturation magnetization. This is due to the competition between the energy of the free magnetic poles on the sample surface (known as demagnetization) and the exchange interaction that tends to align spins. The demagnetizing energy terms depend upon volume, so it takes a larger number of spins for them to become important. Thus on the microscopic scale, the magnetization tends to be aligned, but on the macroscopic scale it tends to be demagnetized. In a full micromagnetic analysis, other energy terms are also relevant. Energy minimization is what determines in which static state a ferromagnetic material will be found.

The Weiss theory is semi-classical and is necessary in part due to the Bohr- van Leeuwen theorem.[8] This theorem is rather technical and uses Maxwell’s equations and statistical mechanics (the grand canonical ensemble) for classical non-relativistic electrons. It shows that at any finite temperature and in all finite applied electrical or thermal fields, the net magnetization of a collection of electrons vanishes identically. This is an example of a large conflict between experiment and theory. It is resolved only with quantum mechanics, as the quantized nature of the electron’s orbital magnetic moments allows for magnetization to exist. However, ferromagnetic samples are sufficiently complex that the problem becomes far too large to treat purely quantum mechanically, hence the need for a mesoscopic semi-classical theory.

1.4 Micromagnetization Dynamics

The semi-classical theory used to solve micromagnetization dynamics problems uses Newtonian physics with only as much quantum mechanics as necessary to capture the underlying mechanisms. As a starting point we have Newton’s second law:

$$\frac{d\mathbf{L}}{dt} = \boldsymbol{\tau} \tag{1.2}$$

where **L** is angular momentum, t is time and **τ** is torque. In a magnetic system this can be written as

$$-\frac{d\mathbf{M}}{\gamma dt} = \mathbf{M} \times \mathbf{H} \,. \tag{1.3}$$

Here **M** is the magnetization which is constant in magnitude but may vary in direction, **H** is the effective magnetic field and γ is the gyromagnetic ratio. This equation will lead to an infinite precession of spins in the magnet, so it must be modified to include damping. The simplest possible assumption is that the damping is linear and isotropic. This assumption has been used successfully in many aspects of magnetoelectronics. This leads to a damping term proportional to change in magnetization d**M**/dt with a strength given by α, a linear damping constant. This leads to an equation of form

$$\frac{d\mathbf{M}}{dt} = -\gamma(\mathbf{M} \times \mathbf{H}) + \frac{\alpha}{M_s}\mathbf{M} \times \frac{d\mathbf{M}}{dt} \tag{1.4}$$

here M_s is the scalar value of the magnetization, known as the saturation magnetization. This is the form of the Landau-Lifshitz-Gilbert (LLG) [16] equation that is usually given in publications. An equivalent form is the original Landau-Lifshitz [17] equation.

$$\frac{d\mathbf{M}}{dt} = -\gamma'(\mathbf{M} \times \mathbf{H}) - \frac{\lambda}{M_s^{\,2}}\mathbf{M} \times (\mathbf{M} \times \mathbf{H}) \tag{1.5}$$

These equations are equivalent if we make the following substitutions

$$\alpha = \frac{\lambda}{\gamma' M_s} \qquad\qquad \gamma = \gamma'(1+\alpha^2) \tag{1.6}$$

The original equation was initially derived assuming low damping without the substitution for γ. This equation is not physical for higher damping. The correspondence between the two forms of the equation was discovered later.[18]

In order to do calculations it is often necessary to write **H** in terms of the magnetization **M**. This is easily accomplished by noting that **H** is the energy variational with magnetization

$$\mathbf{H} = -\frac{\delta w}{\delta \mathbf{M}} \tag{1.7}$$

where w is the volume energy density, and this derivative is a functional derivative which is defined by

$$\frac{\delta w}{\delta M_x} = \frac{\partial w}{\partial M_x} - \nabla \bullet \frac{\partial w}{\partial \nabla M_x} \tag{1.8}$$

When the LLG equation is written in this way, the problem of which energy terms are part of w becomes clear. Typically four terms are used. They are Zeeman, exchange, demagnetizing and anisotropy energy terms. A fifth term, thermal energy in the system, is described later on in this thesis.

This equation is complex and non-linear. Except in special cases, exact calculation is not possible. Since it has four competing energy terms, none of which can be neglected, approximate analytical calculation is also not possible. Thus, this problem must be solved by a numerical simulation.

1.4.1 Zeeman energy

Zeeman energy is the energy from the coupling of spins within the magnet to the external magnetic field. It is more energetically favourable for spins to align with applied field than to point in other directions. This term is

$$w_z = \frac{-\int \mathbf{M} \bullet \mathbf{H} \mathbf{dV}}{V} \tag{1.9}$$

1.4.2 Exchange energy

The exchange interaction is a quantum mechanical interaction that arises from the overlap of electronic charge distributions. Depending upon the material, the exchange interaction is due to electronic orbital overlap of neighbouring atoms directly or mediated by conduction electrons [19] (this is called the RKKY interaction or indirect exchange), or mediated by intervening non-magnetic ions (called superexchange) . In general the exchange interaction can be written as

$$w_{ex} = -\frac{1}{V} \sum_{\langle m,n \rangle} J_{mn} \mathbf{S_m} \bullet \mathbf{S_n} \tag{1.10}$$

where J_{mn} is a quantum mechanical coefficient known as the exchange integral and $\mathbf{S_m}$ and $\mathbf{S_n}$ are the spin directions of the mth and nth atoms and V is the volume of the material. This is known as the Heisenberg Hamiltonian.[20] Much work has been done solving it in many body situations, although mesoscopic magnetism involves too many bodies to approach it in this manner. The magnitude and sign of the exchange integral J_{mn} is in general a function of the electronic structure of the ions and the distance between them. Two simple cases can be considered. The case where J_{mn} is everywhere positive will lead to a minimization in energy where all spins point in the same direction. This is the case of a ferromagnet. When J_{mn} is everywhere negative, the energy minimization will have all spins pointing anti-parallel to their nearest neighbours. This is the case of an antiferromagnet.

Often to do micromagnetic calculations, it is cumbersome to evaluate exchange energy because it involves a discrete calculation and not a continuous one. This problem is solved by assuming that all vectors and properties of the sample are continuous. Then we can write

$$-\sum_{\langle m,n\rangle} J_{mn}\mathbf{S_m}\bullet\mathbf{S_n} \Rightarrow -JS^2\sum_{\langle m,n\rangle}\cos\phi_{m,n} \tag{1.11}$$

where $\varphi_{m,n}$ is the angle between the mth and nth spins. In a ferromagnet where spins are mostly aligned, we can assume φ is small so that $\cos\varphi \to 1-1/2\varphi^2$. Since we will eventually take the derivative of the energy we can neglect the constant term giving us

$$JS^2\sum_{m,n}\phi_{mn}^{\;2} \tag{1.12}$$

We can make further assumptions about φ_{mn} as shown

$$\phi_{mn}^{\;2} \cong \left|\mathbf{M_m}-\mathbf{M_n}\right|^2 \cong \left|\mathbf{r_{mn}}\bullet\nabla\mathbf{M}\right|^2 = \mathrm{a}^2\left[\nabla M_x^{\;2}+\nabla M_y^{\;2}+\nabla M_z^{\;2}\right] \tag{1.13}$$

where a is the mean distance between atoms (the lattice constant) and M is the direction of (classical) magnetization of the spins. This gives us an exchange energy density

$$w_{ex} = \frac{JS^2k_{neighbour}}{a}\left[\nabla M_x^{\;2}+\nabla M_y^{\;2}+\nabla M_z^{\;2}\right] \tag{1.14}$$

where $k_{neighbour}$ is the number of nearest neighbours each atom has. Usually the quantity $JS^2k_{neighbour}/a$ is defined as an exchange constant A.

Now that we have a semi-classical continuum model for exchange we can include several empirical effects into it, such as crystallinity. Local exchange values will decrease around grain boundaries. Usually when exchange is reported in the literature both a crystalline and an (average) polycrystalline value are quoted. In the simulation we generally use a polycrystalline value as our samples are polycrystal.

In the ensuing simulation, exchange will be calculated with nearest neighbours only. Other cells are taken as being far enough apart to make it negligible. Also, since this thesis deals with ferromagnets, J_{mn} is taken to be everywhere positive with a constant value.

1.4.3 Demagnetizing Energy

Demagnetizing energy is the self-energy of the sample. It is the energy of each spin due to the presence of all the other spins. It is mathematically complex to calculate and most of the computation time in simulations is spent computing it. This is because one needs to know the spin configuration of the entire sample to calculate this term for any one spin, thus making the problem non-local. In general, this term is calculated by solving Maxwell's equations. If we start from the equation

$$\nabla \bullet \mathbf{B} = \nabla \bullet (\mu_o \mathbf{H} + \mathbf{M}) = 0\,, \qquad (1.15)$$

and we define the demagnetizing field $\mathbf{H_d}$ to be the field generated by a magnetization $\mathbf{M}$ then

$$\nabla \bullet H_d = -\nabla \bullet \left(\frac{\mathbf{M}}{\mu_0} \right). \qquad (1.16)$$

The sources and sinks of the magnetization act like positive and negative "magnetic charges" for the stray field. This field can be calculated the same way an electric field is calculated in electrostatics, with the only difference being that magnetic charges never appear isolated, since they are always balanced by opposite charges.

The energy of the demagnetizing field can be written down as

$$W_d = \frac{1}{2V}\mu_o \int_{all-space} H_d{}^2 dV = -\frac{1}{2V} \int_{sample} \mathbf{H_d} \bullet \mathbf{M} dV \qquad (1.17)$$

The first integral shows that demagnetizing field energy is always positive, unless $\mathbf{H_d}$ is everywhere zero (in which case the demagnetizing field energy is also zero). The second integral, which is mathematically equivalent for a finite sample, is usually easier to evaluate, since it extends over a finite region. However, calculating these integrals is not simple, and will be discussed in detail later in chapter three.

1.4.4 Anisotropy Energy

Real crystals have directions that are energetically favourable for spins to be aligned and other directions that are unfavourable. This effect is called magnetocrystalline anisotropy. This may be induced or due to spin-orbit coupling. Usually, the induced anisotropy is the larger of the two, and can be controlled by the film growth. This anisotropy is induced by strain in the film or by directional growth (possibly caused by growing the film in a magnetic field). Phenomenologically, this anisotropy is fitted to an energy relation. Most commonly, when a sample has uniaxial anisotropy (one axis that is energetically favourable over all others) the relation used is

$$W_u = K_u \sin^2\theta \qquad (1.18)$$

where K_u is a uniaxial anisotropy constant and θ is the angle from the preferred direction of magnetization or the “easy axis”.

1.5 Magnetostatics and Dynamics – a history

Magnetic switching was first studied statically or quasi-statically. Work in this field has always had industrial pressure pushing it. A good treatise on the subject is Doyle [21], and much of this is also summarized in Hiebert.[22] It has always been an interesting fundamental problem. Much of the work has attempted to answer the question "What happens the instant that the magnetic field is too strong and equilibrium is overcome?" It turns out that this question is complex and still cannot be fully answered today.

Analytic calculation has had some limited success in answering this question.[23] Among the possible reversal mechanisms, only the lowest energy trajectory will happen. This can be illustrated with the calculation of the magnetization reversal of an infinite cylinder initially magnetized along its length. Two modes of rotation of the magnetization are found to be possible. There is the coherent rotation mode ("rotation in unison") where the magnetization in the cylinder rotates in the same angle everywhere, and the "curling" mode where the magnetization reversal nucleates by developing a small component along the azimuthal direction of the cylinder. At a critical radius in the cylinder, there is a crossover in the nature of the lowest energy mode. The curling mode occurs for larger radius cylinders and the coherent mode for smaller radius ones. Further nucleation calculations have been done in other geometries.[24] These are "static" magnetization calculations. Gyrotropic effects (dynamic magnetization effects) must be taken care of to get a full picture of magnetization reversal.

One well-studied example of a localized gyrotropic effect is domain wall motion. Sixtus and Tonks [25] first investigated domain wall motion in a ferromagnetic wire. Their idea was that reversal occurred through domain walls sweeping through a material.

Domain walls have long been studied theoretically. One of the first uses of the Landau-Lifshitz equation [16] was to derive a domain wall mobility formula given by

$$\mathbf{v} = \frac{\gamma\Delta}{\alpha}\mathbf{H} \tag{1.19}$$

where v is the velocity of the wall and Δ is the domain wall width. This formula assumes that the shape of the wall does not change over time. It provides a method for the measurement of the damping constant α by measuring the ratio of v to H. In the case where the domain wall shape is allowed to change with time, this value is an upper bound to the domain wall mobility ($\equiv\gamma\Delta/\alpha$). Since field is proportional to velocity, switching time will be proportional to field when switching is driven by domain wall movement. An effective domain wall mass can also be derived using energy considerations. The motion of the wall can be viewed as an effective inertial object moving viscously through the spins in the sample, where the wall has a mass

$$m_D = \frac{1+\alpha^2}{2\pi\gamma^2\Delta} \tag{1.20}$$

where m_D is called Doring mass.[26] This calculation is only applicable in the case of low velocity. The velocity of a domain wall can increase up to a critical velocity known as the Walker breakdown velocity (or the Walker limit [27])

$$v_W = 2\pi\gamma\Delta M_s \tag{1.21}$$

For fields that exceed this limit, the domain wall is believed to begin oscillations, although this has not been directly observed.

More complex dynamics studies began in earnest in the late 1950's. In depth "first looks" at magnetic switching began at this time. People began to explore the situation where the sample was subjected to fields that were so strong that domain wall motion alone was too slow to bring about the new equilibrium conditions. Coherent and

Figure 1.1 The Stoner-Wohlfarth astroid. The curve dineates the crossover from stable to unstable equilibria. For any field outside the curve there is one stable equilibrium position. For any field inside the curve there are two unstable equilibria values. Point B has two equilibria, M_1 and M_2. Point A only has one equilibria, M_1.

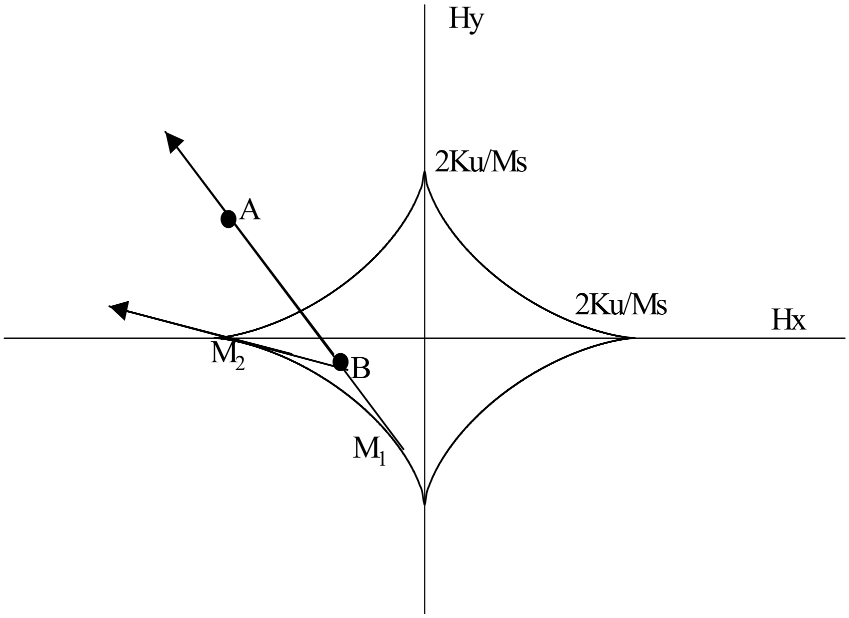

incoherent rotation were first studied experimentally. Coherent rotation was considered to be just a variant upon the rotation in unison that had been analyzed in the cylinder problem. Incoherent rotation was a more complicated, non-equilibrium magnetization pattern where some spins rotated in one direction and others rotated in another direction.

The Stoner-Wohlfarth theorem [28] was constructed for analysis of the coherent reversal of a single domain symmetric object with uniaxial anisotropy. These simplifications allowed for the neglect of complex energy terms, since there is no spatial variation in them across the sample. Symmetry allows for demagnetizing energy to be neglected and the single domain nature allows exchange energy to be neglected. Including only the Zeeman and anisotropy terms, in the case of a two dimensional thin film, the total volume energy density could be written as

$$w = -M_s H_x \cos\theta - M_s H_y \sin\theta + K_u \sin^2\theta \tag{1.22}$$

where θ is the angle between the easy axis and the magnetization. This can be minimized with respect to θ and set to zero to give the equilibrium angle

$$\frac{\partial w}{\partial \theta} = M_s H_x \sin\theta - M_s H_y \cos\theta + 2K_u \sin\theta\cos\theta = 0 \tag{1.23}$$

The second derivative is set to zero to give the transition between stable and unstable minima to give

$$\frac{\partial^2 w}{\partial \theta^2} = M_s H_x \cos\theta + M_x H_y \sin\theta + 2K_u (\cos^2\theta - \sin^2\theta) = 0 \tag{1.24}$$

if we eliminate θ from these two equations we get the Stoner-Wohlfarth astroid

$$H_x^{2/3} + H_y^{2/3} = \left(\frac{2K_u}{M_s} \right)^{2/3} \tag{1.25}$$

This astroid shows the critical values of the external field where the magnetization has a stable equilibrium value and is shown in Fig 1.1. The line δw/δθ=0 is always tangent to this curve. To find the equilibrium position for a given field (H_x,H_y) plot the point for these coordinates. Draw the line(s) which go through that point and are tangent with the astroid. For points outside the astroid there is one stable equilibrium position. For points inside the astroid there are two unstable equilibria. Which one the sample holds at a given time depends upon history. The direction of the tangent line gives the magnetization direction. This astroid is often used to explain the hysteresis curve in a ferromagnet.[28] This astroid does explain magnetic switching, but only quasi-statically. The equilibrium condition can be found for a given field, but it contains no information about how it gets from one equilibrium to another when fields change.

Several experiments found that when inverse switching time (1/τ) is plotted against magnetic field [30] there is a line with two slopes (see Fig 1.2). For smaller applied fields, the linear region is interpreted as being a reversal due to domain wall motion. At higher fields when the curve becomes steeper it is interpreted as being due to a faster coherent rotation. In the region between domain wall motion and coherent rotation, a regime of

Fig 1.2 Inverse switching time 1/T as a function of longiudinal magnetic field H_L with the transverse magnetic field H_T as a parameter (from Olson and Pohm)[29]

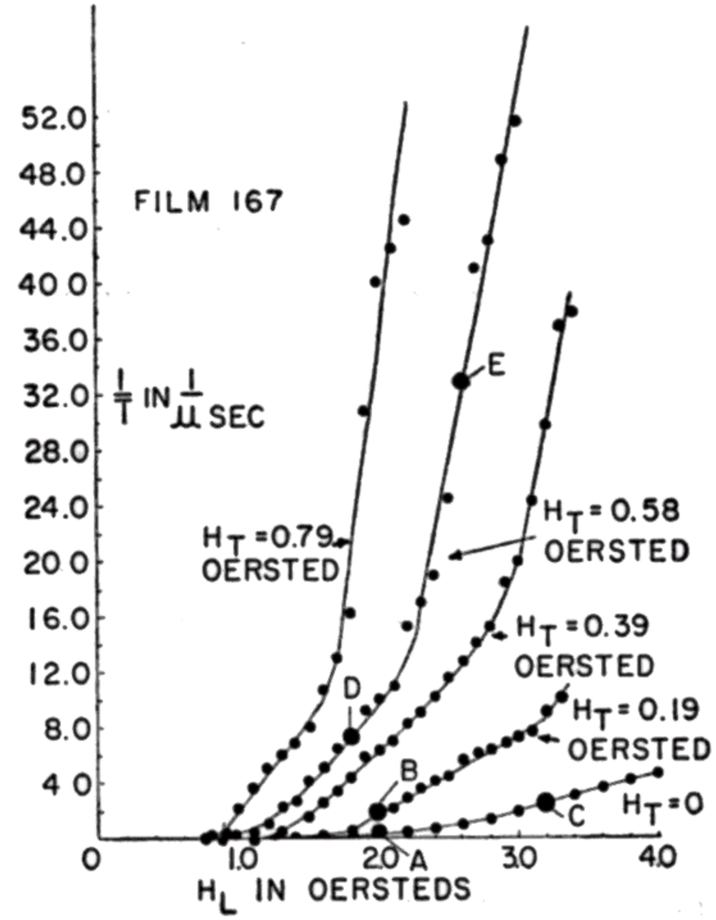

incoherent rotation was proposed by Gyorgy.[31] He produces a model where he assumes that decoherence of spins cause demagnetizing and exchange energy to be everywhere the same and thus not necessary to include in the calculation. Only the applied field needs to be taken into account in this case. He derives the following equation for the switching time:

$$\frac{1}{\tau_S} = \frac{1}{2\alpha\left[1+\frac{1}{\alpha^2}\right]\left(\frac{1}{\gamma}\right)A} H \tag{1.26}$$

where τ_S is the switching time and A is a constant related to the initial magnetization angle. Note that inverse switching time and field are still linear in this regime, although the constant of proportionality has changed. Also note that no spatially resolved experiments existed at this time (the 1950's) to verify that motion was indeed an incoherent reversal.

The next fundamental concern to address is the risetime of the switching pulse itself. This governs when switching goes from quasi-static reversal to dynamic reversal. The major difference is that in dynamic switching there are nonequilibrium magnetization states which are not available quasistatically. Experimental access to these states is allowed using time resolved scanning Kerr effect microscopy (TR-SKEM), as is shown in this thesis. Unlike previous methods, it watches the magnetization change in response to a high bandwidth magnetic field instead of sitting at a critical field and viewing final equilibrium states, or waiting for thermal switching. The magnetization does not respond the same as it would in equilibrium, because it is not in equilibrium. This puts dynamic switching outside the realm of phenomena that can be addressed by looking at a static hysteresis loop. After a high bandwidth change in magnetization, the magnetization takes on many values as it gyrotropically oscillates to equilibrium. Different bandwidth steps will lead to different final states.

1.6 Spin Wave Dynamics

At the same time as the quasi-static switching work was going on considerable advances were made in the study of spin waves. Much of this progress was spurred on by industrial developments with radar and microwaves. This work will have to be unified with the quasi-static work to truly understand magnetization dynamics. This discussion is largely summarized in Stancil.[32]

Analytic spin wave calculations can be done by linearizing the Landau-Lifshitz-Gilbert equation. This immediately confines spin waves to small angle magnetic motion. In much of the work in this thesis, that assumption is untrue, thus making this theory a starting point, but with acknowledged limitations in applicability.

The first step in discussing analytic spin wave dynamics is to linearize the LLG equation (without damping)

$$\frac{d\mathbf{M}}{dt} = -\gamma(\mathbf{M} \times \mathbf{H}) \qquad (1.27)$$

We assume that the time varying parts of the field are small and can be written as

$$\mathbf{M} = \mathbf{M_o} + \mathbf{m} \qquad \mathbf{H} = \mathbf{H_o} + \mathbf{h} \qquad (1.28)$$

where $\mathbf{M_o}$ and $\mathbf{H_o}$ are large, static components of the magnetization and fields, and **m** and **h** are small time varying portions. Thus the torque equation becomes

$$\frac{d(\mathbf{M_o} + \mathbf{m})}{dt} = -\gamma\left[(\mathbf{M_o} + \mathbf{m}) \times (\mathbf{H_o} + \mathbf{h})\right] \qquad (1.29)$$

$\mathbf{M_o}$ and $\mathbf{H_o}$ are parallel so they produce no torque. Neglecting small terms this becomes

$$\frac{d\mathbf{m}}{dt} = -\gamma\left[(\mathbf{M_o} \times \mathbf{h}) + (\mathbf{m} \times \mathbf{H_o})\right] \qquad (1.30)$$

If we assume that the solutions are oscillatory with time dependence $e^{-i\omega t}$ and we set $\mathbf{M_o}$ and $\mathbf{H_o}$ to be along the symmetry (z) axis, then the torque equation becomes

$$-i\omega\mathbf{m} = -\gamma\hat{\mathbf{z}} \times \left\lfloor M_s\mathbf{h} - H_o\mathbf{m} \right\rfloor \qquad (1.31)$$

If we solve for the various components of **h** we get

$$h_x = \frac{\gamma H_o m_x + i\omega m_y}{\gamma M_s} \qquad h_y = \frac{\gamma H_o m_y - i\omega m_x}{\gamma M_s} \qquad h_z = 0 \qquad (1.32)$$

We can write this as a matrix equation

$$\begin{bmatrix} h_x \\ h_y \end{bmatrix} = \frac{1}{\gamma M_s} \begin{bmatrix} \gamma H_o & i\omega \\ -i\omega & \gamma H_o \end{bmatrix} \begin{bmatrix} m_x \\ m_y \end{bmatrix} \tag{1.33}$$

and then invert this to obtain a susceptibility tensor

$$\mathbf{m} = \overset{=}{\chi} \bullet \mathbf{h} \tag{1.34}$$

where $\overset{=}{\chi}$ is called the Polder susceptibility tensor,

$$\overset{=}{\chi} = \begin{bmatrix} \chi & -i\kappa \\ i\kappa & \chi \end{bmatrix} \tag{1.35}$$

where

$$\chi = \frac{\gamma^2 M_s H_o}{\gamma^2 H_o{}^2 - \omega^2} \qquad \kappa = \frac{\gamma \omega M_s}{\gamma^2 H_o{}^2 - \omega^2} \tag{1.36}$$

To go further we will need to include equations for magnetostatics. We start with Maxwell's equations which deal with magnetism

$$\nabla \bullet \mathbf{B} = 0 \qquad \nabla \times \mathbf{H} - \frac{1}{c}\frac{\partial \mathbf{D}}{\partial t} = \frac{4\pi}{c}\mathbf{J} \tag{1.37}$$

and in the static case take the time derivative and the current **J** to be zero. So these equations become

$$\nabla \bullet \mathbf{B} = 0 \qquad \nabla \times \mathbf{H} = 0 \tag{1.38}$$

For these equations to hold in general, they must hold for the small time varying portions b and h. Therefore

$$\nabla \bullet \mathbf{b} = 0 \qquad \nabla \times \mathbf{h} = 0 \tag{1.39}$$

where b is

$$\mathbf{b} = \mathbf{h} + 4\pi\mathbf{m} = \mathbf{h} + 4\pi\overset{=}{\chi}\mathbf{h} = \overset{=}{\mu} \bullet \mathbf{h} \tag{1.40}$$

and μ is defined as

$$\overset{=}{\mu} = \begin{bmatrix} 1+4\pi\chi & -4\pi i\kappa & 0 \\ 4\pi i\kappa & 1+4\pi\chi & 0 \\ 0 & 0 & 1 \end{bmatrix} \tag{1.41}$$

We can define a scalar potential ψ such that h=-∇ψ since that will automatically satisfy the Gauss's Law equation. Then we have

$$\nabla \bullet \mathbf{b} = \nabla \bullet \left(\overline{\overline{\mu}} \bullet \nabla \psi \right) = 0 \tag{1.42}$$

which gives

$$\begin{pmatrix} \frac{\partial}{\partial x} & \frac{\partial}{\partial y} & \frac{\partial}{\partial z} \end{pmatrix} \bullet \left[\begin{pmatrix} 1+4\pi\chi & -4\pi i\kappa & 0 \\ 4\pi i\kappa & 1+4\pi\chi & 0 \\ 0 & 0 & 1 \end{pmatrix} \bullet \begin{pmatrix} \frac{\partial}{\partial x} \\ \frac{\partial}{\partial y} \\ \frac{\partial}{\partial z} \end{pmatrix} \psi \right] = 0 \tag{1.43}$$

Which reduces to

$$(1+4\pi\chi)\left[\frac{\partial^2 \psi}{\partial x^2} + \frac{\partial^2 \psi}{\partial y^2} \right] + \frac{\partial^2 \psi}{\partial z^2} = 0 \tag{1.44}$$

This is Walker's equation for magnetostatic modes in a homogenous medium in cgs units. In SI units the equation is

$$(1+\chi)\left[\frac{\partial^2 \psi}{\partial x^2} + \frac{\partial^2 \psi}{\partial y^2} \right] + \frac{\partial^2 \psi}{\partial z^2} = 0 \tag{1.45}$$

In general, this equation is tough to solve except in simple geometries. Walker [33] solved it in a spheroid. Damon and Eshbach [34] solved it in a thin layer. In more complicated geometries numerical work is usually needed. This is the classical derivation of spin waves starting from Maxwell's equations. Although this derivation is explicitly done for small angle waves, the classical derivation probably best approximates what is seen in experiment.

Spin waves can also be obtained starting from a quantum mechanical problem. In these problems, spin waves are quasi-particles of flipped magnetization (roughly analogous with phonons) called magnons.

This calculation is mathematically involved (for complete details see White [35]). One can start with the Holstein-Primakoff Hamiltonian [36] which is a second quantized Hamiltonian that includes Zeeman, exchange and dipole-dipole demagnetizing energy. One can develop raising and lowering (creation and anhihilation) spin operators to diagonalize this Hamiltonian. The frequency dispersion for wavevector k=0 is found to be:

$$\omega = \sqrt{\left(\gamma H_i + N_x \omega_M\right)\left(\gamma H_i + N_y \omega_M\right)} \quad (1.46)$$

where $H_i=H_o-4\pi N_z M_s$, $\omega_M=4\pi\gamma M_s$, H_o is the external field, $N_{x,y,z}$ are demagnetizing factors that depend upon sample geometry and are defined as

$$\mathbf{H_d} = \frac{-\overline{\overline{N}} \bullet \mathbf{M}}{4\pi}, \quad (1.47)$$

where in a diagonalized geometry $N_x+N_y+N_z=1$. Thus, one can by symmetry arguments "guess" the demagnetizing factors (for example in a sphere, by symmetry, $N_x=N_y=N_z=1/3$).

We can look at this formula in the special case where we have an infinite planar thin film with the external field directed along one of the axes in the plane. Thus we have the x and z (magnetic field direction) in plane and the y axis out of plane. Since the film is infinite in both x and z, it will have zero demagnetizing factor in those directions. Hence we get $N_x=N_z=0$ and $N_y=1$, and the frequency dispersion is

$$\omega = \gamma\sqrt{H_o(H_o + 4\pi M_s)} \quad (1.48)$$

This is the Kittel formula [37] which gives the ferromagnetic resonance frequency as a function of applied field in a thin film sample.

In the case where $\mathbf{k}\neq 0$ the frequency dispersion is far more complex.

$$\omega_k = \sqrt{\left[\gamma H_i + 2zJS\left(1-\gamma_k\right)\right]\cdot\left[\gamma H_i - 2zJS\left(1-\gamma_k\right)\right] + \omega_M \sin^2\theta_k} \quad (1.49)$$

where z is the number of interacting nearest neighbor sites, J is the exchange constant between neighboring spins, S is the spin quantum number, θ_k is a spherical coordinate and $\gamma_k = \frac{1}{z}\sum_{\delta} e^{i\mathbf{k}\bullet\boldsymbol{\delta}}$ where δ is the vector between exchange coupled nearest neighbors.

In the one dimensional case, we assume that there are two nearest neighbors (z=2) then

$$1-\gamma_k = 1-\cos ka \quad (1.50)$$

where a is the lattice constant. For small k we have

$$1-\cos ka \approx 1-\left(1-\frac{k^2a^2}{2}\right) = \frac{k^2a^2}{2} \quad (1.51)$$

thus

$$\omega_k = \sqrt{\left(\gamma H_i + JSk^2a^2\right)\left(\gamma H_i + JSk^2a^2 + 4\pi M_s\gamma \sin^2\theta_k\right)} \quad (1.52)$$

Note that this dependence is nearly quadratic and has a non-zero offset near k=0. Looking at the angular dependence, the frequency will be highest perpendicular to the symmetry axis (θ_k=90°) and lowest for propagation along that direction (θ_k=0°)

1.7 Spin Wave Example – Damon-Eschbach Modes

Damon and Eschbach calculated the magnetostatic modes for a thin layer magnetized in plane.[34] Since this approximates our experimental case, it is instructive to look at.

We need to solve the Walker equation inside the material. To start we can assume a trial wave function Ψ inside the material

$$\psi_{in}(\mathbf{r}) = \psi_o \cos(k_z z)e^{i\mathbf{k_t}\bullet\mathbf{r}} \quad (1.53)$$

where $\mathbf{k_t}$ is a wave vector in the plane. Outside the material we must satisfy the Laplace equation

$$\nabla^2\psi = 0 \quad (1.54)$$

Here we will have a trial solution like

$$\psi \sim e^{i\mathbf{k}_{\mathbf{t,out}}\bullet\mathbf{r} \pm k_{t,out} z} \quad (1.55)$$

Since we want Ψ to vanish at infinity, we have to choose the signs of the exponent correctly. Above the film we have

$$\psi_{above}(\mathbf{r}) = Ce^{i\mathbf{k}_{\mathbf{r,out}}\bullet\mathbf{r} - k_{r,out}z} \quad (1.56)$$

and below the film we have

$$\psi_{below}(\mathbf{r}) = De^{i\mathbf{k}_{\mathbf{r,out}}\bullet\mathbf{r} + k_{r,out}z} \quad (1.57)$$

The boundary conditions on the fields require that the tangential **h** be continuous, assuming the absence of any sheet currents, and that the normal **b** be continuous. The condition on **h** is equivalent to requiring continuity of Ψ across the boundary. This requires that C=D and that $\mathbf{k}_{t,out}=\mathbf{k}_t$ and

$$Ce^{-\frac{k_t d}{2}} = \psi_o \cos\left(\frac{k_z d}{2}\right) \tag{1.58}$$

where d is the thickness of the film and the z-axis origin is at the center of the thickness. Continuity of the normal component of **b** at z=±d/2 gives

$$Ce^{-\frac{k_t d}{2}} = \psi_o \sin\left(\frac{k_z d}{2}\right) \tag{1.59}$$

Thus we have

$$\tan\left(\frac{k_z d}{2}\right) = \frac{k_t}{k_z} \tag{1.60}$$

Substituting our trial function into the Walker equation we get

$$(1+\chi)\left(k_x^2 + k_y^2\right) + k_z^2 = 0 \tag{1.61}$$

Thus if we have $k_t^2=k_x^2+k_y^2$ then we can relate k_t and k_z by

$$\frac{k_t}{k_z} = \frac{1}{\sqrt{-(1+\chi)}} \tag{1.62}$$

When this gives a real solution (i.e., $1+\chi<0$) we have allowed modes within the spin manifold. If we combine these results and eliminate k_z then we will get a dispersion relation giving k_t as a function of frequency ω (which is buried within χ)

$$\tan\left[\frac{k_t d}{2}\sqrt{-(1+\chi)}\right] = \frac{1}{\sqrt{-(1+\chi)}} \tag{1.63}$$

This equation can be solved graphically. It gives multiple solutions which are numbered n=0,2,4 etc. We can repeat the same process for a sine-wave trial solution and get odd solutions in n=1,3,5 etc. where n corresponds to the number of nodes through the film thickness. These two can be combined into one full solution

$$\tan\left[\frac{k_t d}{2}\sqrt{-(1+\chi)}-\frac{n\pi}{2}\right]=\frac{1}{\sqrt{-(1+\chi)}} \qquad (1.64)$$

The first few of these modes are shown in Fig 1.3 with constants chosen to represent permalloy. H_o is taken to be 500 Oe and the sample thickness is taken to be 15 nm in this example. Note that the spin wave manifold (range of real solutions) runs from γH_o, the magnetic resonance frequency of a free spin, up to $\gamma\sqrt{M_s H_o + H_o^2}$. For this example that gives values of 88 to 145 1/s.

This calculation is merely a starting point for a comparison with any of our experiments. It is important to keep in mind the assumption of low amplitude spin waves. Also, the thin layer is assumed to be infinite in dimension. Storey et al [38] have taken the Damon-Eschbach modes one step further by "quantizing" them. They allow only wavelengths that fit evenly within the finite length and width of the material to occur. This method is an improvement, but it still does not take into account edge effects, demagnetizing fields and non-uniformity within the slab. However, their calculation does agree well with their experimental results. Bryant et al [39] take into account edge effects and demagnetization using a variational method. They also discuss the merits of this approximate approach. Another drawback is the assumption that there are no sheet currents in the layer. In conductors such as permalloy we can have eddy currents. However, this has not prevented permalloy from being used for experimental comparisons in the past, although the impetus to study permalloy stems from its industrial relavance.

Fig 1.3 Dispersion relation for first five Damon-Eschbach modes in permalloy. Lowest mode is n=0. Next lowest is n=1 etc up to n=5.

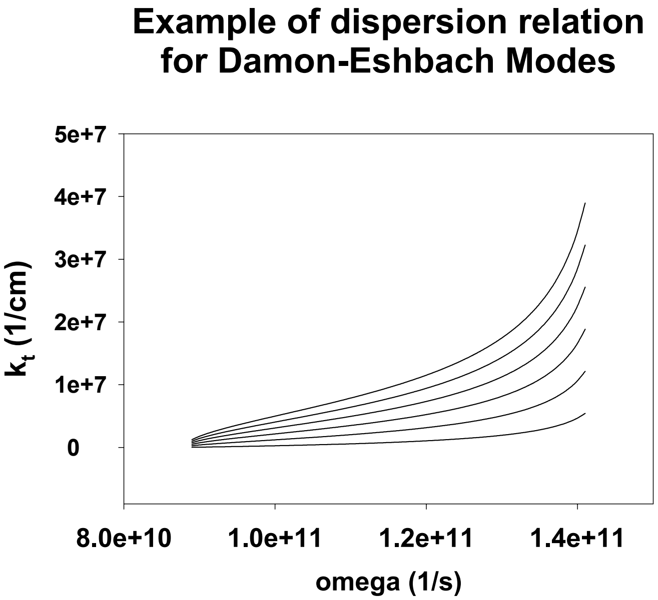

Using micromagnetic simulation one can generate spin waves (although non-analytically) for comparison with experiment. In some ways, this is done in this thesis, although only with moderate success because the spin waves generated in experiment are often not fully resolved spatially. These results are shown in chapter five. This is one way in which the form of damping in the simulation can be checked definitively. The damping form that gives the appropriate spin waves will likely be the correct form.

1.8 Modern Works in Magnetism

A good summary of some pertinent modern works in magnetism is found in Hiebert.[21]

A large amount of work has been done imaging static magnetic domains in thin film permalloy. Hubert and Schaffer [40] contains several images and discussions about this topic. A large variety of domain structures are possible. For example, domain wall structure varies with film thickness. For thin samples (~10 nm) domain walls are largely symmetric Neel walls (where magnetization rotates in the plane of the sample). For thicker samples (90 nm or greater) domain walls are usually Bloch walls (where magnetization rotates in the plane of the wall). In intermediate regimes, walls are an intermediate cross-tie wall (where magnetization rotates in both senses), with increasing cross-tie density as thickness increases. Labyrinth patterns can also occur. This is likely due to demagnetizing field coupling across grain boundaries in a polycrystal sample. This is known as a magnetization ripple.[41] Stray field coupling will be locally stronger in either the lateral or transverse direction and will thus lead to symmetry breaking in experimental results.

Static imaging is not necessarily limited to surfaces. Techniques exist to probe buried layers in magnetic multilayers. Buhrman et al [42] use Ballistic Electron Magnetic Microscopy (BEMM) where they use a sharp tip scanned across a sample to inject "hot" electrons. The top magnetic layer will act as a polarizer, as only those electrons with the same spin direction as those in the top magnetic layer will travel through the layer. When current is measured in lower layers, those layers will act as an analyzer, since the polarized electrons from the top layer will be scattered unless the lower layer has the same magnetization direction. Pollmann et al [43] use a polarized x-ray microprobe to image buried layers. This uses intermediate energy x-rays (5-10 keV) which allow for penetration of the top layers of the structure to obtain information from buried layers. This method has the further benefit that it allows for element specific information, as x-rays can be tuned to the chemical composition of the layers. Techniques such as magnetic resonance force microscopy [44] also show promise to allow imaging of buried layers.

In some experimental works on dynamic magnetization switching, thermal switching is studied. A sample is held near its coercive field, such that thermal switching becomes probable. Lederman et al [45] show thermal activation work on single domain γ-Fe_2O_3 particles. They find the thermal energy barrier to be more complex than just a single Neel barrier. Below a 30° switching field a curling mode is seen. Above a 30° switching field, uniform rotation is observed. Koch et al [46] , after experiment and modeling, discuss an energy ladder containing several Neel barriers to be crossed, each with a probability of crossing forwards or backwards. Switching occurs when all of the energy barriers have been surmounted.

Gyrotropic switching has been studied by Bach et al [47] using the Stanford Linear Accelerator Center (SLAC) test beam, which is capable of producing local fields up to several Tesla with 2-4.4 ps length in time, by driving an electron bunch through a thin film sample. In these excitations, there is not sufficient time available for thermal activation to play any significant role, so thermal effects are removed from gyrotropic switching. Co/Pt multilayers were analyzed post-excitation in their final equilibrium state, and the domains observed are consistent with coherent rotation in the different fields.

Using magnetic modeling, the gyrotropic nature of reversal has been studied further. For example Hillebrands et al [48] have used Stoner-like magnetic particles to model their response to field pulses of varying strength, direction, length and shape. Longer pulse data is governed by magnetic damping, and shorter pulses are dominated by gyrotropic effects. The differences can be huge as is shown in Fig 1.4 [48] which shows switching astroids with different pulses. Fig 1.4a corresponds to a square field pulse of 2.75 ns duration, while in figure 1.4b it is 250 ps long. In the long pulse limit (a pulse lasting long enough that the system reaches a new equilibrium and with a long enough risetime to remove the precessional effects), we expect that the result is the Stoner-Wohlfarth astroid. Although the longer pulse more closely resembles it than the shorter one, both show oscillatory behavior. The sample initially has its magnetization pointed in the left direction. A pulse is applied that has components H_x and H_y as shown by the axes on the plot. If the sample remains unswitched after the pulse the region is shown in dark grey. If it switches, the region is shown in lighter grey. In general, if a pulse is applied to the left, no switching occurs. If a pulse is applied to the right, which is strong enough to overcome coercivity, switching occurs. If the pulse is short enough, it can start gyromagnetic oscillations, which may or may not induce switching. Switching is dependant upon which of the two magnetization directions the spin is pointing along when the oscillations damp out. Hence, it is possible to induce switching with a field pointing to the left (such as point a) depending upon the length of the pulse and a field exceeding coercivity, but pointing to the right will not necessarily induce switching.

Figure 1.4 Switching astroids for square-pulse magnetic field inputs. If a pixel is displayed in light grey the sample switched. If it is dark grey it did not. (a) Longer pulse of 2.75 ns causes only slight deviation from regular Stoner-Wohlfarth switching (b) Short field pulse of 0.25 ns causes much larger deviations (from Bauer et al [48])

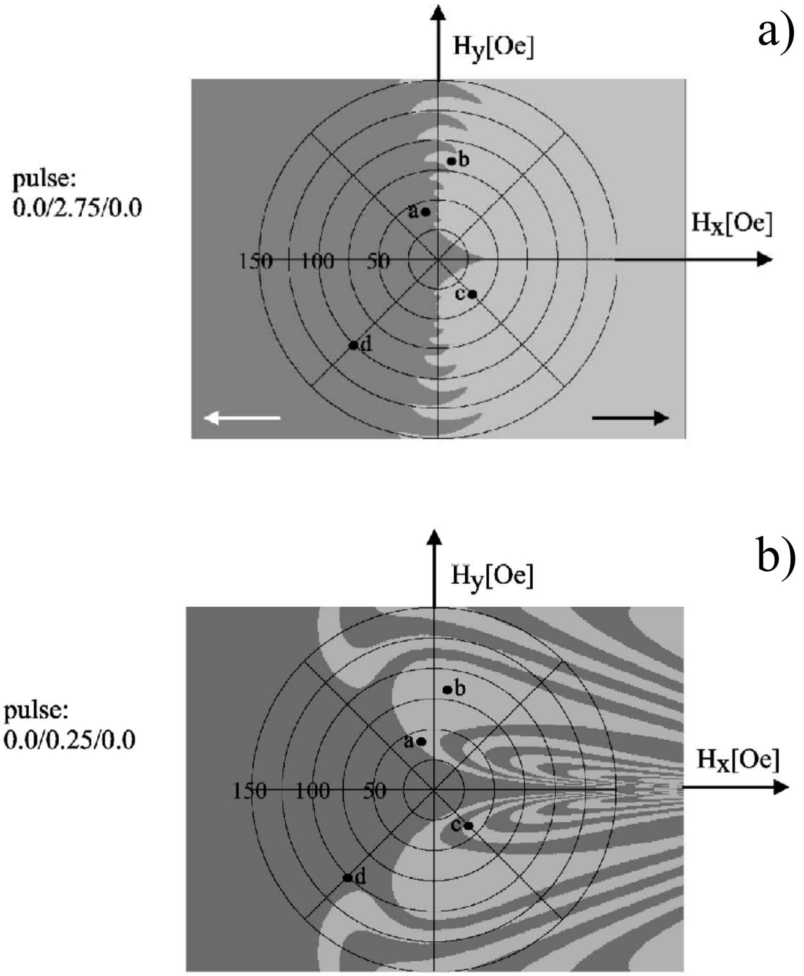

The theory of the magnetic damping constant is discussed by Suhl [49] . He discusses different damping mechanisms: relaxation to the lattice, and "indirect" relaxation via excitation of spin wave modes. He concludes that two distinct damping RATES might be seen during a switching process. The first portion will be a rapid damping governed by spin wave excitations, and the second portion slower and governed by damping to the lattice. Silva et al [50] have taken this one step further by explaining experimental work, assuming (in an ad-hoc manner) two different damping CONSTANTS for the different portions of the dynamical motions. This is probably not justified since many simulations show apparent two rate damping for just one damping constant (as in chapter 5 of this thesis).

Safonov and Bertram [51] look at magnetization reversal as a nonlinear multimode process. They simulate magnetization reversal in a single grain sample, where the grain is treated as a small system of subgrains that are exchange coupled and have uniaxial anisotropy. Their gyromagnetic equations were solved without damping. The magnetization follows Suhl's discussion and shows a non-linear spin wave excitation on short timescale. The spatially averaged magnetization over the grain significantly decreases during the reversal. Bertram et al [52] go further in applying similar calculations to a thin film. They find that excess Zeeman energy is transferred to magnetostatic and exchange coupled spin waves allowing the average magnetization to "relax" even in the absence of damping.

Experimentally, several groups are studying dynamic magnetization processes. Results from our group [53] are discussed in many places in this thesis. Silva and Rogers [50] have done work using a permalloy bar on a microstrip line. The bar is placed on top of a center conductor strip with step and impulse excitations sent down it along the hard axis (transverse direction). An inductive sampling technique is initially used. Rotation times as short as 200 ps are reported. It is in some of the step data that they observe anomalous transient damping and introduce two separate values of the damping constant α. This work is done without spatial resolution.

Using the second harmonic magneto-optic Kerr effect (SHMOKE), Silva et al [50] have added spatial resolution. The frequencies of underdamped precessional response from the inductive measurement and the SHMOKE measurement are slightly different. This is attributed to slightly different responses from the sample's bulk and surface properties, as second harmonic probes are principally sensitive to surfaces due to the symmetry breaking there.

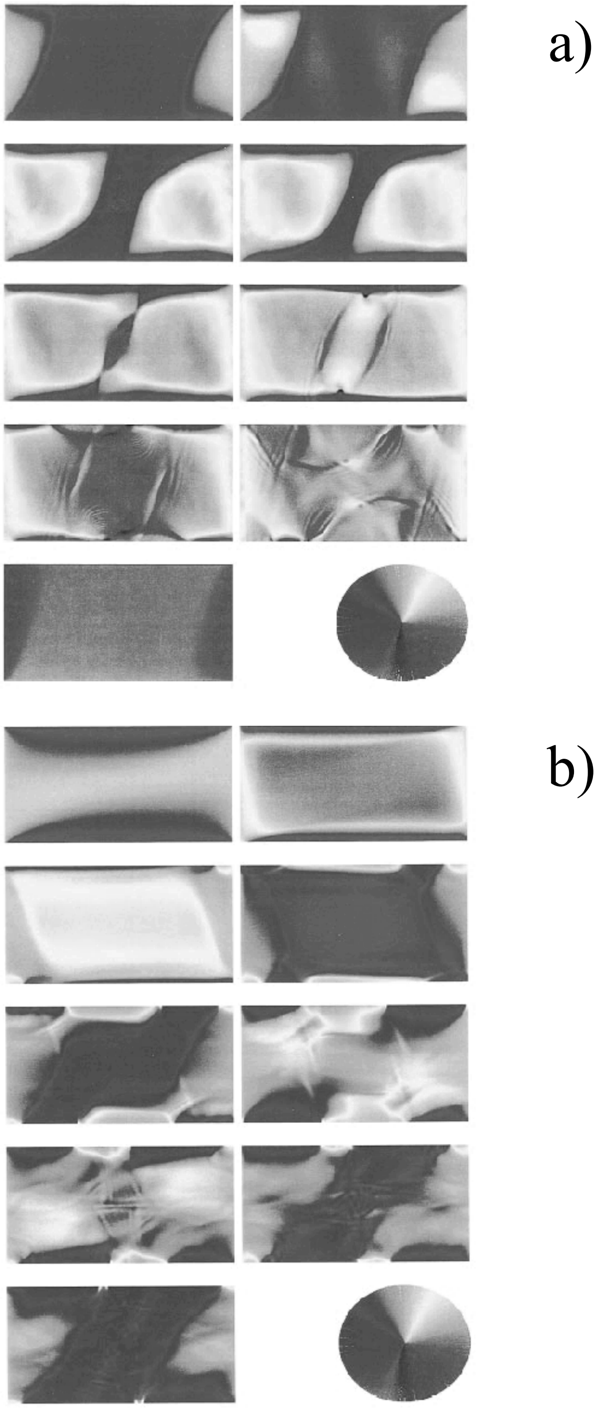

Figure 1.5 Simulated reversal in a 5 nm thick 1.6 x 0.8 μm $Ni_{60}Fe_{40}$ element. **(a)** Reversal with a 70 Oe easy axis field. The times of the images are 0, 0.25, 1.42, 1.59, 1.75, 1.90, 2.07, 2.32 and 6.61 ns after the application of the pulse, reading left to right.. **(b)** Reversal with a hard axis field of 50 Oe and an easy axis field of 80 Oe. The times of the images are 0, 159,279,399,519,639,849,969 and 1089 ps after the application of the pulse, reading left to right.

Koch et al [54] measure and simulate dynamical magnetization reversal in a 5 nm thick, 1.6 x 0.8 μm thin film $Ni_{60}Fe_{40}$ sample. The magnetization is measured by using the element as the top layer of a spin polarized tunnel junction and measuring the tunnelling resistance across it. The switching time is measured as a function of pulse amplitude with times ranging from 10 ns down to 500 ps and the pulse amplitude increasing from the coercivity (14 Oe) to 100 Oe. This method does not allow for any spatial resolution. These results were compared to the simulation which is shown in Fig 1.5. This simulation is quite reminiscent of many that will be shown further into this thesis. Here there is a 70 Oe easy axis field pulse 10 ns in length (with a 40 ps rise time). In Fig 1.5 (a), the hard axis field (across the short dimension in plan) is zero. The edge domains grow and meet in the center of the film. The center then quickly rotates to align with the applied field and then nucleates reversal on the top and bottom edges of the film. In part b of the figure, a 50 Oe hard axis field is added. The reversal becomes more coherent. The magnetization vector rotates around the 80 Oe, 200 ps pulse. They found that most of there experimental observations could be accounted for with this simulation.

1.9 Summary of this Chapter

This first chapter is intended to give the reader a theoretical background to be able to understand the main ideas in micromagnetism and to give a broader context for this work. Motivation for this thesis research from both a fundamental and applied is presented. Ferromagnetism and magnetization dynamics are explored, introducing the Landau-Lifshitz-Gilbert equation. A history of work in magnetization statics and dynamics is presented along with an introduction to a complimentary body of work studying **k**-space spin wave dynamics. Finally, a survey of contemporary research in magnetism is provided.

2. Time-Resolved Scanning Kerr Effect Microscopy

This chapter discusses the experimental technique of time-resolved scanning Kerr effect microscopy (TR-SKEM). It is a combination of ultrafast laser techniques and optical microscopy to allow the observation of repetitive magnetization dynamics. This technique has been detailed in several places.[21,53] Those are more definitive references, while this chapter is intended as a general overview and a discussion of issues specific to the present experiments which are not fully covered in other reference material. The following describes background to the technique and the specific set-ups used to gather the data in this thesis.

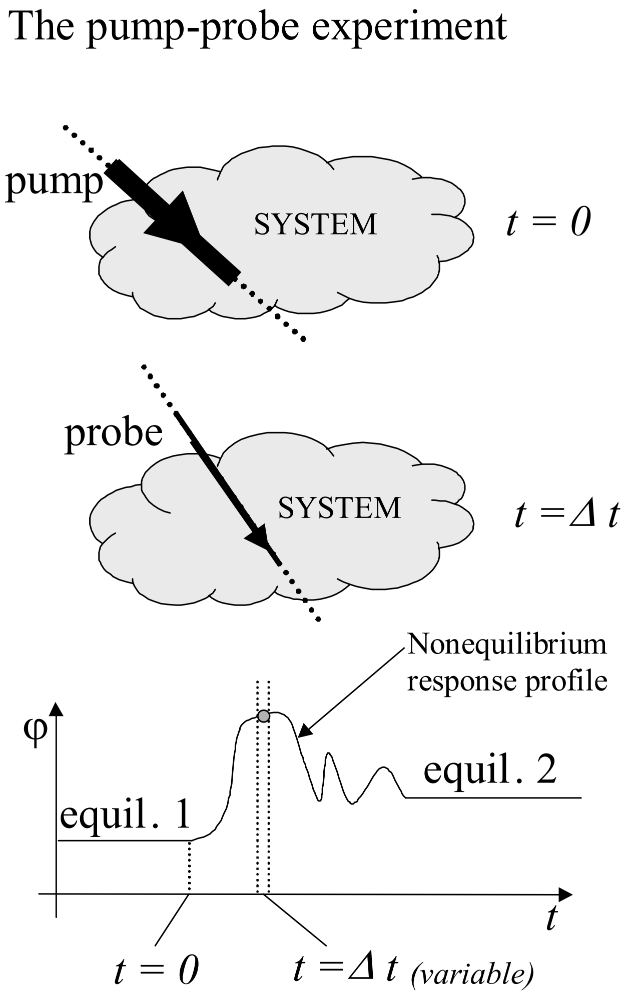

Figure 2.1 Cartoon showing a generic pump-probe experiment. A system is pumped out of equilibrium at time t=0. At a variable time (t=Δt) later the system is probed to acquire the nonequilibrium response of a parameter φ

2.1 Ultrafast laser techniques

Ultrafast lasers produce trains of very short optical pulses and are well suited to the study of transient phenomena. Two good reviews of ultrafast lasers and their applications are Diels and Kaiser.[55] Since the TR-SKEM system is an ultrafast microscopy system, general pump-probe ultrafast laser exeriments will first be described.

In pump-probe experiments, ultrafast lasers are used to stroboscopically observe repetitive phenomena. A cartoon of such an experiment is shown in Fig 2.1. A laser pulse is used to somehow excite, or pump, a sample at time t=0. At some later instant in

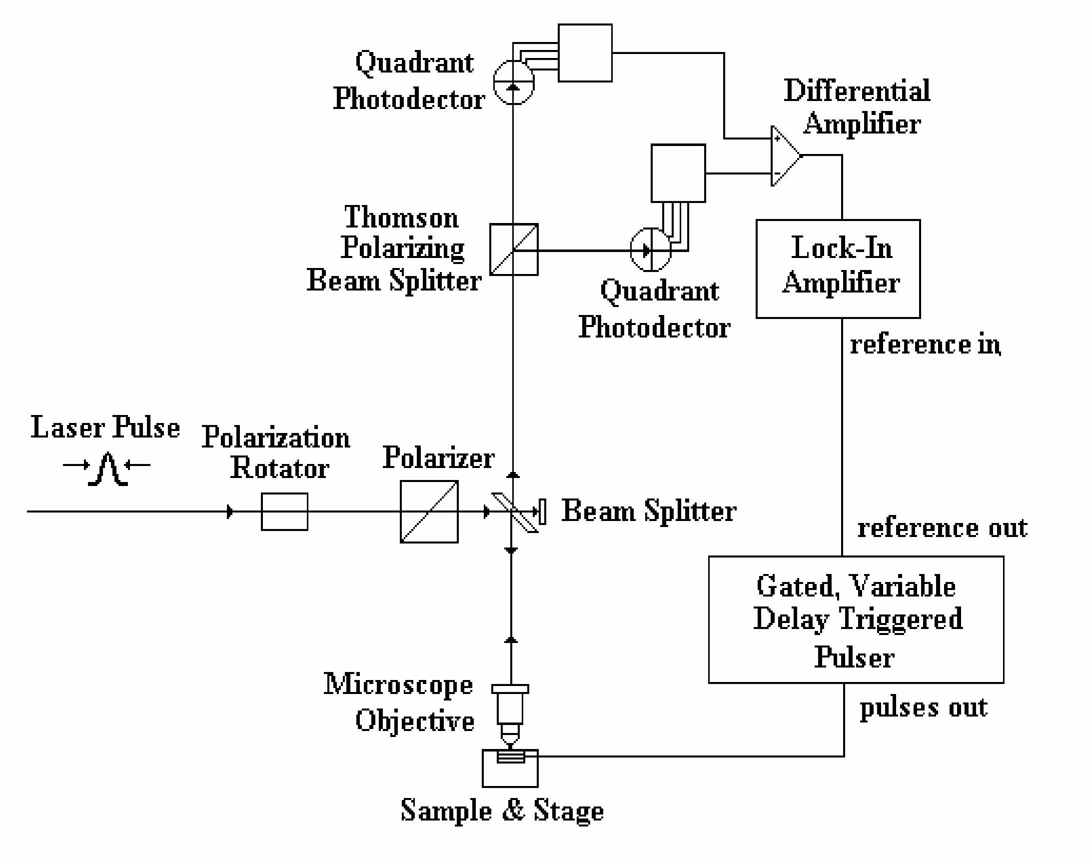

Figure 2.2 Schematic of Time-Resolved Scanning Kerr Effect Microscopy system used for magnetization reversal experiments. Sample is pumped with a pulser that is triggered by the pulse picker or cavity dumper of the laser. It is probed later with the laser beam itself. The rotation in the polarization plane of the reflected light gives access to the magnetization.

time Δt, the laser is used to probe the state of the sample giving a value of a parameter ϕ which is excited from equilibrium by the pump. The interval Δt can be varied by repeating this procedure to measure the entire non-equilibrium profile of the parameter ϕ. In principle, these techniques can have temporal resolution limited only by the width of the ultrafast laser pulse.

The heart of any ultrafast microscopy system is the laser itself. In the experiments in this thesis, the pulsed light source used is either a cavity-dumped dye laser or a Ti:Sapph laser that is run with or without a pulse picker.

The dye laser is pumped by a mode-locked frequency doubled Nd:YAG laser and cavity dumped at a rate between 0.5 and 4 MHz. Its pulse width is about 2 ps. The output of the dye laser is noisy and is the limiting factor in the signal in experiments using it. This is even after treatment with an electro-optic intensity stabilizer and filtering with either a pin hole spatial filter or a single mode polarization preserving optical fiber.

The Ti:Sapph system is far more stable. When pulse picked it has a repetition rate of 400 Hz to 4 MHz. It produces femtosecond pulses at around 800 nm (this value is tunable). When not pulse picked the pulses repeat at 80 MHz. The fundamental beam has RMS amplitude noise of well under one percent. This allows for the signal to noise to be limited by the detection instead of the laser.

2.2 Time-Resolved Scanning Kerr Effect System

The time resolved scanning Kerr effect microscopy system is the experimental system used in the work in this thesis. It uses an ultrafast laser to stroboscopically image dynamics using a homemade scanning optical microscopy system. Magnetic information is gathered using the Kerr effect, a rotation of the polarization plane of reflected light which is proportional to magnetization. A block diagram of a TR-SKEM system is shown in Fig 2.2.

To detect an image, we need to detect the change in the polarization direction of the light after reflection by the sample. A Thomson polarizing beam splitter is used to split the reflected beam into two perpendicular components. These components are calibrated to be equal when there is no magnetic signal (ie before time zero). The out of plane signal is the difference in intensity, measured by two silicon photodetectors placed after the Thomson beam splitter. The in-plane components are harder to detect, but can be

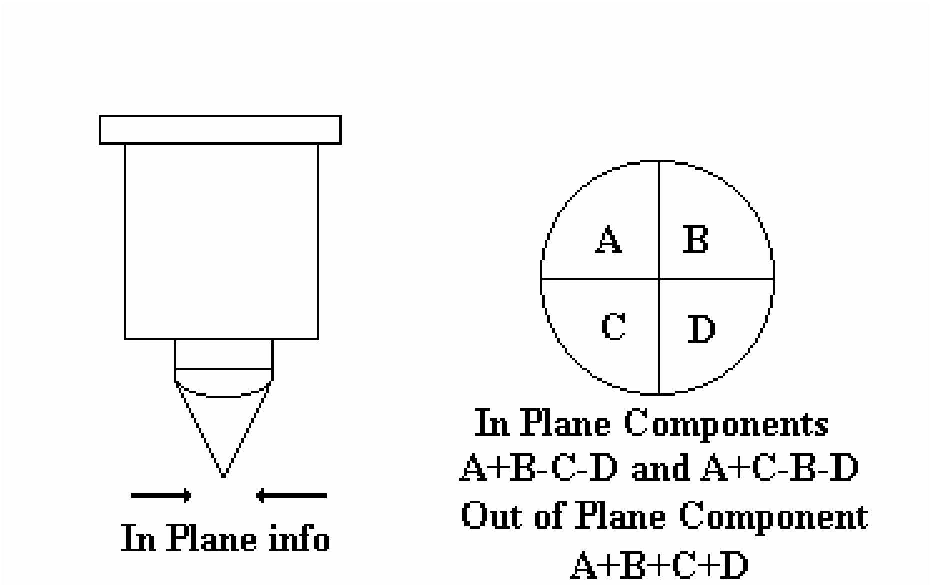

Figure 2.3 Quadrant detection system. A high numerical aperature objective will receive information from a cone of light foccused to a diffraction limited spot. Light scattered on either side of the cone will carry away information on the magnetization state in the plane of the sample. By adding and subtracting appropriate components in a quadrant detection system, one can isolate this in plane information from the out of plane information.

done using quadrant detection. There is an asymmetry in the reflected light scattered from the sample. This asymmetry can be magnified by using a high numerical aperature objective. Light reflected on the left side of the beam will carry away in plane information (as well as the out of plane information). Light reflected on the right side of the beam will carry away the same in plane information, but with opposite sign (as well as the same out of plane information). By adding the left side and subtracting the right side, gathered with quadrant photodetectors, we can separate the in-plane signal from the out of plane signal. The other in plane component can be gathered by adding the top and subtracting the bottom half of the signal. Fig 2.3 shows this is done. Calibration of the relative strength of the various components is still a problem. The out of plane component uses the polar Kerr effect while the in plane ones use the longitudinal Kerr effect. The difference is discussed more in section 2.3 where the Kerr effect is discussed in detail.

In the set-up shown in Fig. 2.2, which was used for magnetization reversal measurements, a gated, variable delay electronic pulser is used to excite the system. It is delayed electronically and excites a transient magnetic field which flows through a transmission line near the sample. The pulser is gated in the kHz regime. This allows the magnetic signal to be gathered using off the shelf kHz electronics using a lock-in

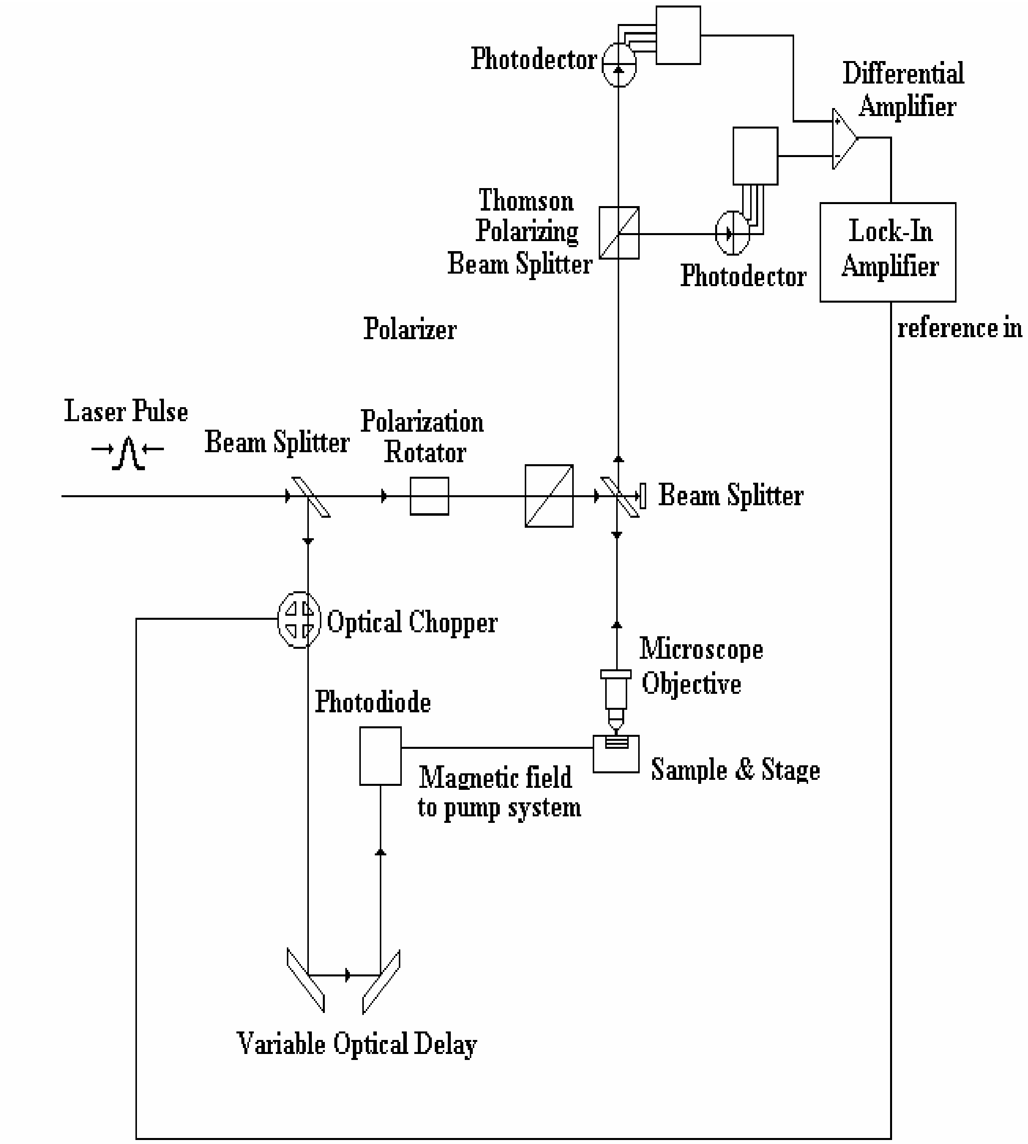

Figure 2.4 Experimental system used for ferromagnetic resonance experiments. The pump beam is shot through a variable delay line and then used to excite a fast magnetic field created by a photo-voltaic photodiode. At a point later the probe beam gathers magnetization information upon its change in polarization direction upon reflection from a magnetic sample.

amplifier. This system allows for detection over a delay range of tens of ns, with 50 ps temporal resolution.Ferromagnetic resonance experiments require better than 50 ps temporal resolution, so a different setup is used. Figure 2.4 shows this experimental set-up used for ferromagnetic resonance experiments. The main modification from the previous setup is in the sample pumping. The laser pulse is split into two beams. The probe beam is sent into an optical delay line, a retro-mirror that can be mechanically moved by a stepper motor to increase or decrease delay. The light is then shot back onto a photo-voltaic diode which provides the current for the transient magnetic field. The probe beam is also delayed by a constant amount so that it arrives after the pump beam.

Different experimental set-ups are used for different experiments due to the differing time scales over which the experiments must measure. In the magnetization reversal experiment, a sample is reversed with a 10 ns magnetic field pulse, reversal times are typically hundreds of picoseconds to a few nanoseconds. It is necessary to probe time differences longer than the transient magnetic field pulse, so a dynamic time range of more than 10 nanoseconds is needed. This can be accomplished using an electronic delay. The drawback of electronic delay is that jitter in the electronics limits temporal resolution to about 50 picoseconds at best, but this is acceptable because it is smaller than the reversal times. There is a trade off between the temporal resolution and the length of time that can be studied in an experiment. In a ferromagnetic resonance experiment better temporal resolution is needed. The period of oscillation may be a couple hundred picoseconds or less, and we wish to study what is happening within an oscillation period. The sample is pumped by as quick a transient field as possible. The pulse from the photodiode is nominally symmetric. It has a roughly 100 ps rise time and a 100 ps fall time (limited by the speed of the photodiode) – which contrasts to the 10 ns excitation in the reversal experiment. The sample will continue to oscillate for a few nanoseconds if the field conditions are correct. Using a mechanical delay line, the problem of electronic jitter is removed leaving the width of the laser pulse as the factor that limits temporal resolution of the observation. One picosecond delay corresponds to a moving the mirror 0.15 mm ($c=2d/t$) which can be easily done with off the shelf components. A delay line that allows for 90 cm of motion for the mirror (as is used for the ferromagnetic resonance experiment) will have a range of 6 ns. It is possible to make delay lines longer and longer to keep this better temporal resolution, but the arrangement quickly becomes unmanageable. The longer the line is, the more critical the alignment of the optics becomes. In the ferromagnetic resonance experiment, we can have a sub picosecond temporal resolution, but are limited to about a 6 nanosecond range in time.

The other major difference between the two configurations is the repetition rate. Both experiments can be run simultaneously using the pulse picked light for the reversal experiment and the non-pulse picked light for the resonance experiment. The non-pulse picked light will have an 80 MHz repetition rate leaving 12.5 nanoseconds between stroboscopic events. This is long enough for the sample to return to equilibrium in the resonance experiment, but not in the reversal experiment, which is typically run at 800 kHz.

In both systems, a transient electrical current pulse is generated which will create a magnetic field pulse to drive the sample out of equilibrium. To excite a sample out of plane, the sample should be situated beside the current carrying line. To excite a sample in plane, it should be situated on top of the current carrying line.

The imaging is stroboscopic. It must be triggered repetitively and synchronously with the laser pulses. To build up sufficient signal, the interaction of numerous laser pulses and repeated events are averaged and built up into a signal. Because of this, it is possible to extract picosecond temporal information using kHz bandwidth electronics and detectors.

2.3 Magneto-optic Kerr Effect

To make our measurements we use the magneto-optic Kerr effect (MOKE) to measure the magnetization state of a sample. Two good references on this topic are the Hubert and Mansuripur textbooks.[40, 56] The Kerr effect is the rotation of the polarization plane of light when it is scatterered (reflected) by a magnetic material. Mathematical analysis of the Kerr effect depends of the relative geometry of the incident light and the magnetization direction in the material. There are three basic geometries. For magnetization out of plane of the sample, the geometry is known as the polar Kerr effect. For in plane magnetization, parallel to the plane of incidence of the reflected light, it is

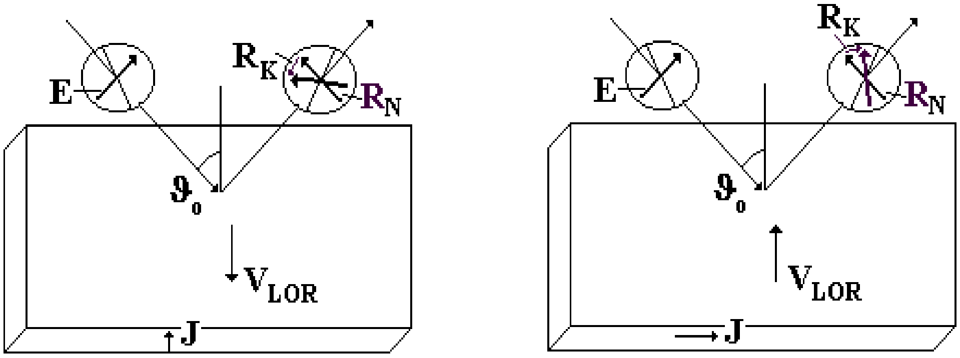

a) polar || **b) longitudinal ||**

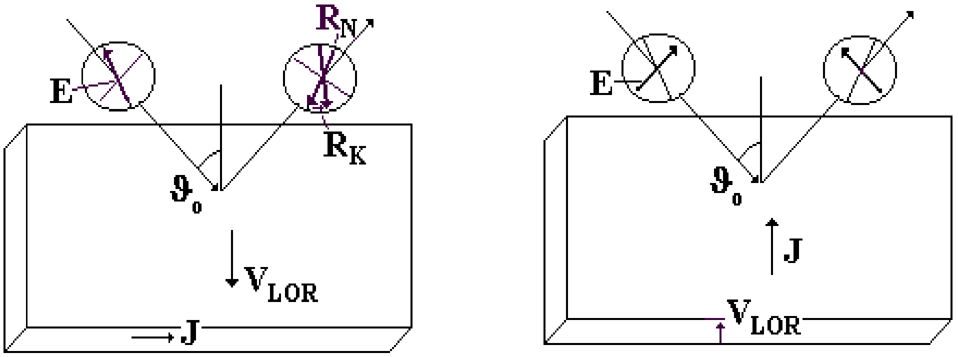

c) longitudinal ⊥ **d) transverse**

Figure 2.5 Geometries for the various Kerr effects. **E** is the incident light's direction of polarization, which has an angle of incidence ϑ_o. $\mathbf{R}_N$ is the regularly reflected electric field amplitude. $\mathbf{R}_K$ is the magneto-optical Kerr amplitude. This amplitude can be conceived as being generated by the Lorentz motion $\mathbf{V}_{LOR}$. which is due to current density **J**. **a)** shows the polar Kerr effect (in this case with **E** parallel to plane of incidence). The effect is the same for **E** perpendicular. **b)** shows longitudinal Kerr effect for **E** parallel to the plane of incidence. **c)** shows the longitudinal effect for **E** perpendicular to the plane of incidence. This is the same effect as in **b)** but opposite in sign d) shows the transverse Kerr effect. Only polarization perpendicular to the plane of incidence yields an effect

known as the longitudinal Kerr effect. For in plane magnetization, perpendicular to the plane of incidence, it is known as the transverse Kerr effect. These geometries are shown in figure 2.5. There are differences in the mathematical analysis of each Kerr effect.

The Kerr effect derivation is done well in Freisen.[57] The complete derivation is algebraically complicated and will be left to this reference.[57] It involves solving the Helmholtz equation to find the allowed modes of propagation in the material and then using Maxwell's equations to find the electric and magnetic field components in these modes, matching boundary conditions at the interface between the material and free space and then solving for reflection coefficients. In a homogeneous medium uniformly magnetized along the z-axis, the dielectric tensor may be written as:

$$\overline{\overline{\boldsymbol{\varepsilon}}}=\begin{bmatrix} \varepsilon & \varepsilon' & 0 \\ -\varepsilon' & \varepsilon & 0 \\ 0 & 0 & \varepsilon \end{bmatrix} \tag{2.1}$$

Here the diagonal element of the tensor ε represents the normal interaction between light and the medium, while the off-diagonal term ε' is due to magneto-optic activity. Using this dielectric tensor, one can proceed with the mathematically complex calculation. Only the results are reported in this thesis.

For the polar Kerr effect the reflection coefficients are :

$$\begin{bmatrix} R_p \\ R_s \end{bmatrix}=\begin{bmatrix} \dfrac{n\gamma-\gamma'}{n\gamma+\gamma'} & \dfrac{\frac{\varepsilon'}{n}}{(\gamma+n\gamma')\cdot(n\gamma+\gamma')} \\ \dfrac{\frac{\varepsilon'}{n}}{(\gamma+n\gamma')\cdot(n\gamma+\gamma')} & \dfrac{\gamma-n\gamma'}{\gamma+n\gamma'} \end{bmatrix}\begin{bmatrix} I_p \\ I_s \end{bmatrix} \tag{2.2}$$

where $n=\sqrt{\varepsilon}$, $\gamma=\cos\theta$, $\gamma'=\sqrt{1-\sin^2\theta/n^2}$, where θ is the angle of incidence of the light.

For the longitudinal Kerr effect we have:

$$\begin{bmatrix} R_p \\ R_s \end{bmatrix}=\begin{bmatrix} \dfrac{n\beta-\beta'}{n\beta+\beta'} & \dfrac{\frac{\gamma\beta\varepsilon'}{n^2}}{(\beta+n\beta')\cdot(n\beta+\beta')\beta'} \\ -\dfrac{\frac{\gamma\beta\varepsilon'}{n^2}}{(\beta+n\beta')\cdot(n\beta+\beta')\beta'} & \dfrac{\beta-n\beta'}{\beta+n\beta'} \end{bmatrix}\begin{bmatrix} I_p \\ I_s \end{bmatrix} \tag{2.3}$$

where $n=\sqrt{\varepsilon}$, $\gamma=\sin\theta$, $\beta=\cos\theta$, $\beta'=\sqrt{1-\sin^2\theta/n^2}$.

Finally for the transverse Kerr effect we have:

$$\begin{bmatrix} R_p \\ R_s \end{bmatrix} = \begin{bmatrix} \frac{n\cos\theta-1}{n\cos\theta+1}\left\{1+\frac{\sin 2\theta \frac{\varepsilon'}{n^2}}{n^2\cos^2\theta-1}\right\} & 0 \\ 0 & \frac{\cos\theta-n}{\cos\theta+n} \end{bmatrix} \begin{bmatrix} I_p \\ I_s \end{bmatrix} \tag{2.4}$$

where $n=\sqrt{\varepsilon}$. Since there are no cross-terms in this reflectivity matrix, one will see no rotation of polarized light with pure p state or pure s state incident upon a surface. However if a mixed state is used, some rotation will be observed because s and p light are reflected differently.

It is also informative to think about the Kerr effect from a materials standpoint. If we include the Zeeman effect in the theory of dispersion, magneto-optical effects can be calculated. This can be seen from the following qualitative argument. Linearly polarized light will induce electrons to oscillate parallel to their plane of polarization – the plane of the electric field **E** in the light The regularly reflected light will have the same polarization plane as the incoming light, but a secondary electron motion due to the Lorentz force light, proportional to **m x E**, where **m** is the magnetization within the sample, will generate secondary amplitudes of reflected light. The superposition of the regularly reflected light with the secondary light will lead to a magnetization dependent polarization rotation. This argument shows that if the polarized light is in the same plane as the sample magnetization no Kerr rotation will be observed. This can be seen by the zero cross terms in the transverse Kerr effect matrix.

2.4 Summary of the Chapter

This chapter is intended to give the reader a basic understanding of the time resolved scanning Kerr effect microscopy system used to gather the experimental data in this thesis. Although not a definitive source, many references are given to papers that spell out the development and more precise details of the system.[21,53] An introduction to basic pump-probe experiments and the ultrafast lasers used in our experiments is given. The time-resolved scanning Kerr effect microscopy system is introduced, along with the quadrant detection system. Special attention is given to a discussion on issues that influence this the work in this thesis that are not otherwise published in literature. Finally, the magneto-optical Kerr effect is discussed.

3. Micromagnetic Simulation

This chapter discusses the technique used to do micromagnetic simulation, including the background, the algorithm used, as well as other potential variants that one could use. The micromagnetic simulation code is based upon pioneering simulation work from Hayashi, Mansuripur, Zhu and Bertram.[58] It solves the Landau-Lifshitz-Gilbert equation of micromagnetic dynamics using finite element methods. Our particular code was initially developed by Andrzej Stankiewicz, but its final form was a large part of the work in this thesis.

3.1 Landau-Lifshitz-Gilbert Equation

Magnetism is inherently quantum mechanical as is shown by the Bohr-van Leeuwen theorem,[8] however it is not tractable to solve quantum mechanical problems with billions of atoms as is the case in micromagnetics. Thus an approximate theory is needed that is more tractable. The phenomenolgical Landau-Lifshitz-Gilbert theory, as derived and discussed in section 1.3 of this thesis, is such an option. It has been a very reliable theory (see the successes in the magnetic recording field as examples!), and is the best starting point for a comparison with the experimental micromagnetic dynamic observations. This will be one of the most stringent tests of the LLG theory. Eventually, it is hoped that this comparison will push LLG beyond its limitations. Possibly it will show that a single damping constant is not enough to describe the dynamics, or that the Newtonian approximations involved are invalid. In this case, it may become necessary to go beyond the LLG theory.

3.2 Methods of Demagnetizing Energy Calculation

Since this is the most complex part of a micromagnetic simulation special attention will be devoted to this problem. A general solution of this problem can be found by noting the parallels with electrostatics using potential theory. This derivation is from Aharoni.[23]

If we define a reduced magnetization

$$\mathbf{m}(\mathbf{r}) = \frac{\mathbf{M}(\mathbf{r})}{M_s} \tag{3.1}$$

and we further define a reduced volume charge density λ_v and a surface charge density σ_s

$$\lambda_v = -\nabla \bullet m \text{ and } \sigma_s = m \bullet n \tag{3.2}$$

where **n** is the outward directed surface normal, the potential from the demagnetizing field at position **r** can be found by the integral

$$\Phi_d(\mathbf{r}) = \frac{J_s}{4\pi\mu_o}\left[\iiint \frac{\lambda_v(\mathbf{r}')}{|\mathbf{r}-\mathbf{r}'|}dV' + \oiint \frac{\sigma_s(\mathbf{r}')}{|\mathbf{r}-\mathbf{r}'|}dS'\right] \tag{3.3}$$

where $H_d(\mathbf{r}) = -\nabla\, \Phi_d(\mathbf{r})$. With another integration we obtain

$$w_d = J_s\left[\iiint \lambda_v(\mathbf{r})\Phi_d(\mathbf{r})dV + \oiint \sigma_s(\mathbf{r})\Phi_d(\mathbf{r})dS\right] \tag{3.4}$$

As beautiful as this closed solution may be, it is only calculable in the most trivial cases since it is a sixfold integral (three to calculate $\Phi_d(r)$ and three more to calculate w_d). To go beyond simple cases we need another form to evaluate numerically.

The approach in a finite element simulation is to compute as many steps of the problem analytically as possible. This approach can be traced back to Rhodes and Rowland.[59] The argument shown here is similar to that of Hayashi.[60] A dipole magnetic field that would be required to generate the known magnetization **M** is superimposed upon the center of each cell. Thus the demagnetizing field can be calculated as follows

$$\mathbf{H}_\mathrm{d} = -\sum_{cell} \iiint_{V'} \frac{\mathbf{M}(\mathbf{Q}')r^2 - (3\mathbf{M}(\mathbf{Q}')\bullet\mathbf{r})\mathbf{r}}{r^5}dV' \tag{3.5}$$

where integrations are carried out in the source cell V' and the distance vector Q' runs from the center of the cell to the observation point and its magnitude is denoted by r. If we further assume magnetization to be constant within each cell we can write this as a matrix equation as shown

$$\begin{bmatrix} H_d^{\,x} \\ H_d^{\,y} \\ H_d^{\,z} \end{bmatrix} = \sum_Q \begin{bmatrix} K_{xx} & K_{xy} & K_{xz} \\ K_{yx} & K_{yy} & K_{yz} \\ K_{zx} & K_{zy} & K_{zz} \end{bmatrix} \begin{bmatrix} M_x \\ M_y \\ M_z \end{bmatrix} \tag{3.6}$$

where K_{ij} are purely geometric terms called demagnetizing coefficients (note that these are slightly different from the demagnetizing factors N deiscussed in section 1.5. In vector notation this is

$$\mathbf{H}_{\mathrm{d}} = \sum_Q \mathbf{M}(\mathbf{Q}) K(\mathbf{r}-\mathbf{Q}) \tag{3.7}$$

K_{ij} can be calculated as follows

$$\begin{aligned} K_{xx} &= -\iiint_{V'} \frac{r^2 - 3(x-x')^2}{r^5} dV' \\ K_{xy} = K_{yx} &= -\iiint_{V'} \frac{3(x-x')(y-y')}{r^5} dV' \end{aligned} \tag{3.8}$$

The other demagnetizing coefficients can be found by cyclic permutation on x,y or z. These integrals can be performed to yield demagnetizing coefficients in the form below

$$\begin{aligned} K_{xx} &= \sum_{i=0}^{1} \sum_{j=0}^{1} \sum_{k=0}^{1} (-1)^{i+j+k} \tan^{-1} \left| \frac{\left(K+k-\frac{1}{2}\right)\left(J+j-\frac{1}{2}\right)\Delta z \Delta y}{r_{ijk}\left(I+i-\frac{1}{2}\right)\Delta x} \right| \\ K_{xy} &= -\sum_{i=0}^{1} \sum_{j=0}^{1} \sum_{k=0}^{1} (-1)^{i+j+k} \ln \left| \left(K+k-\frac{1}{2}\right)\Delta z + r_{ijk} \right| \end{aligned} \tag{3.9}$$

where r_{ijk} is defined as

$$r_{ijk} = \sqrt{\left(I+i-\frac{1}{2}\right)^2 \Delta x^2 + \left(J+j-\frac{1}{2}\right)^2 \Delta y^2 + \left(K+k-\frac{1}{2}\right)^2 \Delta z^2} \tag{3.10}$$

Δx,Δy and Δz are the dimensions of each cell with indices I,J,K. The other demagnetizing coefficients can be found by permuting x,y,z along with I,J,K and Δx,Δy,Δz.

This is a starting point for demagnetizing calculations, but it alone is not enough. The assumption that the point dipole is at the center of every cell in this calculation is insufficient when the angle between adjacent spins is large (see for example

McMichael[61]). It is necessary to further improve the demagnetizing coefficients by volume averaging them (or calculating an average value for a point dipole at all positions within the cell). This has been done by Fukushima et al.[62] These volume averaged demagnetizing coefficients are (in a compact computational form)

$$\begin{aligned}\left\langle K_{xx}\right\rangle &= \frac{1}{V}\sum_{i,j,k=1}^{3}(-1)^{i+j+k-1}\, sn(i)sn(j)sn(k)F1\big(x+ax(i),y+ay(j),z+az(k)\big)\\ \left\langle K_{xy}\right\rangle &= \frac{1}{V}\sum_{i,j,k=1}^{3}(-1)^{i+j+k-1}\, sn(i)sn(j)sn(k)F2\big(z+az(k),x+ax(i),y+ay(j)\big)\end{aligned} \tag{3.11}$$

where the arrays ax,ay,az and sn are defined as follows

$$\begin{aligned} &ax(1)=-\Delta x \qquad ax(2)=0 \qquad ax(3)=\Delta x \\ &ay(1)=-\Delta y \qquad ay(2)=0 \qquad ay(3)=\Delta y \\ &az(1)=-\Delta z \qquad az(2)=0 \qquad az(3)=\Delta z \\ &sn(1)=1 \qquad sn(2)=2 \qquad sn(3)=1 \end{aligned} \tag{3.12}$$

and the functions F1 and F2 are defined as

$$\begin{aligned} F1(x,y,z) &= xyz\tan^{-1}\left(\frac{yz}{xd}\right)+\frac{1}{2}y(z^2-x^2)\ln|d-y|+ \\ &\frac{1}{2}z(y^2-x^2)\ln|d-z|+\frac{1}{6}(y^2-z^2-2x^2)d \end{aligned} \tag{3.13}$$

$$\begin{aligned} F2(x,y,z) &= -xyz\ln|d+z|+\frac{1}{6}y(y^2-3z^2)\ln|d+x|+\frac{1}{6}x(x^2-3z^2)\ln|d+y|+ \\ &\frac{1}{2}x^2y\tan^{-1}\left(\frac{yz}{xd}\right)+\frac{1}{2}y^2z\tan^{-1}\left(\frac{xz}{yd}\right)+\frac{1}{6}z^3\tan^{-1}\left(\frac{xy}{zd}\right)+\frac{1}{3}xyd \end{aligned}$$

and *d* is defined as

$$d=\sqrt{x^2+y^2+z^2} \tag{3.14}$$

As before other formulas come from permutations of the coordinates.

There are a number of general features of this calculation that can aid in its computation. Regardless of which set of demagnetizing coefficients are used, note that they only depend upon the distance between two cells and not their absolute position. Thus, the coefficients can be stored in a much smaller portion of the memory.

Note also, that the form in eqn 3.7 has an inner sum, which amounts to a discrete convolution, as long as the cell positons are periodic. This sum can be computed by Fast Fourier Transform techniques, greatly increasing its computation speed (Hayashi [58]). The drawback is that with periodic cells you cannot have an adaptive cell size.[63] Adaptive cell size would allow you to have small cells only where necessary (for example domain walls) and larger cells where they can be allowed (for example domains) thus speeding up calculation as less cells are needed. In our simulation we have chosen to use FFT techniques instead of adaptive cell size. This gives us the benefit of faster simulations, which is especially important in our case of magnets several micrometers in size, but prevents the use of odd shaped cells for non-rectangular boundaries (ie circular samples).

3.3 Coordinate Systems

One of the first problems in solving the LLG equation is determining which coordinate system to use to represent the magnetization components. The two common

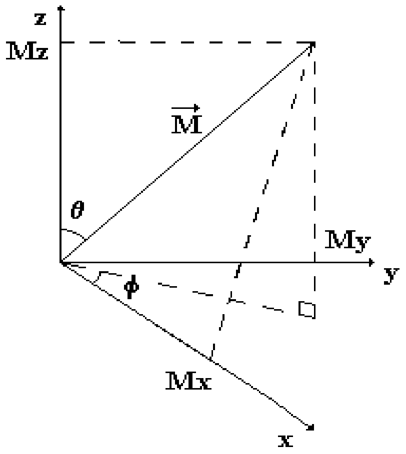

Figure 3.1. Coordinate systems in which micromagnetic simulation can be carried out. Magnetization can be specified by Cartesian coordinates (x,y,z) or by spherical angles (θ,ϕ)

ones are Cartesian and spherical coordinates. See figure 3.1 detailing both coordinate systems. Both have advantages and drawbacks.

In spherical coordinates there are only 2 degrees of freedom in the LLG equation and this can easily be captured in the coordinate system. Since the length of all magnetization vectors are constant, only the magnetization angles θ and ϕ are needed for each point. The constraint of constant magnetization (see section 1.3) is unconditionally satisfied by this choice. The drawback is that when the polar angle θ approaches 0 or π, the azimuthal angle ϕ is no longer uniquely defined. This prevents any LLG calculations in this regime. By carefully choosing the orientation of the problem to be solved, this issue can usually be avoided. If it cannot it may become necessary to use multiple coordinate systems within the same problem (Nakatani [59]), which becomes quite cumbersome. To date we have not encountered any problems that cannot be solved within a carefully chosen single coordinate system.

In Cartesian coordinates, the problem of ϕ being undefined is non-existent. This is a significant convenience. However, the constraint of constant magnetization is not as easily satisfied. Due to round off error it is possible that the length of the magnetization vector in a cell will change over time. If this becomes significant, one solution (Nakatani [59]) is to independently calculate two magnetization vector components and use the constraint

$$M_z = \pm\sqrt{M_s^2 - M_x^2 - M_y^2} \qquad (3.15)$$

to determine the third component. Since this only determines the absolute value of a component, it is necessary to choose this component when its value is sufficiently far from zero that its sign can be assumed.

In our simulation we use both sets of coordinate systems. Most of the calculation is done using the spherical magnetization angles, but it is much easier to calculate FFTs in Cartesian coordinates so we convert for the FFT and then convert back.

3.4 Form of Landau-Lifshitz-Gilbert Equation used in Simulation

In order to efficiently solve the LLG equation it is necessary to get it into the simplest form possible. We start with it in the form

$$\frac{d\mathbf{M}}{dt} = -\gamma \mathbf{M} \times \mathbf{H} + \frac{\alpha}{M_s} \mathbf{M} \times \frac{d\mathbf{M}}{dt} \tag{3.16}$$

In spherical coordinates we can obtain the equations

$$\frac{dM_\theta}{dt} = -\gamma H_\phi M_s - \alpha \frac{dM_\phi}{dt} \sin\theta \tag{3.17}$$

$$\frac{dM_\phi}{dt} \sin\theta = \gamma H_\theta M_s + \alpha \frac{dM_\theta}{dt}$$

where H_ϕ and H_θ are effective magnetic field components in those directions. Solving these equations for dM_ϕ/dt and dM_θ/dt yields

$$\frac{dM_\theta}{dt} = -\frac{\alpha \gamma M_s H_\theta}{1+\alpha^2} - \frac{\gamma M_s H_\phi}{1+\alpha^2} \tag{3.18}$$

$$\frac{dM_\phi}{dt} \sin\theta = \frac{\gamma M_s H_\theta}{1+\alpha^2} - \frac{\alpha \gamma M_s H_\phi}{1+\alpha^2}$$

We can now define a dimensionless variable t* where

$$t^* = \frac{t \gamma M_s}{1+\alpha^2} \tag{3.19}$$

This will transform these equations to

$$\frac{dM_\theta}{dt^*} = -\alpha H_\theta - H_\varphi, \qquad \frac{dM_\phi}{dt^*} \sin\theta = H_\theta - \alpha H_\phi \tag{3.20}$$

These are the equations used in the simulation.

3.5 Simulation Algorithm

The complete simulation code is listed in Appendix A. Two and three dimensional simulation codes are given. Most of the work was done using the two dimensional code

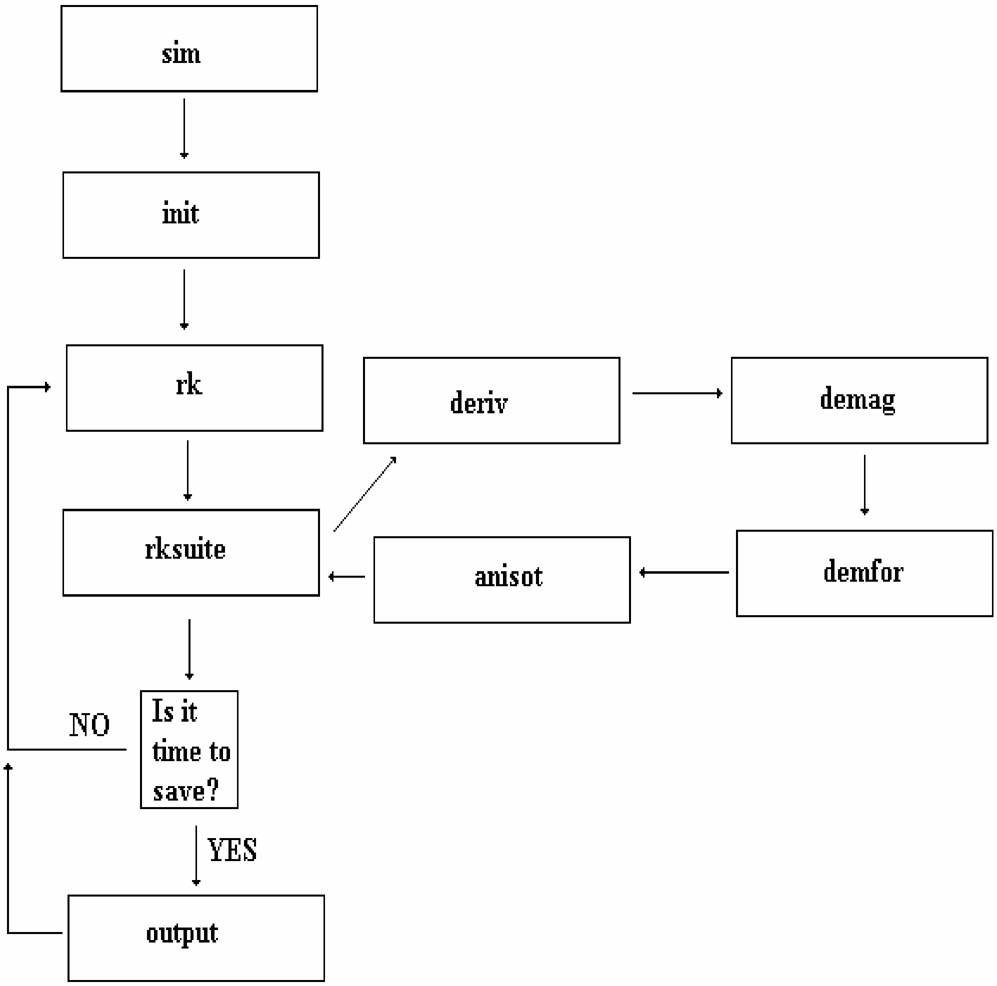

Figure 3.2 Flowchart for simulation program

since we use thin film samples which are well approximated by the two dimensional simulation and will run much faster. The program is broken up into several different files. The global variables are kept in global.inc. This is a file which is included in the major subroutines to pass global variables from one routine to another. In this routine, information like the size of the sample and the number of cells to be used is set. Sim is the programmable driver. In it, information such as the names of input and output files and the time that the problem is integrated over are set. Init is used to initialize variables such as the sample mask and demagnetizing coefficients. The most important of the initialized variables is the sample mask, which is a three dimensional array. In the two dimensional simulations, the first index runs from –2 to 2 and the second and third from 1 to nxmax and 1 to nymax respectively. If a cell (x,y) is contained within the sample, then mask(0,x,y) will be one, if that cell is outside the sample, then it is zero. The other elements are used for exchange calculations, mask(-1,x,y), specifies if the cell to left of (x,y) is in the sample for exchange calculations; mask(1,x,y) is to the right; mask(-2,x,y) is the cell below; and mask(2,x,y) is the cell above. This allows for odd shaped samples to be used in simulation. Rk is used to condition the program for using the 4th order variable stepping Runge-Kutta solver rksuite, which was written at Southern Methodist University [64]. Output is done in the output routine. Various components of the magnetic field are calculated in the other routines. Demag calculates the demagnetizing field (as well as exchange) using FFTs. Code is written to use both the built in FFTs on the SGI system and to use FFTW (the fastest FFT in the west) which was written at MIT [65]. Demfor contains the formulae used for demagnetizing coefficients. Anisot calculates anisotropy fields. Deriv calculates the derivatives dM_θ/dt and dM_ϕ/dt as required for rksuite. Interrupt is used to restart the program whenever the queue is reset on Aurora, a Silicon Graphics SGI-Origin 2000, located at the University of Alberta.

The program begins in sim to figure out what problem is being done and then goes to

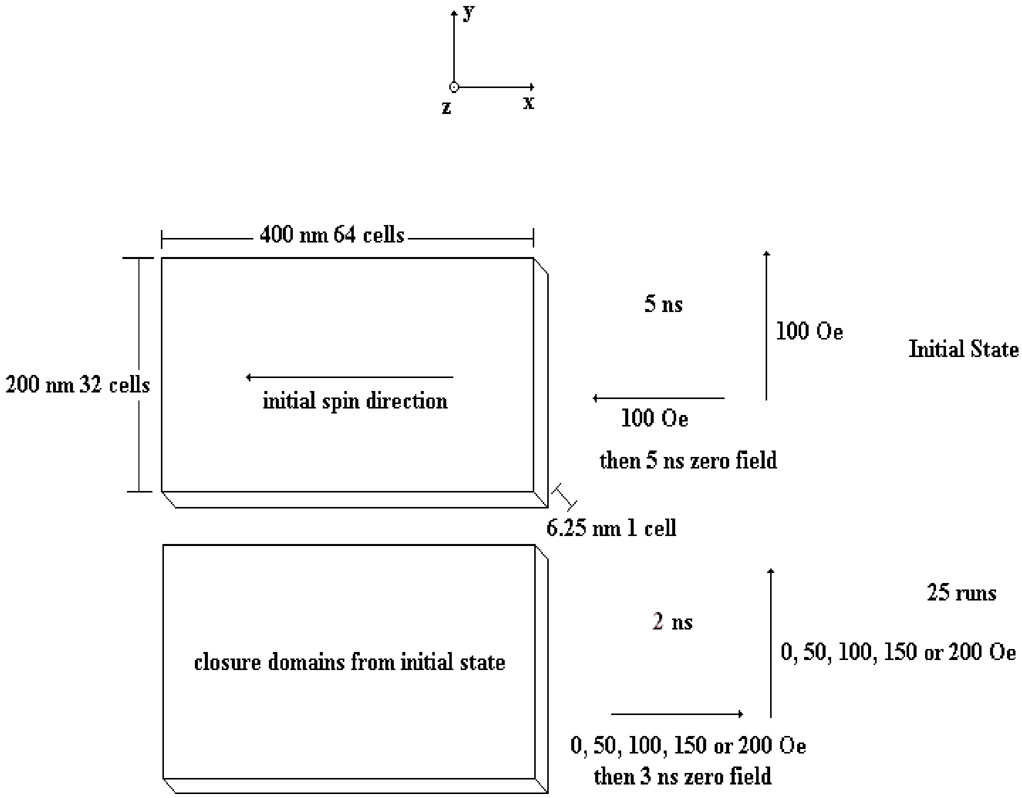

Figure 3.3 Initial test problem run with Roger Koch to test our micromagnetic code

init to initialize variables. It then goes into rk to set up to take a Runge-Kutta step and calculates the various magnetic fields using demag, demfor and anisot before stepping forward with rksuite solving the equations defined in deriv. The time steps are done with a variable stepper. The code measures the change in the magnetization angles (θ,ϕ) and accepts a step if this change is below a specified tolerance (which can be set in the sim routine using the variables tol and thres). If a step is sufficiently far below the error limit, it will attempt a larger time step next time,. If a step exceeds error limits, it will discard that step and attempt a smaller step in time. Periodically it saves the output using output. The flowchart is shown in figure 3.2

3.6 Benchmarking the code

The first test when the micromagnetic simulation code was written was to ensure that its calculations were correct. The National Institute of Standards and Testing (NIST) has a series of standard problems[66] that can be used to test magnetostatic simulations, but they do not address dynamic problems. They are a starting point, but do not directly apply to our code. Our code was run on the same problems as Roger Koch's micromagnetic simulation code.[54] This was the same series of problems which has been run using several major micromagnetic simulation programs.[67] In these problems, the sample is 400 nm x 200 nm x 6.25 nm. It is divided into cubic cells with linear dimension 6.25 nm to make a grid of 64 x 32 x 1 cells. Material parameters used are saturation magnetization $4\pi M_s$=10 kGauss, exchange constant 10^{-6} erg/cm and damping constant α=0.01. To calculate an initial state, we start with all spins pointing in the negative x direction (see figure 3.3). There is a field of –100 Gauss in the x direction and 100 Gauss in the y direction. The sample has 5 ns to equilibrate. Then it is left in zero external field for 5 ns. With this initial state, we have a zero risetime DC magnetic field pulse of 0, 50, 100, 150 and 200 Gauss along the y axis and 0, 50, 100, 150 and 200 Gauss along the x axis for 2 ns. Then the sample is allowed to equilibrate in 0 Gauss for 3 ns. This makes for twenty-five runs in total. We expect to see small details that are different due in a large part to exchange energy. The exact theory of exchange holds on the atomic level and we must make assumptions to implement it with larger cells.

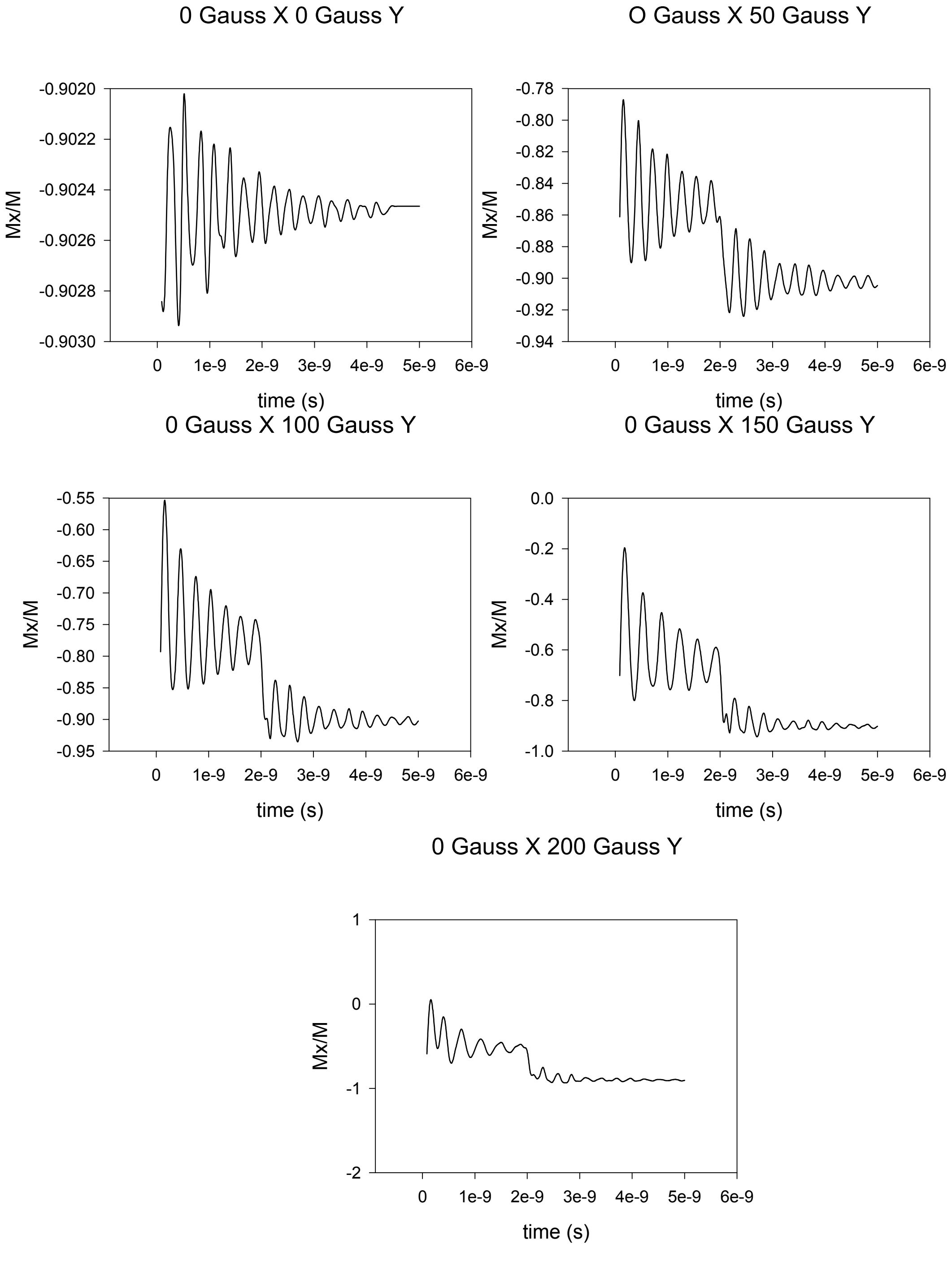

Figure 3.4 Roger Koch's simulation comparison. Runs with 0 Gauss along the X axis

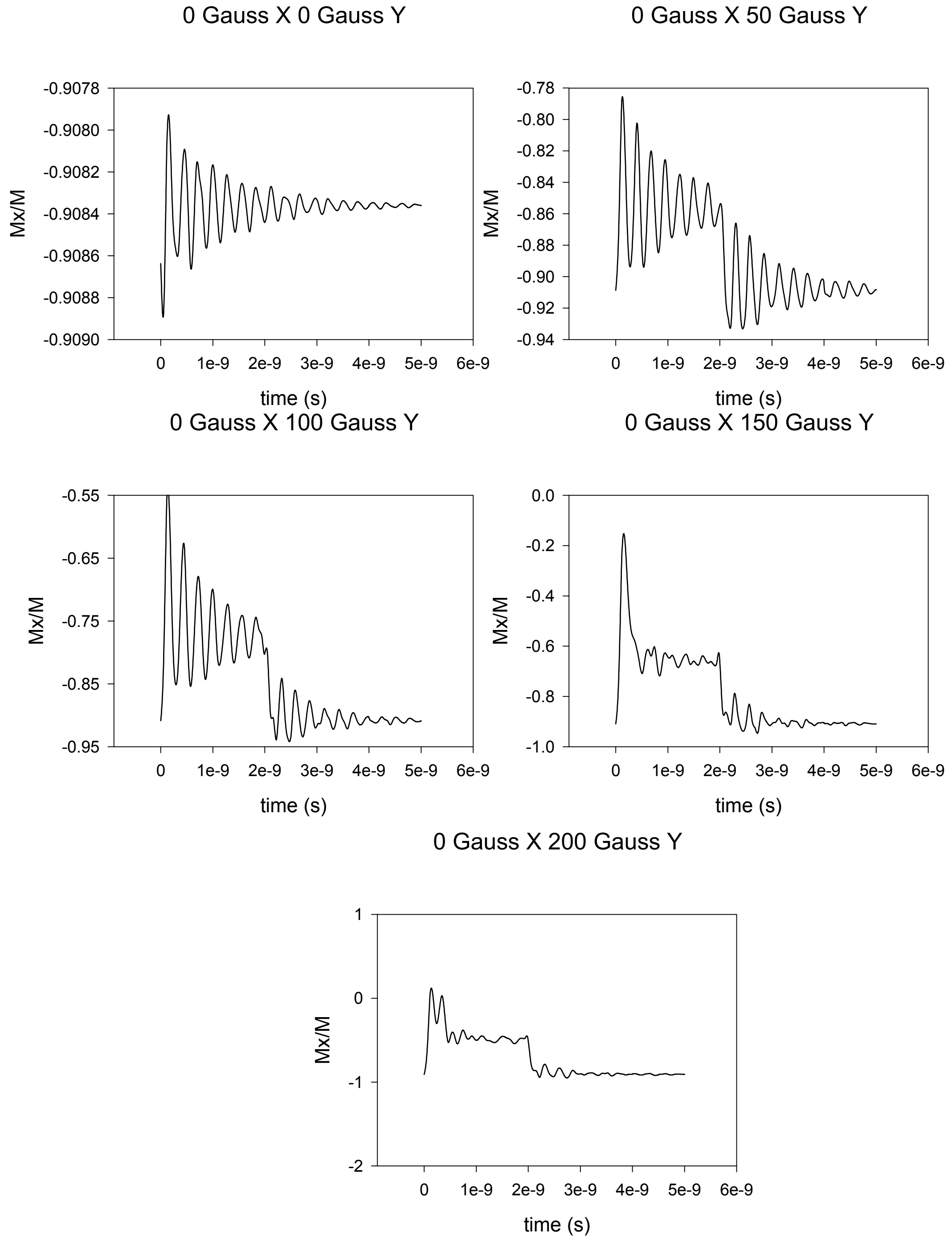

Figure 3.5 Our simulation for comparison with Roger Koch. Runs with 0 Gauss along the X axis

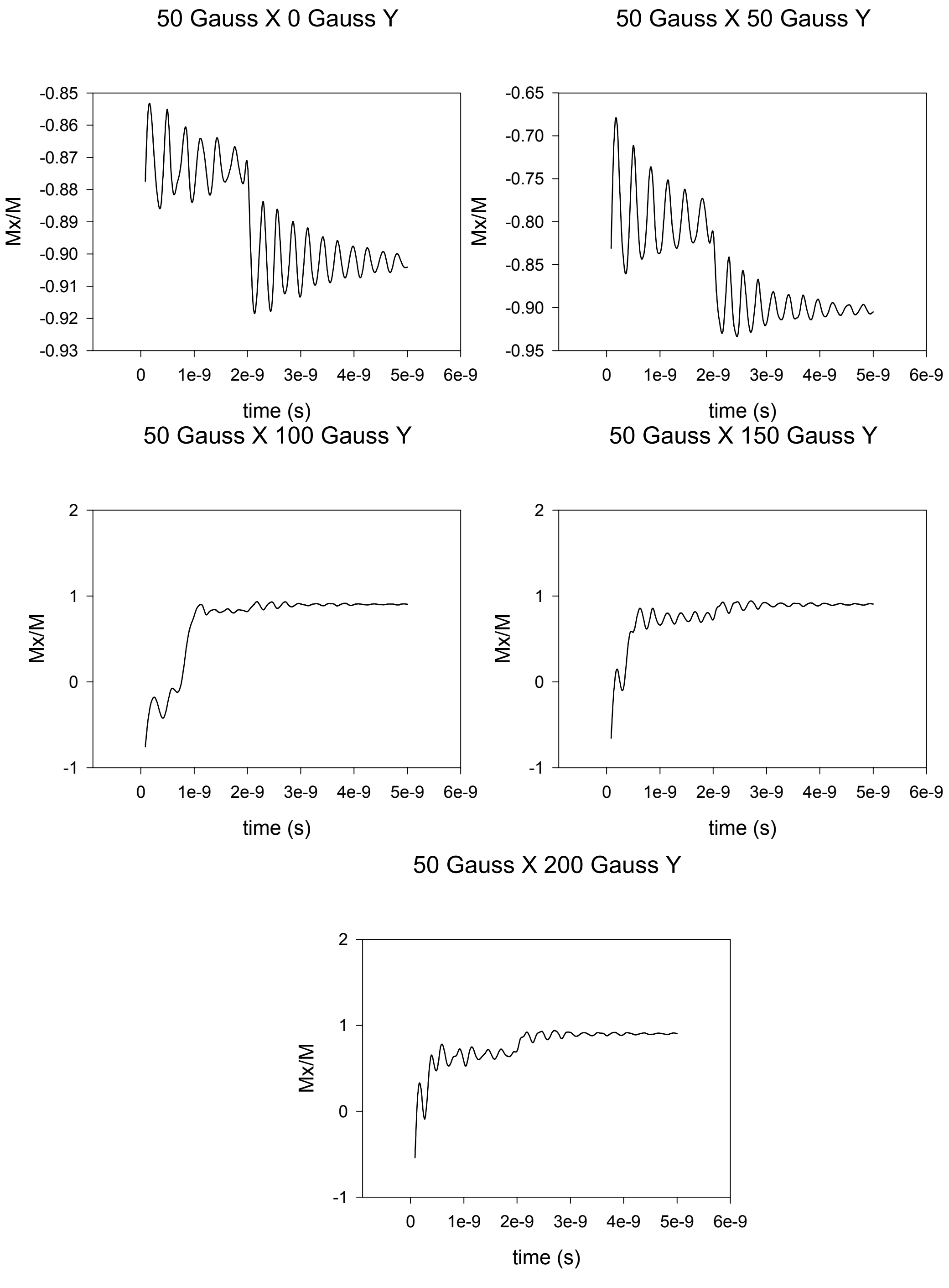

Figure 3.6 Roger Koch's simulation comparison. Runs with 50 Gauss along the X axis

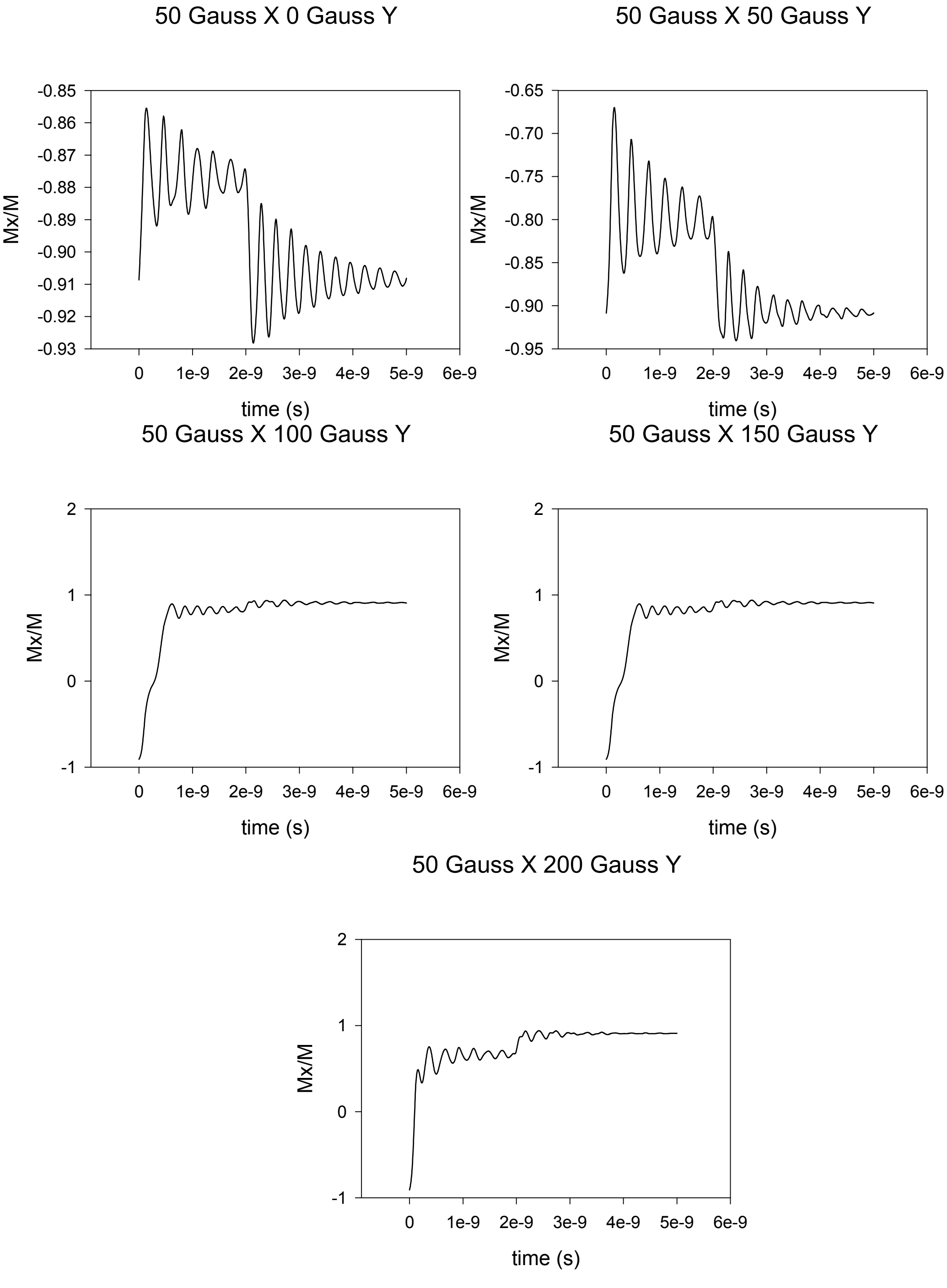

Figure 3.7 Our simulation for comparison with Roger Koch. Runs with 50 Gauss along the X axis

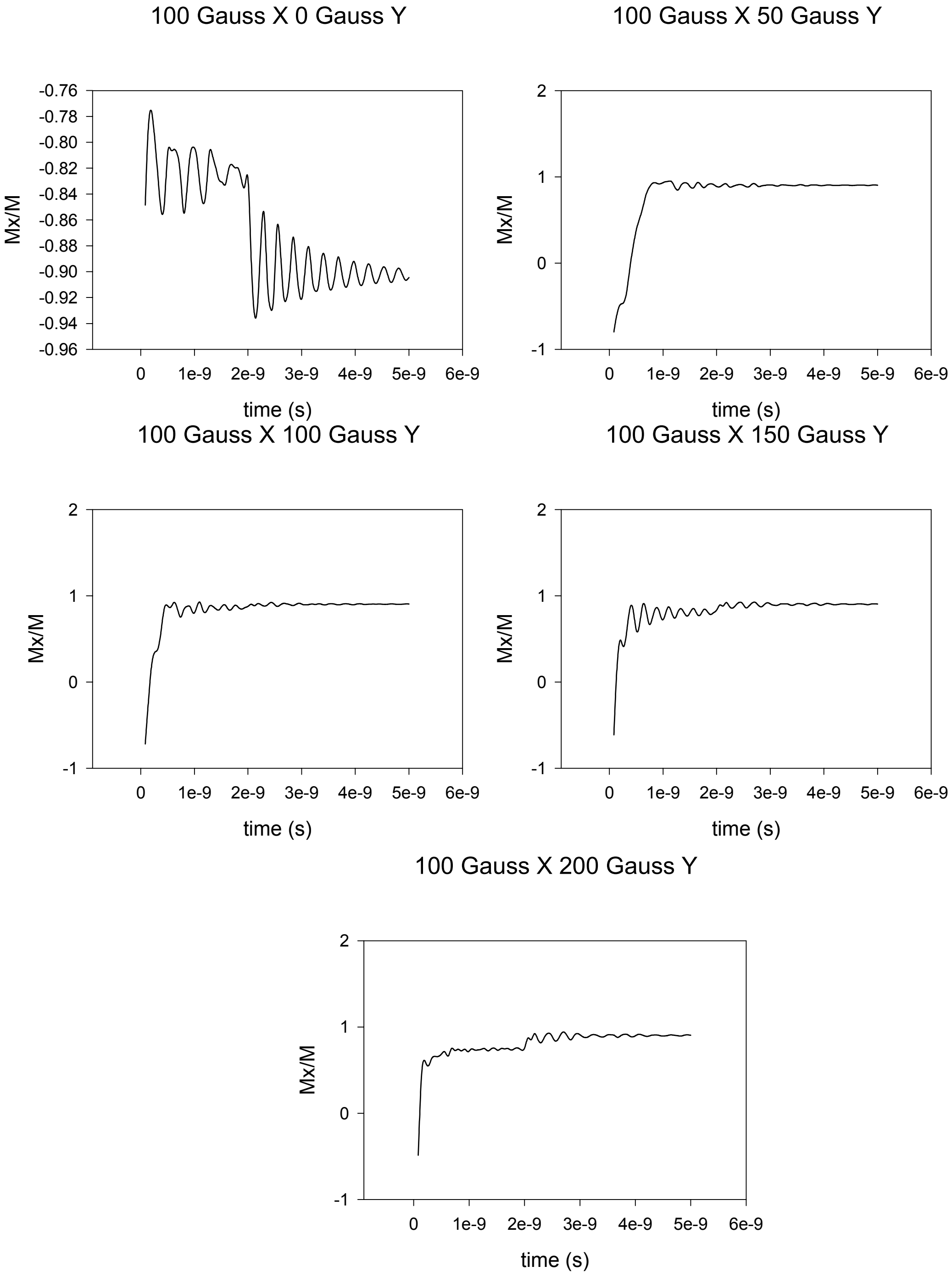

Figure 3.8 Roger Koch's simulation comparison. Runs with 100 Gauss along the X axis

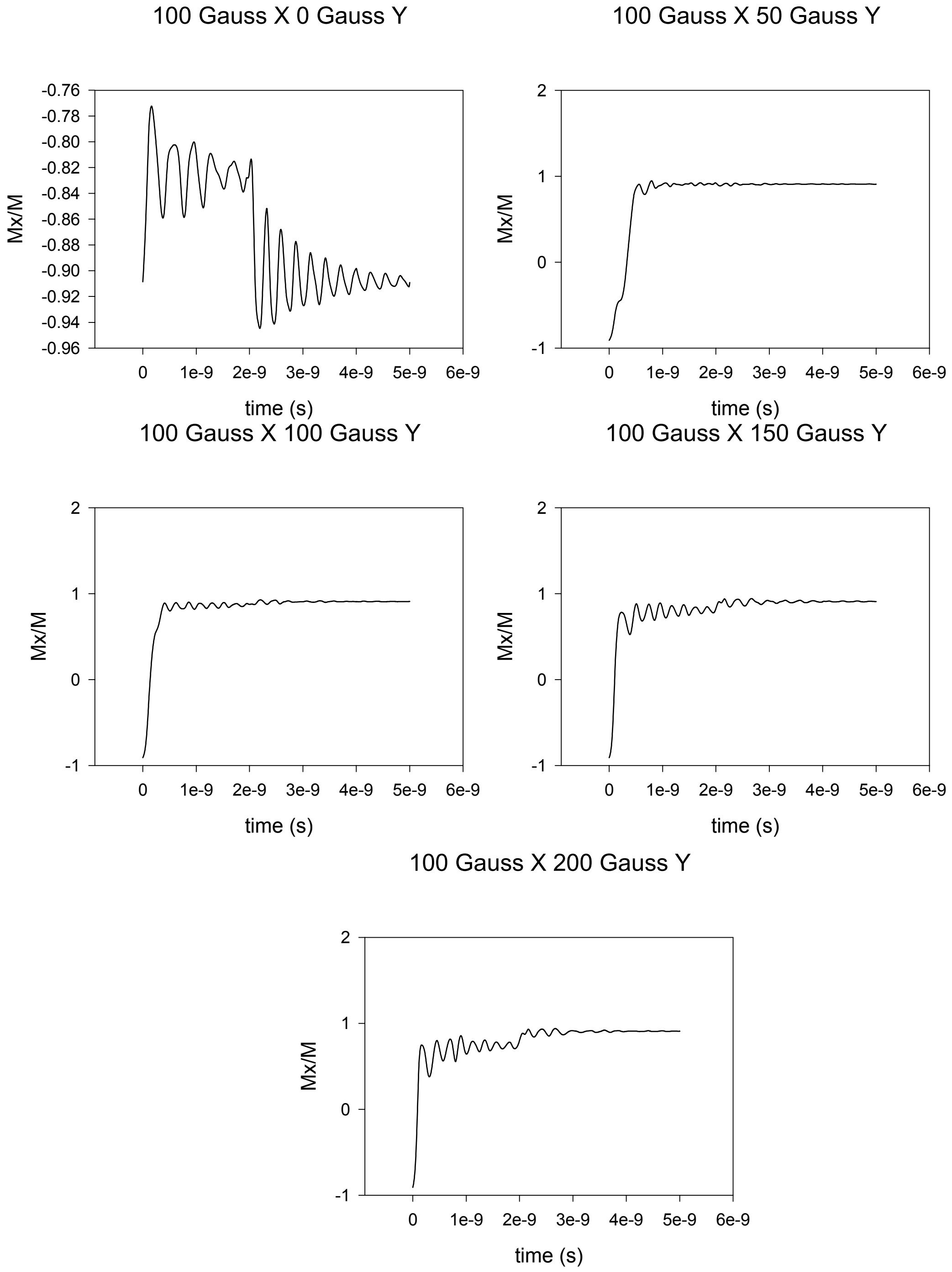

Figure 3.9 Our simulation for comparison with Roger Koch. Runs with 100 Gauss along the X axis

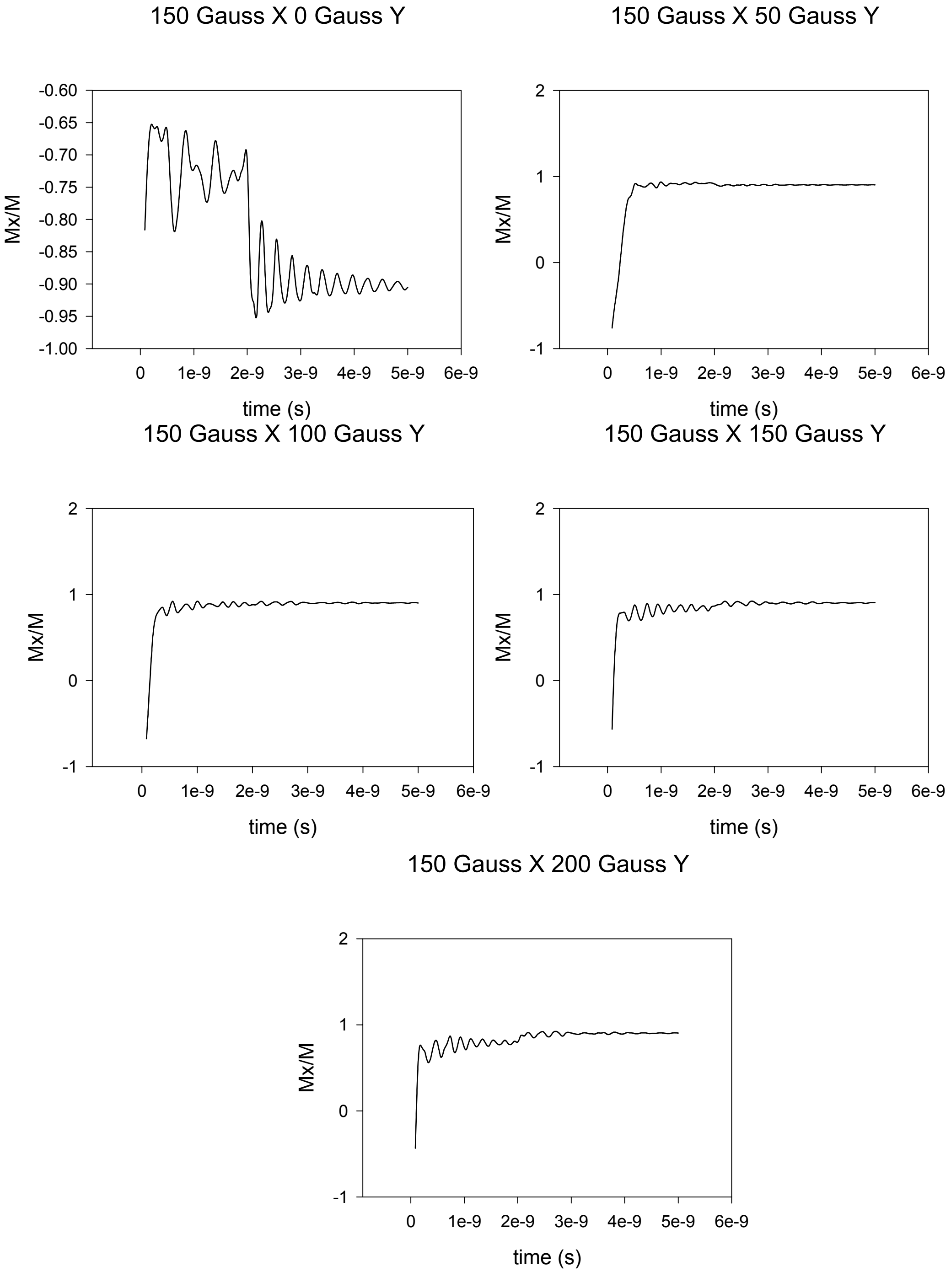

Figure 3.10 Roger Koch's simulation comparison. Runs with 150 Gauss along the X axis

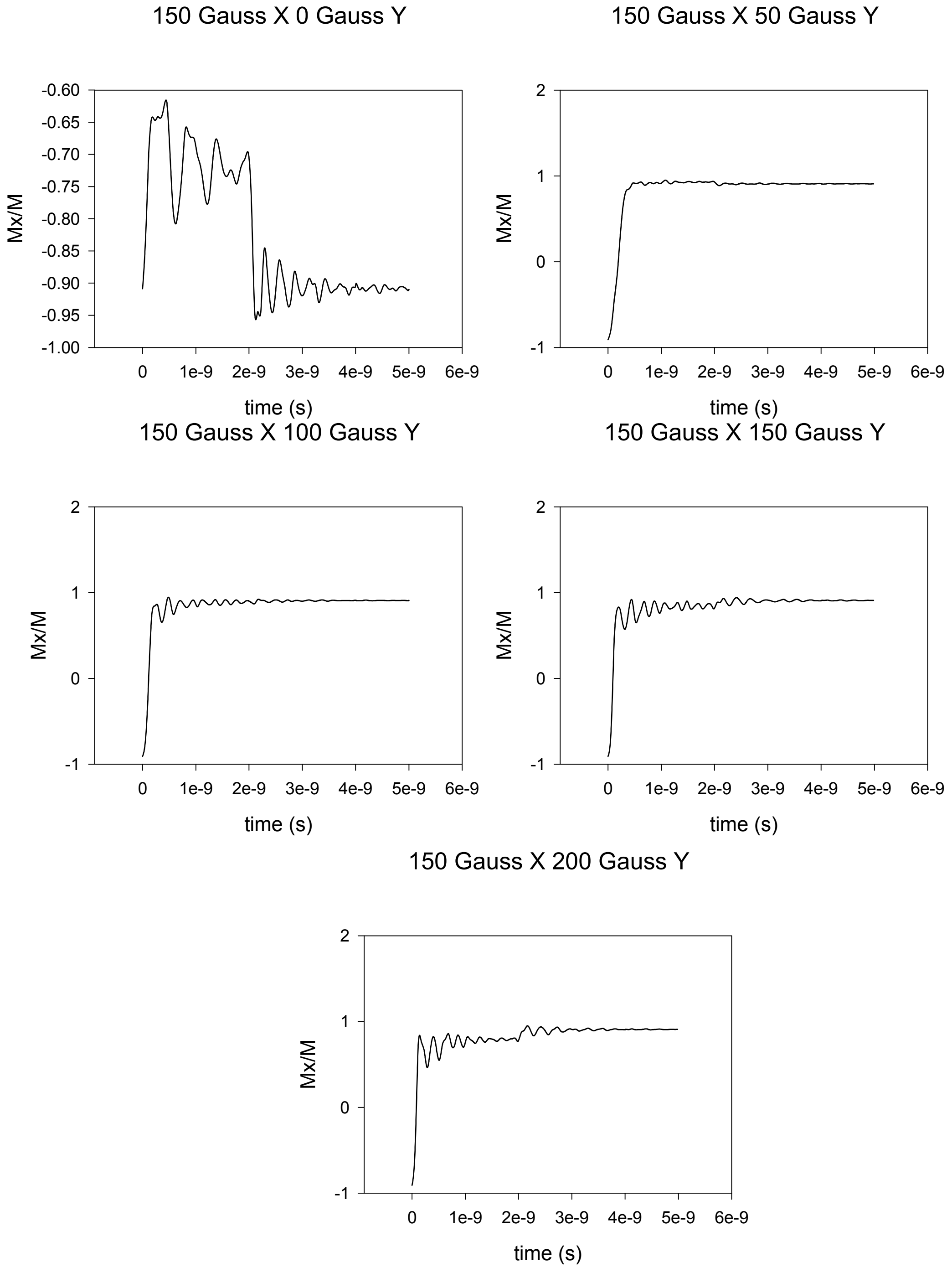
150 Gauss X 0 Gauss Y

150 Gauss X 50 Gauss Y

150 Gauss X 100 Gauss Y

150 Gauss X 150 Gauss Y

150 Gauss X 200 Gauss Y

Figure 3.11 Our simulation for comparison with Roger Koch. Runs with 150 Gauss along the X axis

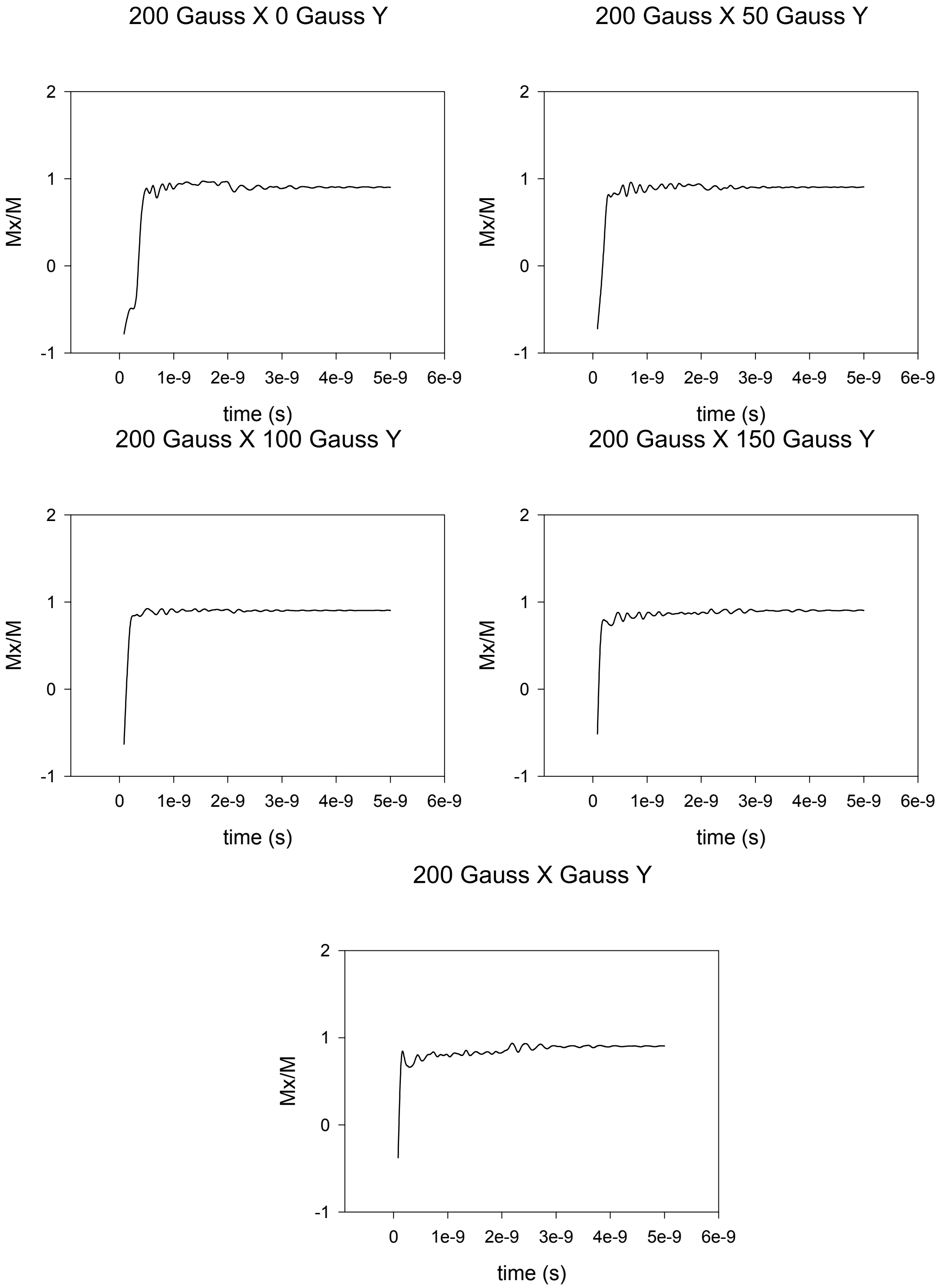

Figure 3.12 Roger Koch's simulation comparison. Runs with 200 Gauss along the X axis

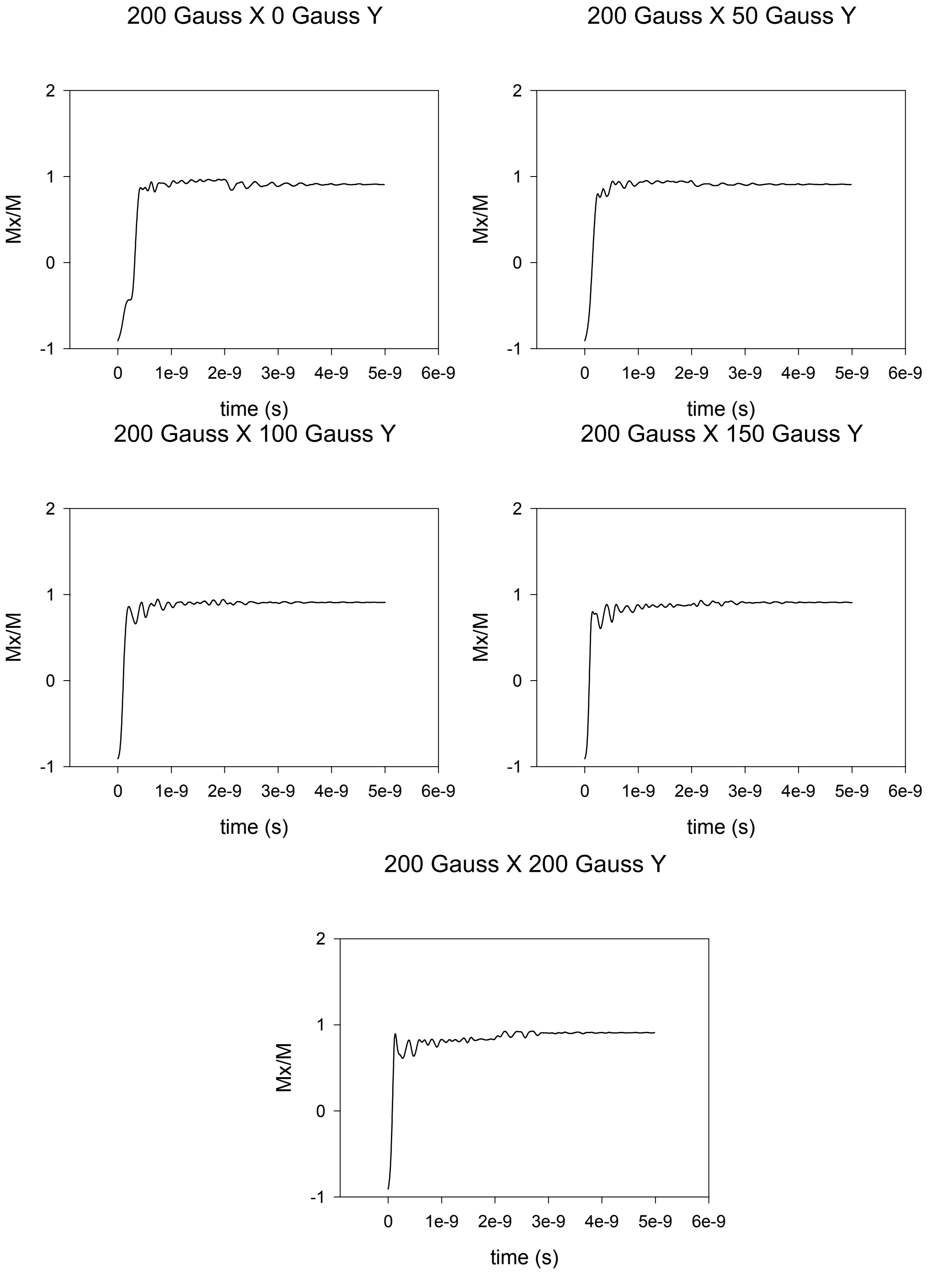

Figure 3.13 Our simulation for comparison with Roger Koch. Runs with 200 Gauss along the X axis

A comparison between Koch's results and ours is shown in figures 3.4-3.13, with five plots each with the same magnetic field along the long axis of the sample, but with varying magnetic fields along the short axis. Plotted on the y-axis is the magnetization in the x-direction (the long axis) integrated over the entire sample, normalized by the total magnetization of the sample. Time is plotted along the x-axis. In each of the twenty-five cases, similar dynamics is seen. The large scale sample behavior (whether it switches or doesn't switch) is the same in both cases. Rise times and oscillations have similar periods and shapes. This comparison is successful. It shows that our simulation behaves the same as other existing magnetization dynamics simulations on a simple problem.

These simulations show a wide cross-section of what is possible in magnetization dynamics. If a magnetic field larger that the coercive field of a sample is applied along its long axis (the initial direction of magnetization), it will switch its direction of magnetization by 180 degrees. If, in addition, another magnetic field is applied along the short axis of the field, the long axis field required to switch magnetization direction is reduced.[68] The change in magnetization when a sample switches magnetization direction is accomplished in this zero temperature simulation by precession of the various spins within the sample. This precession can be coherent throughout the sample, or incoherent between different domains. When it is coherent, periodic resonance oscillations can be observed within the sample. This is the magnetization of the spins undergoing a damped ferromagnetic resonance. A coherent rotation is usually faster than an incoherent one, so often a short axis field is added to speed up the reversal. When coherent rotation is observed, if it is caused by a short pulse the final equilibrium state (whether or not it switches) can be determined by pulse length alone as in the work of Hillebrands.[48]

3.6.1 Speed of Computation Comparison

The simplest comparison to make is the time needed to run a problem. One way to look at this is in terms of "expansion time", this is the ratio of the time of computation to the time the actual magnetic dynamical event will take. Koch reports an expansion time of $6.4 * 10^{10}$ using a 450 MHz pentium for this set of problems. On other slower IBM machines, he reports that it this can slow to ~ 2 * 10^{11}. We find a 1.15 x 10^{11} expansion time using a 233 MHz pentium, which is in this ballpark.

3.6.2 Issues Uncovered While Benchmarking

This good comparison in the standard problem run with Roger Koch was not simple to achieve. It took several tries to get the same parameters between our simulation and Koch's one. There are other runs with slightly varying parameters stored on CDs. The major difference between the different attempts is the way exchange is handled on boundaries. In order to explain this issue and the different options, we need to look further at exchange energy and how it relates to other energy terms.

Of the energy terms we are considering as important to magnetism, on the interatomic scale, exchange will dominate. It will be the largest energy term and will tend to align all the atoms spins as long as the region of interest remains small enough. How small a region we need to look at depends upon the other energy terms involved. Two different length parameters can be found. Both are known as exchange lengths. One exchange length is found by comparing anisotropy energy with exchange energy. This exchange length is given by

$$l_{ex}{}^{A} = \sqrt{\frac{A}{2K_u}} \tag{3.24}$$

where A is the exchange constant and K_u is anisotropy constant. If we take A as 10^{-6} erg/cm and K_u as 10^4 erg/cm^3 which are typical values for permalloy, we get an exchange length of about 70 nm.

One can get another exchange length by comparing demagnetizing energy with exchange energy. This exchange length is given by

$$l_{ex}{}^{D} = \sqrt{\frac{A}{2\pi M_s{}^2}} \tag{3.25}$$

taking the saturation magnetization M_s to be 860 Oe. This gives an exchange length slightly below 5 nm.

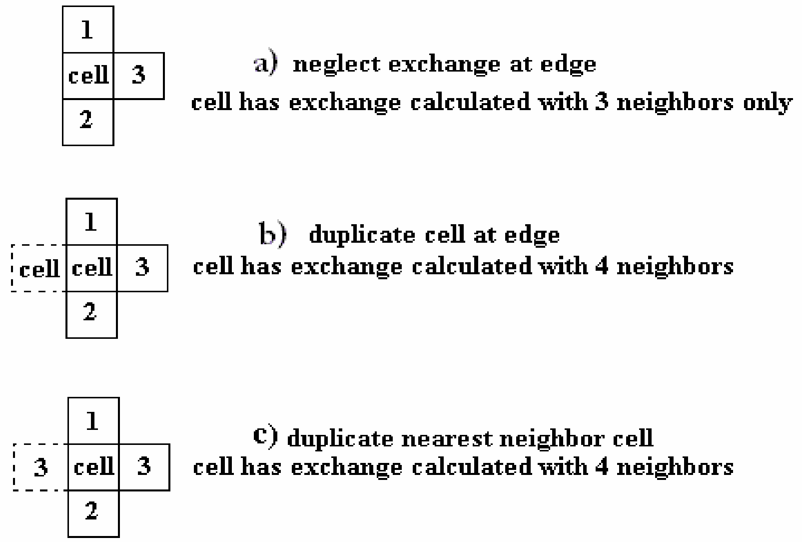

Figure 3.14 Various methods of handling the exchange interaction at boundaries. With sufficiently small cells they will all give same result. **a)** is the traditional (Zhu) method, b) and c) are departures from it that help ensure Maxwell's equation boundary conditions are satisfied for larger than optimal cell size.

As long as the cell size is sufficiently small with respect to the exchange lengths, it is expected that the simulation will produce results that are independent of cell size. This statement is somewhat vague, and it required some amount of trial and error to determine in practice what size of were needed (see chapters 4 and 5).

When cells become large with respect to exchange lengths, the simulation begins to misrepresent the physical situation. There is less energy in exchange in the simulation then there should be in the experimental case. Only exchange energy is dependant upon cell size, other energy terms maintain their value. This eventually leads to discrepancy in the simulation by underestimating exchange energy. In cases where other energy terms are much larger than exchange, the simulation can still produce meaningful results with cells much larger than the exchange length. However, another problem can start to occur at the boundary of the sample. We know from Maxwell's equations that the derivative of the magnetization **M** normal to a boundary is constant across that boundary. Since there is no material outside the ferromagnet that means this derivative is zero on the magnet's edge. With sufficiently small cells this condition is trivially satisfied. Larger there introduce error in this boundary condition. This error can be corrected by carefully treating exchange at boundaries. Three options were tried. If a cell is outside the sample, it can be neglected for exchange calculation. This is the most traditional approach and the one advocated by Jimmy Zhu.[69] However, this leads to boundary condition problems when cell sizes are large. Two other options (see Figure 3.14 for a schematic representation of these) include replicating edge cells (3.14.b) or nearest neighbor cells (3.14.c). These will better fit the boundary conditions for larger cells. It was found that replicating edge cells gave very similar features to neglecting exchange at boundaries, but helped boundary conditions to better satisfy the boundary conditions. Using nearest neighbor cells, although boundary conditions are satisfied, does not always give the same dynamics. Switching is faster when nearest neighbor cells are used for exchange on boundaries. This is because the closure domains on the edge of the sample are not parallel with the applied magnetic field, whereas in general the spins in the center of the sample are. They will feel a larger torque from an external magnetic field and thus will switch first. The sample with nearest neighbor exchange will "drag" both the edge cell,

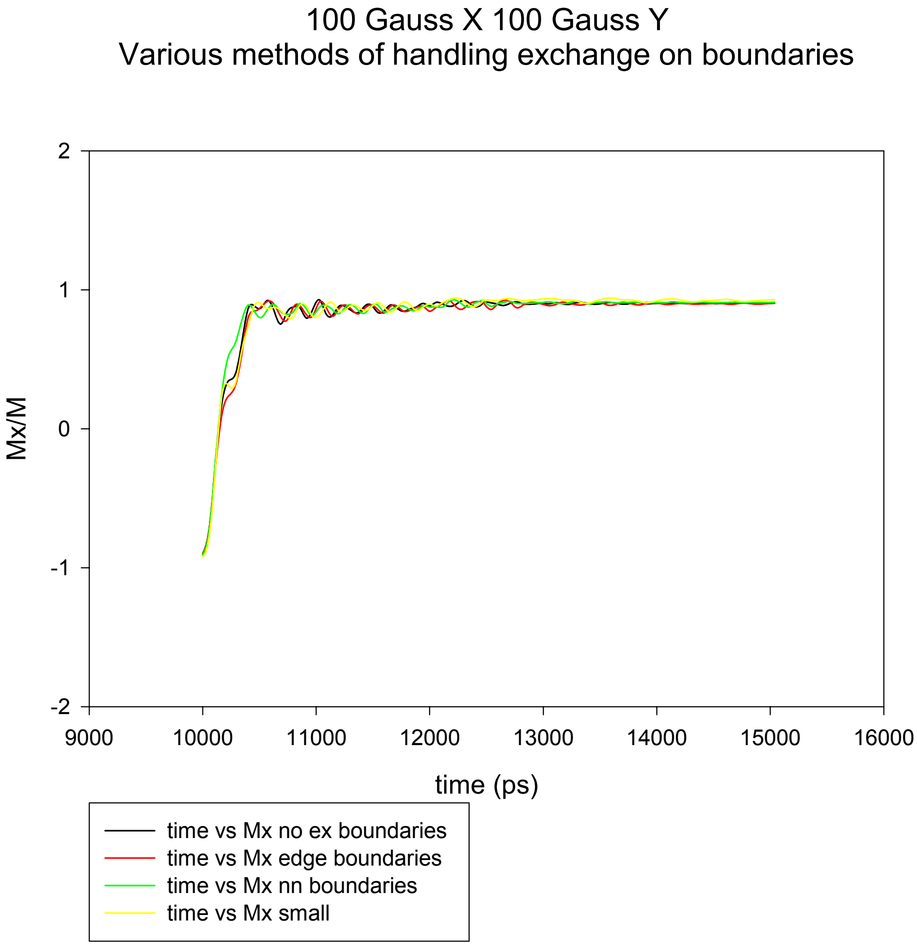

Figure 3.15. Effect of different boundary conditions on standard problem simulation with 100 Gauss in X and 100 Gauss in Y. Note there is little difference between no exchange along sample boundaries and repeating edge cells. Using nearest neighbor cells speeds up the reversal.

as well as the nearest neighbor, together when they begin to switch due to stronger exchange coupling. This starts the switch faster in the nearest neighbor sample and leads to artificially fast dynamics (ie faster rise times etc). This effect may arise slightly when edge cells are replicated for exchange, but it is far less significant. As an example we can use the case of 100 Gauss in X and in Y. Figure 3.15 shows the integrated Mx vs. time curves for each. Note that the nearest neighbor switch is significantly faster, but the other two switches take nearly the same amount of time.

Theoretically, the question of how to handle boundaries is even more complicated due to surface anisotropy.[23] This is the realization that a spin on the surface has a nearest neighbor on one side but none on the other and this affects exchange. Calculations have been done for a few atomic layers [70] that show that surface anisotropy can affect the atoms that are a few layers inward from the surface. Thus, there is some room for uncertainty on how best to handle exchange at surfaces in micromagnetic simulation.

3.7 Conservation of Energy

Another important test for the simulation code is to check that it conserves energy when there is no damping. A stringent test for this is a large angle magnetic motion, such as a magnetic reversal because it will be a more complex computation. A sample of the

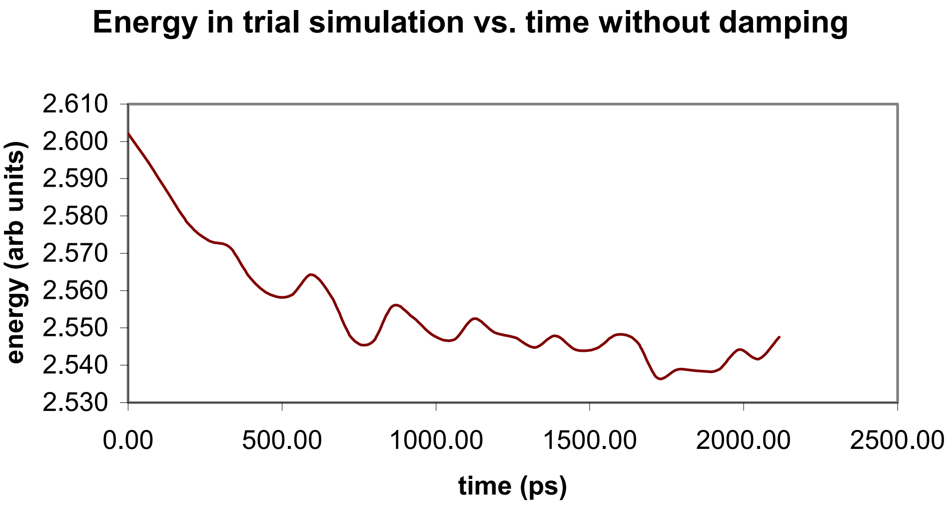

Figure 3.16. Energy in a trial simulation plotted against time. The sample loses about 2.5% of its total energy during the reversal. Energy loss is during the large angle motion at the start of the reversal and slows when this motion is complete

same size, shape and initial state and with the same parameters as in the previous benchmarking is used. It is then given a 300 Oe field along the x-axis so that it switches quite rapidly. This is a large “boost” of Zeeman energy, which as the sample switches is converted into exchange and demagnetizing energy. The sample does not reach an equilibrium, as there is no damping. The spins precess about an axis in the reversal direction with energy being converted between exchange and demagnetizing energy. A plot of the total energy vs. time is shown in figure 3.16. Throughout over 2 ns of motion, approximately 2.5% of the energy within of the sample is lost. The energy is lost most quickly during the rapid switch in magnetization and when the sample motion slows, the energy stays far more constant. In lower driving fields, it is expected that energy is better conserved.

3.8 Other Simulation Possibilities

Landau-Lifshitz-Gilbert micromagnetic simulations are not the only possible way to try to solve micromagnetic problems. Other methods exist, but they tend to be better suited for static problems or use a more complicated and experimentally unsupported damping term. Static simulations tend to be based upon the La Bonte iteration.[71] This is discussed in the upcoming section. More complex damping term simulations such as Bloch-Bloembergen [72] and Bar`yaktar [73] are discussed in the following sections.

3.8.1 La Bonte Iteration

If the problem is to determine the equilibrium magnetization configuration, the fastest method is likely the La Bonte iteration.[71] It is known to converge significantly faster than an LLG simulation.

In equilibrium, the magnetization in any cell will be aligned with the effective field in that cell. The La Bonte iteration is to make a reasonable guess for the magnetic field **H** (Only the external field would be known exactly. Exchange, anisotropy and demagnetizing fields are guesses.) and then align the magnetization **M** with **H**. This magnetization will change the overall field **H**, so a new **H** can be calculated with this **M**.

To iterate **M** is replaced by M**H**/H where **H** is calculated from the assumed **M**. Eventually, this technique converges to a solution but it is slow. In order to speed up the convergence, the correction from one term to the next

$$\partial\mathbf{M} = \frac{M\mathbf{H}}{H} - \mathbf{M} \tag{3.21}$$

is multiplied by a scalar factor w, which is chosen by how quickly it can make the calculation converge to a solution.

This technique will lead to an equilibrium configuration but is very poor for dynamics. It is very hard to pull a time scale of motion out of this technique. Also, all motion would have to be quasi-static as equilibrium values would be calculated throughout the motion. Likely the assumption of quasi-static motion breaks down.

3.8.2 Bloch-Bloembergen Equation

Another common form of damping is the Bloch-Bloembergen equations,[72] they assume that the longitudinal and transverse components of magnetization have different relaxation rates, thus allowing for change in the length of the magnetization vector. These equations are

$$\left.\frac{d\mathbf{M}}{dt}\right]_z = -\gamma\left[\mathbf{M}\times\mathbf{H}_{\mathbf{eff}}\right]_z - \frac{M_z - |\mathbf{M}|}{2T_1} \tag{3.22}$$

$$\left.\frac{d\mathbf{M}}{dt}\right]_{x,y} = -\gamma\left[\mathbf{M}\times\mathbf{H}_{\mathbf{eff}}\right]_{x,y} - \frac{M_{x,y}}{2T_2}$$

Here relaxation is a two stage process. The magnetization is reduced along a preferred axis, the direction of magnetization (in this case the z direction). Its precessional motion is slowed along the directions perpendicular to this preferred axis. T_1 is called the longitudinal relaxation time. It is the time the magnetization takes to shrink along the preferred axis. Processes that lead to change in magnitude of the magnetization vector are generally spin-lattice interactions. T_1 is also often called the spin-lattice relaxation time. Transverse components relax differently. This relaxation maintains absolute value of the magnetization. They do so with a relaxation time T_2. At this point, there is no convincing data that suggests that this approach is any better than an LLG simulation, although it is more complicated and has more free parameters (T_1 and T_2 replace α). With the success of LLG in magnetoelectronic applications, it makes sense to begin with an LLG simulation.

3.8.3 Bar'yaktar damping

Bar'yaktar [73] is far more general in his equation of motion allowing for directional dependence due to crystal symmetry (and its effect on for example exchange). He derives a magnetization dynamics equation as shown

$$\frac{d\mathbf{M}}{dt} = -\gamma \mathbf{M} \times \mathbf{H} + \gamma M_s \left\{ \alpha_{ik} H_i \mathbf{e_k} - \alpha_e a^2 \nabla^2 \mathbf{H} \right\} \qquad (3.23)$$

Here α_{ik} is a damping tensor which comes directly from the Dirac equation and α_e is damping due to exchange, a is the lattice constant of the material, $\mathbf{e_k}$ is a unit vector and summation on repeated indices is assumed. This equation does not conserve the length of the magnetization vector. Also, because the dissipative function in this equation is quite complicated in how it relates to the effective magnetic field **H**, the analysis of relaxation in the system is quite complicated. Ten damping parameters are needed to numerically solve this equation (vs 1 in LLG). It would be quite difficult to isolate and measure these different parameters, likely leaving many free parameters to simulation. It appears that no Bar'yaktar simulations have been carried out successfully and no values for the associated damping parameters exist. The only work to date [57] has been analytic calculation, which is perturbative in nature, relying upon the fact that the damping constants are small and can be viewed as perturbations. Results are similar to those from more traditional techniques. No definitive prediction or explanation of experiment appears to exist that shows Bar'yaktar damping is any better than the damping constant in the LLG equation. This may become possible with better experiments. Because the LLG equation is far more tractable and has not been shown to be inadequate, it is used for simulation and not Bar'yaktar.

3.9 Summary of the Chapter

In this chapter, the micromagnetic simulation is introduced. A short discussion on the Landau-Lifshitz-Gilbert equation (derived in chapter one) is given. The mathematically complex task of calculating demagnetizing energy is introduced with a few different methods for how it can be done. The problem of which coordinate system to use in a simulation calculation is given. The mathematical form of the LLG equation used in simulation is derived. The algorithm of the simulation code is explained. The two dimensional code is in Appendix A and the three dimensional code in Appendix B. The first trials to validate the code, by checking for energy conservation and by solving a standard problem and comparing our results to an established code are presented. The results are given, and a discussion of the issues encountered during the comparison is given. Alternative methods to a micromagnetic LLG simulation are introduced, with a brief discussion on their strengths and weaknesses. These methods are La Bonte's iteration, the Bloch-Bloembergen equation and Bar'yaktar damping. It is hoped that after reading the chapter, the reader will be familiar with the issues regarding micromagnetic simulation and understand the choices made in writing our code. This detailed comparison with experiment could not have been performed without the code development reported here.

4. Ferromagnetic Resonance

In this chapter we will look at the ferromagnetic resonance experiments that were used first as a check of the simulation and later as a significant test. This is a good first test because it is a small angle excitation. This is a favorable condition for a single damping constant Landau-Lifshitz-Gilbert simulation because motion will be strongly driven by long wavelength magnetostatic modes, which the simulation captures well. Because the motion does not have small features (such as domain walls) possibly larger cells can be used. The first tests were done using the simulation to reproduce data from Wayne Hiebert's master's thesis.[73] Later results are from experiments done by Miro Belov and the author to find the influence of a patterned defect in ferromagnetic resonance.

4.1 Experimental Details

The first set of data was obtained by Wayne Hiebert. Experimental details can be found in Freeman et al.[52.73] The data was gathered with the dye laser and the system discussed in chapter two. The sample was excited with a biased photoconductive switch [74] made of GaAs with gold interdigitated leads patterned on it. A schematic of the switch

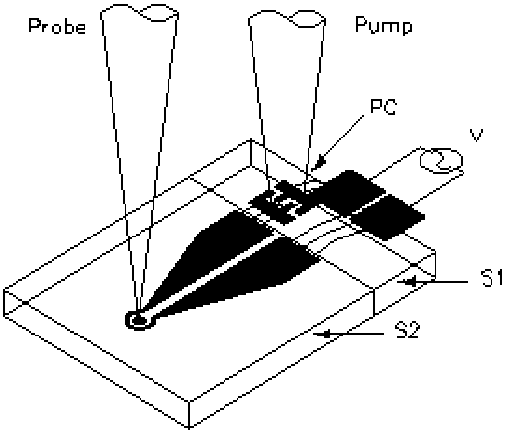

Figure 4.1 Schematic of a sample positioned in a gold coil with a GaAs photoconductive switch (PC) for pumping as in first ferromagnetic resonance experiments. The probe beam shines on the magnetic sample within the coil. S1 is the sample containing the photoconductive switch that is mounterd on S2, the patterned ferromagnet inpositioned inside a gold coil.

with a sample is shown in Fig 4.1. When light is shined on the switch, it conducts due to electron-hole pair creation in the GaAs. Typically, under these conditions it has a time-averaged resistance of 10 kOhms. Electron-hole recombination exponentially raises the resistance after the pump pulse ends. The current pulse has a half-life around 400 ps. When there is no light on the switch, its resistance is greater than 30 MOhms. When the switch was illuminated with the pump beam and thus turned on, current flowed through the coil exciting the permalloy sample inside it. The permalloy sample is biased by a DC magnetic field in the plane. The current in the coil tips the magnetization, making it precess about the bias field. It oscillates at its resonance frequency. This is detected at some time later with the probe beam. The detection is done with a lockin amplifier at the frequency of the AC bias voltage on the photoconductive switch. Time delay of the probe pulse is varied with an optical delay line.

The later results were gathered using the set-up described is section 2.2 and pictured in Fig 2.4. Te experimental system with a photovoltaic cell is easier to operate because there is no need to use a photoconductive switch. Photoconductive switches are difficult to use because they can overload and be damaged quite easily if too much laser power shines upon them, if they are subject to an electrostatic discharge or if too much current flows in them. Also, it is very hard to shape the current pulse because electrical reflections can occur at the bonds between the sample and the switch. It is almost unavoidable to have some reflections in the system. Reflections can be minimized by keeping the distance between the switch and the sample to a minimum. This is hard to do because the probe beam is focused with a microscope objective and the pump beam must also be focussed on the switch with a lens. They can only be brought a certain distance apart without the objective clipping the pump beam or the lens clipping the probe beam. The major benefit of using a photoconductive switch comes in temporal resolution. The switch responds very quickly to its illumination and, effectively, no temporal resolution is lost in this conversion, so the ultimate limit in temporal resolution remains the width of the incident laser pulses. When the sample is triggered by a photovoltaic cell, the temporal resolution is limited by the reaction time of the cell. The photovoltaic cell can be thought of as a pre-packaged photoconductive switch, thus making it more user-friendly.

4.2 Experimental Results with Photoconductive Switch

The first ferromagnetic resonance investigations were done to determine material constants to be used in micromagnetic simulation. These results are reported in detail in Hiebert et al [52,73] and are merely summarized here. By measuring the dependence of the resonant frequency with DC field and fitting it to the Kittel formula

$$f = \frac{\gamma}{2\pi}\sqrt{H(H + 4\pi M_s)} \tag{4.1}$$

where γ is the gyromagnetic ratio, H is the external DC magnetic field and M_s is saturation magnetization of the permalloy, a value for the saturation magnetization was measured. It was found to have a value of $4\pi M_s$=10.8kOe. Then the time resolved ferromagnetic resonance curve were fitted with that value of saturation magnetization to find the damping constant. It was found that α=0.008 was the best fit value for the curves. Spatial snapshots of the magnetization were taken at various increments in time, in various DC magnetic fields. The most complex case was that of a circular permalloy element 8 μm with a thickness of 100 nm. It is in a 250 Oe external magnetic field and given a transient magnetic field with a large reflection in it. This reflection makes for a more complex interaction, leading to more complex spatial magnetization profiles. Only three spatial images were taken. They are shown in Fig 4.2. All three images are after the double excitation peak. The excitation is mostly symmetric from left to right but is clearly spatially non-uniform.

4.3 Simulation of these results

Because the system in 4.2 is a relatively simple system with high spatial non-uniformity, it is a good place to begin with real world tests of the simulation. It should be noted that the sample is relatively large and in order to have comparison results in a reasonable amount of time, we are forced to use a two dimensional simulation and cells that are larger than the exchange length of permalloy. Whether or not these lead to

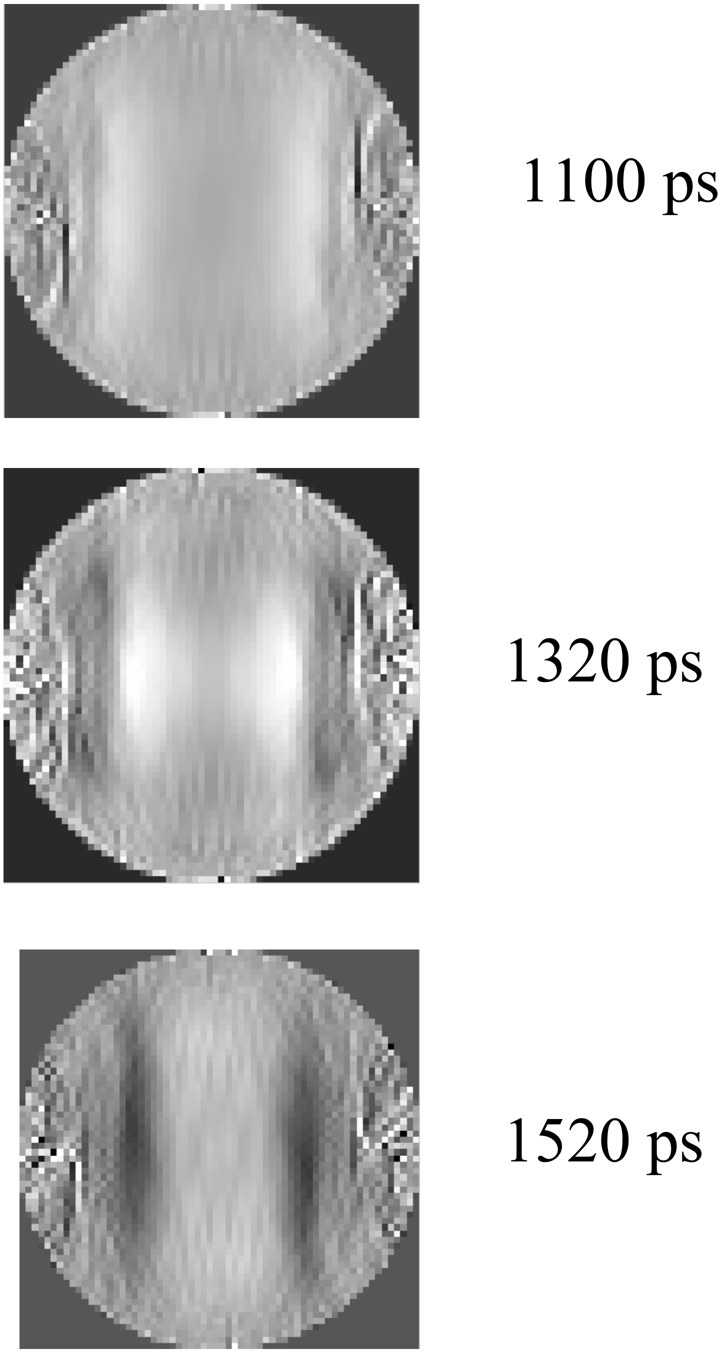

Figure 4.2 Spatial structure in an 8 micron circle after a "double kick" ferromagnetic resonance excitation. Notice spatial richness of excitation. Top left shows an SEM micrograph of the sample, top right a cartoon of spatial and temporal transient magnetic field.

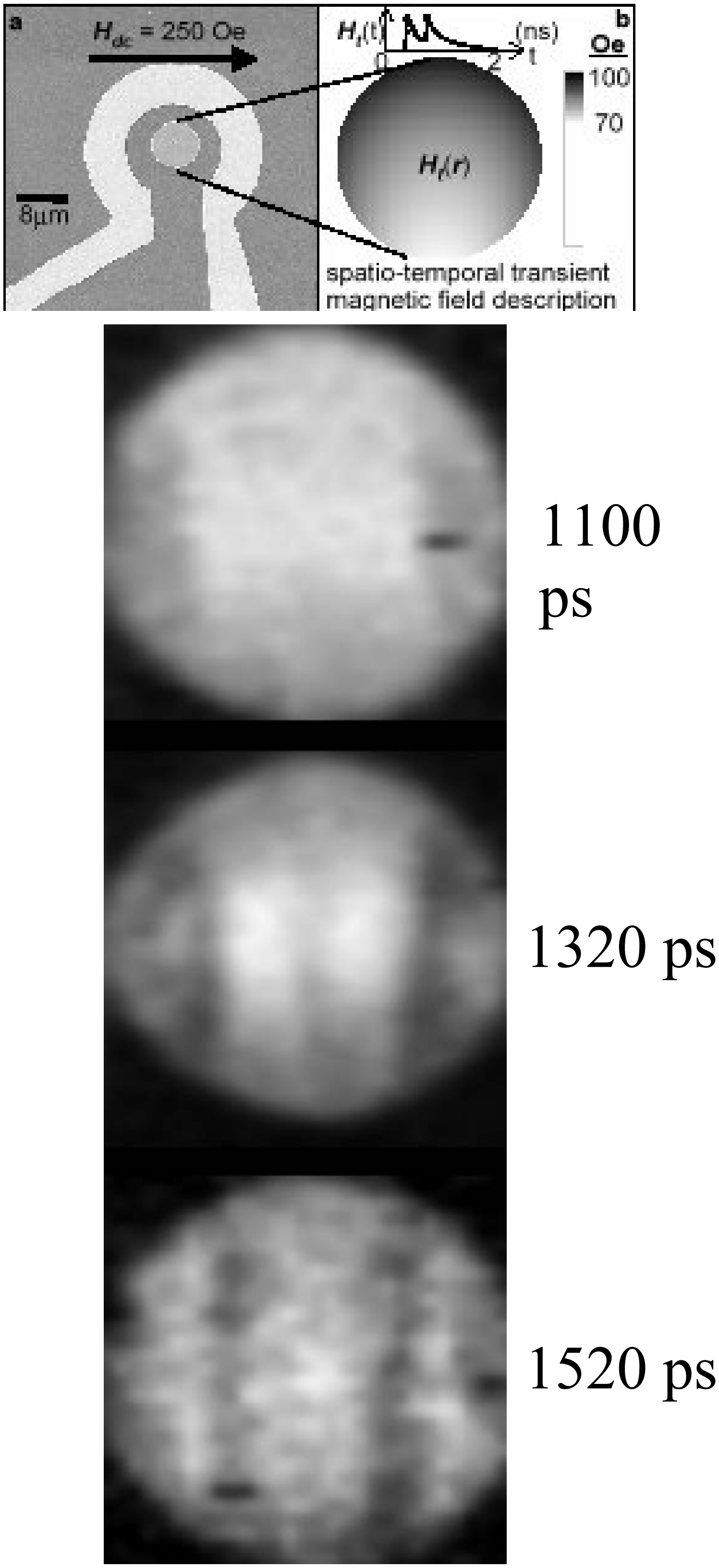

Figure 4.3 Simulation of 8 micron ferromagnetic resonance with double kick excitation. 256 x 256 cells. Agreement appears to be very good.

problems are issues that can be further addressed, partially by how well the simulation agrees with experiment.

Initial simulations were done with 256 x 256 cells. This makes for a cell size of 31 x 31 x 100 nm. This is large with respect to the exchange length. However, at first glance it appears to give reasonable results. The simulation results for this initial comparison are shown in Fig. 4.3.

The experimental spatial resolution is limited to about 700 nm, so features in the simulation will be washed out in experiment, but they are in very good agreement. Maxima and minima appear in the same places.

With this positive result we went to smaller cells. We found that in order to reproduce these good comparisons it was necessary to have a spatially varying magnetic field as well as one that is temporally varying. In order to do this, one must accurately know the pulse profile in both space and time. The fact that a good agreement is possible with larger cells, but without the spatial variation in the transient magnetic field is an interesting result. This may be partially because the dynamics is mostly driven by magnetostatics and exchange energy is only a small correction. This correction becomes

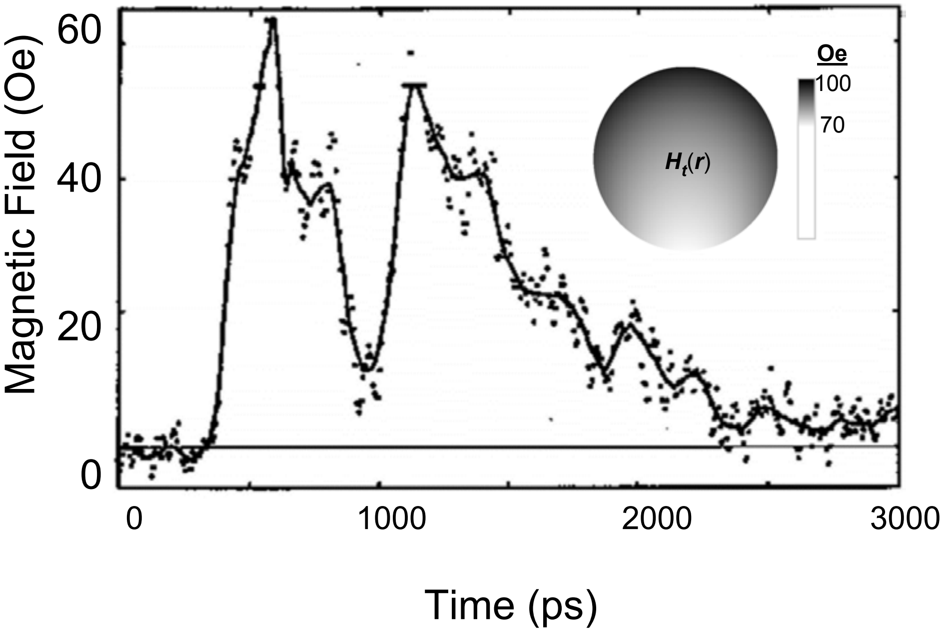

Figure 4. 4 Detailed representation of the spatial and temporal representation of the "double kick" ferromagnetic resonance exicitation. Temporal profile found magneto-optically. Spatial profile found with Biot-Savart law. The circles shows spatial variation is the field within the 8 micron disk.

less significant with large cells, so less effort must be taken to ensure it is correct. Thus, one can succeed with simulation with an average transient magnetic field (which is assumed to be uniform throughout the sample) instead of the actual spatially varying one.

The pulse's profile in time can be found magneto-optically [75,76]. At high enough DC magnetic fields, the magnetization response to the transient field mimics the transient field. This response can be filtered to remove any small remaining resonance oscillations, leaving a transient field **H(t)** that is accurate up to the cutoff frequency of the filter. This field is spatially non-uniform because it is caused by a coil which is only a partial loop and because the sample diameter is not small compared to the diameter of the coil. Using the Biot-Savart law, an effective field as a function of position is calculated. A rough sketch of the temporal profile of the pulse is shown in Fig 4.2. A more accurate representation is in Fig.4.4.

With these tools in place, it is possible to calculate the FMR images with smaller cells (512 x 512 cells) as is shown in Fig.4.5. There was still concern that these cells may be too large and this simulation was repeated with 1024 x 1024 cells. The results of the largest simulation (1024x1024 cells) are shown in Fig. 4.6. These results show that the simulation converges to a pretty similar answer with both of the largest two cell sizes.

In theory, we could run the simulation with arbitrarily small cells to guarantee that we have not lost features due to large cell size, but there is a trade off in the amount of time it takes to run the program. Since the simulation scaling is dictated largely by the FFT which scales as N log N where the log is to the base 2. Since the FFT has its best performance when the number of cells in each direction is 2^n for some integer n, it is most feasible to increase the number of cells in the x and y direction both by a factor of two in order to try smaller cells. Assuming the simulation program scales exactly as N log N (where the log is to the base 2), this will increase processing time by a factor of 8. Thus it can become prohibitively difficult to run a simulation with too many cells. One solution to this is to try parallel computation. We have only found this moderately successful. With four CPUs an increase in speed by a factor of roughly two (vs. one CPU) occurs and adding more CPUs adds little (and depending on the problem can slow it down). The 256 x 256 run takes about 10 hours to complete, the 512 x 512 run about 3 days and the 1024 x 1024 run takes about 26 days. Thus, this largest run is too large to

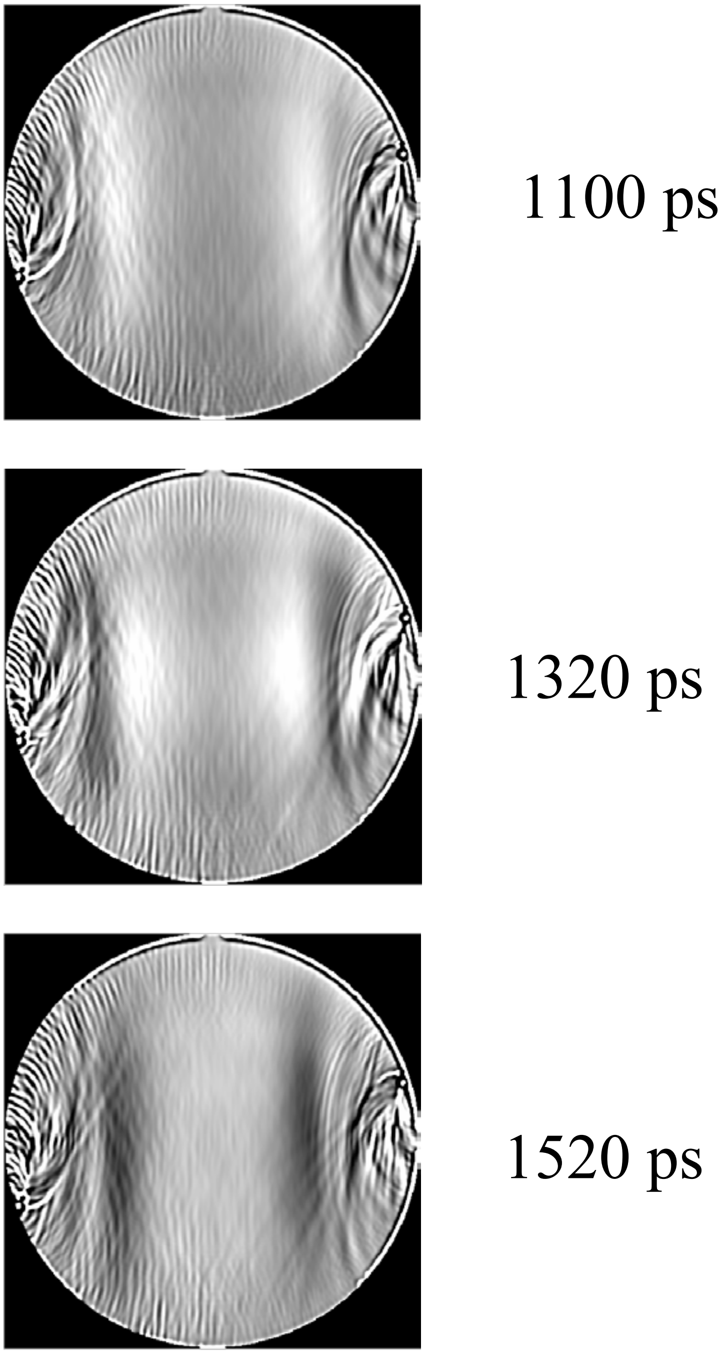

Figure 4.5 FMR in an 8 micron disk with a “double kick” excitation. 512 x 512 cells. In order to keep good agreement with experiment, Biot-Savart law is required to calculate a spatially varying magnetic field.

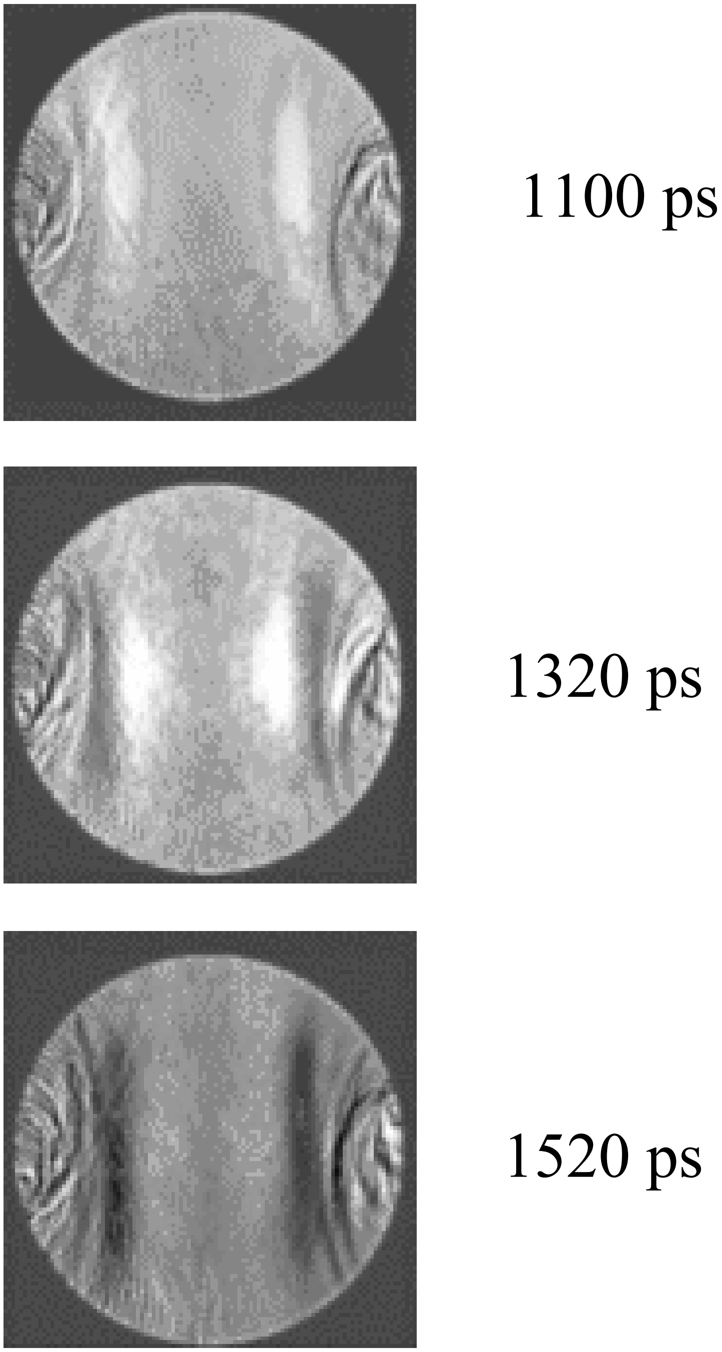

Figure 4.6 FMR in an 8 micron disk with a “double kick” excitation. 1024 x 1024 cells. In order to keep good agreement with experiment, Biot-Savart law is required to calculate a spatially varying magnetic field. Notice how similar it appears to the simulation with 512 x 512 cells.

routinely execute, however it is valuable to see that results between it and the smaller 512 x 512 run are very similar.

4.4 Experimental Results with fast photodiode

Further experimental data was gathered using the setup where the sample was pumped using a fast photodiode. The samples used were 4 μm squares with and without a patterned defect at the center of the square. They are shown in Fig. 4.7. Montages of

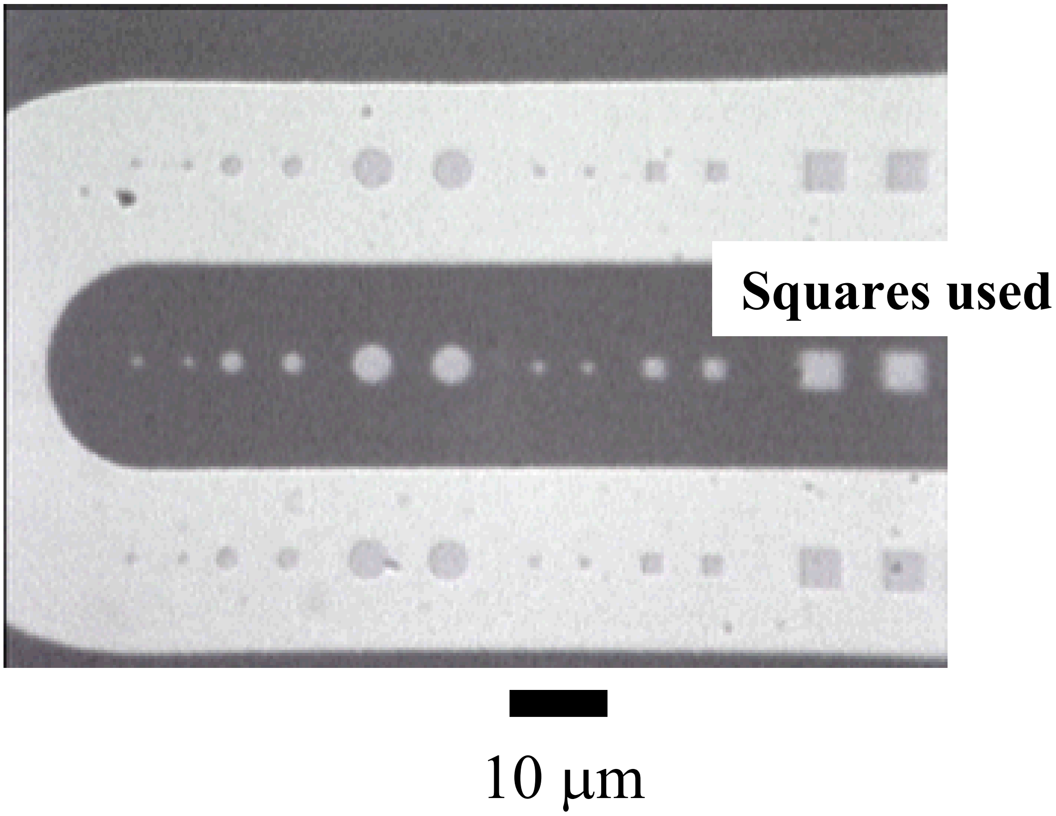

Figure 4.7 Optical microscope photo of sample used in photodiode FMR experiments. The gold coil is 20 microns wide with a 20 micron opening. The 4 micron squares used are inside the coil on the right**.** The ~ 150 micron pinhole in the center of the rightmost one cannot be resolved.

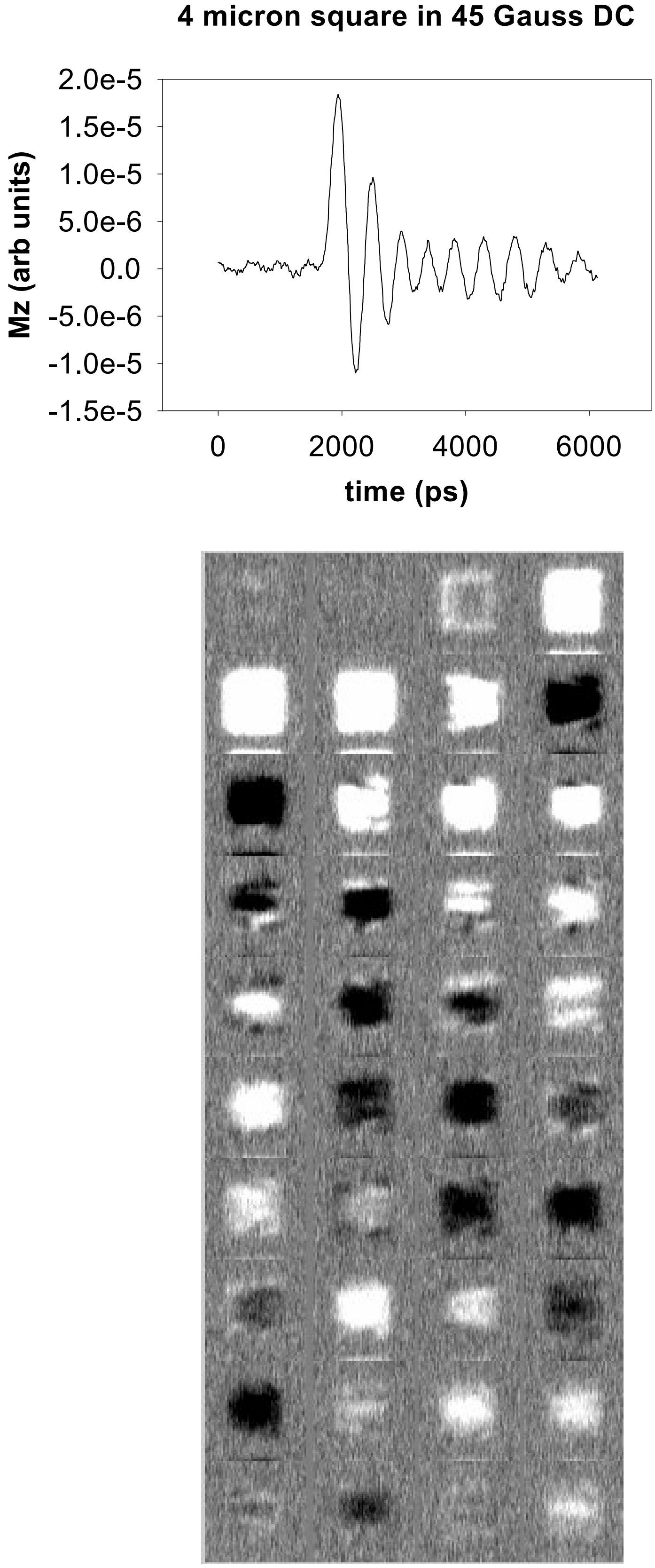

Figure 4.8 FMR in a 4 micron square in a 45 Gauss DC field. Time scan at the center of the sample and spatial scans. First spatial scan frame is taken at t=1900ps. Each additional frame 120 ps later reading across rows from left to right

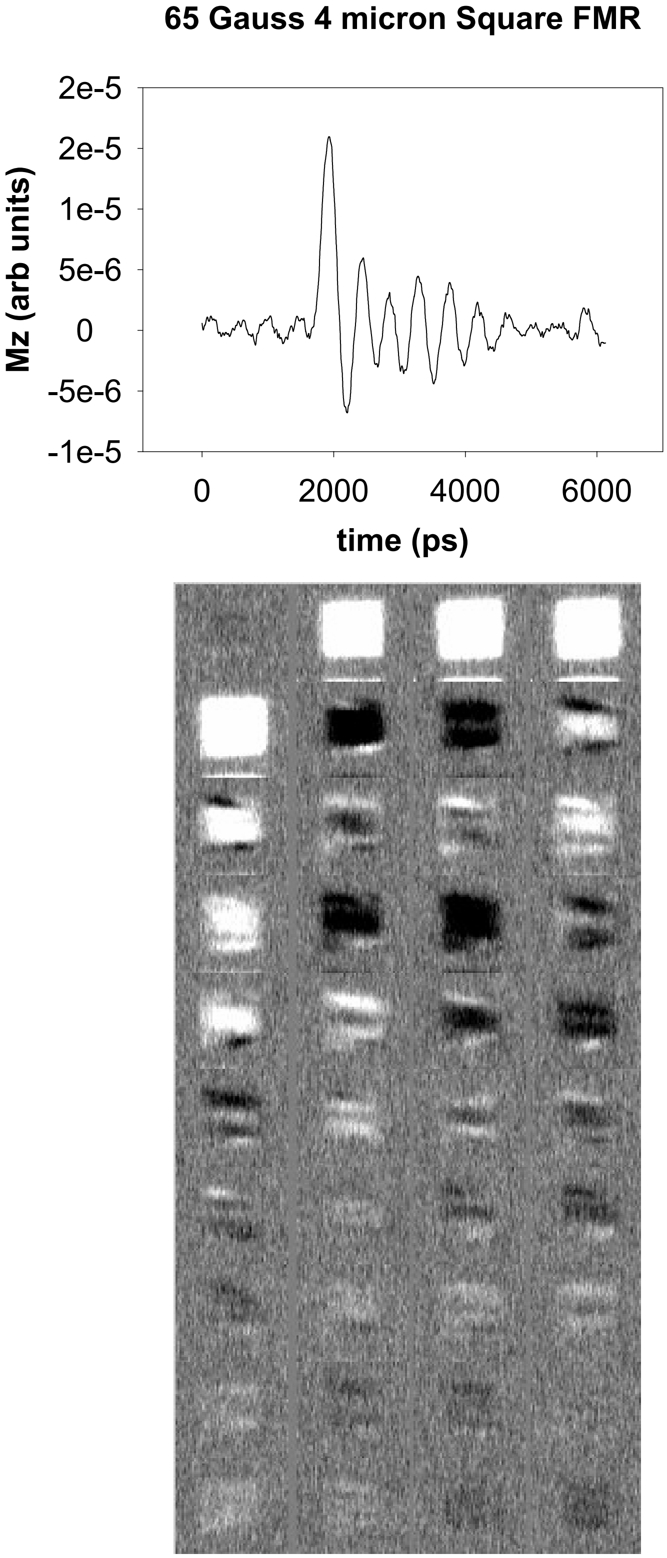

Figure 4.9 FMR in a 4 micron square in a 65 Gauss DC field. Time scan at the center of the sample and spatial scans. First spatial scan frame is taken at t=1900ps. Each additional frame 120 ps later reading across rows from left to right

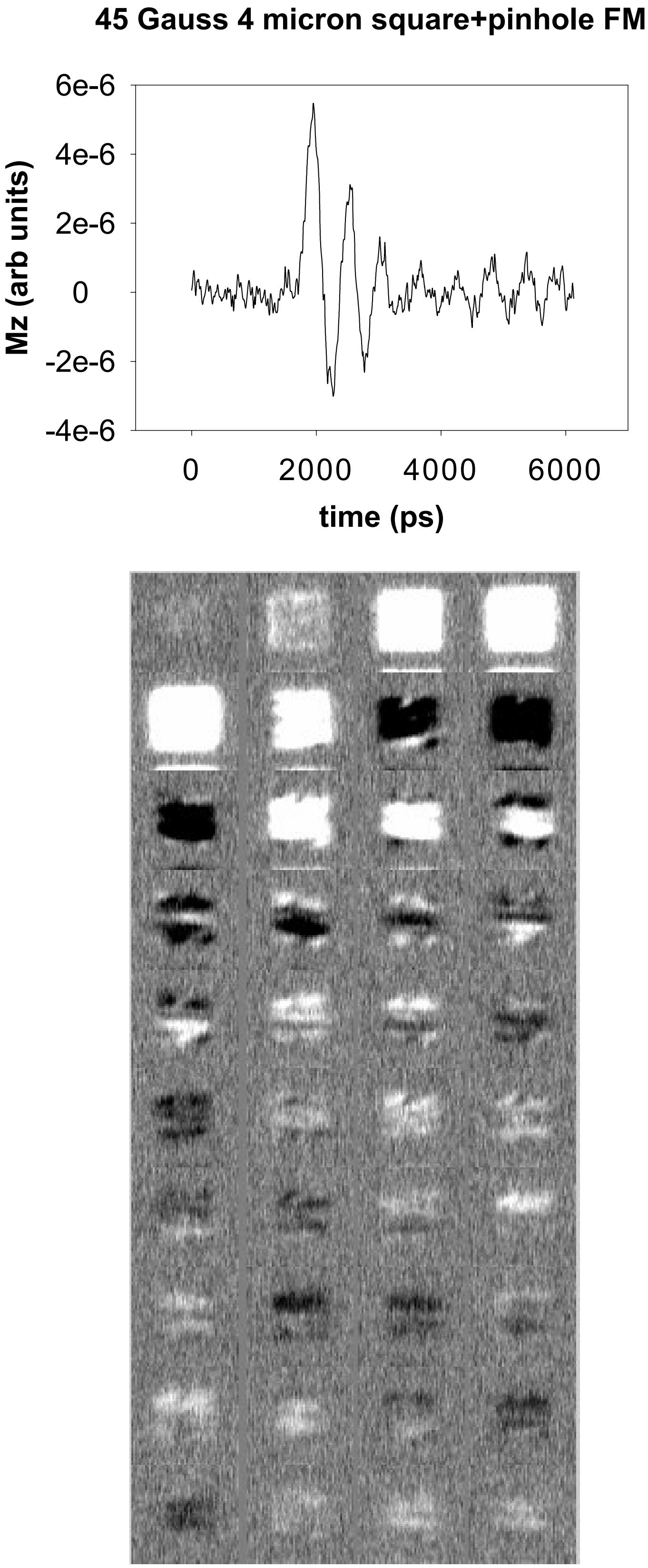

Figure 4.10 FMR in a 4 micron square with a pinhole in its center in a 45 Gauss DC field. Time scan at the center of the sample and spatial scans. First spatial scan frame is taken at t=1900ps. Each additional frame 120 ps later.

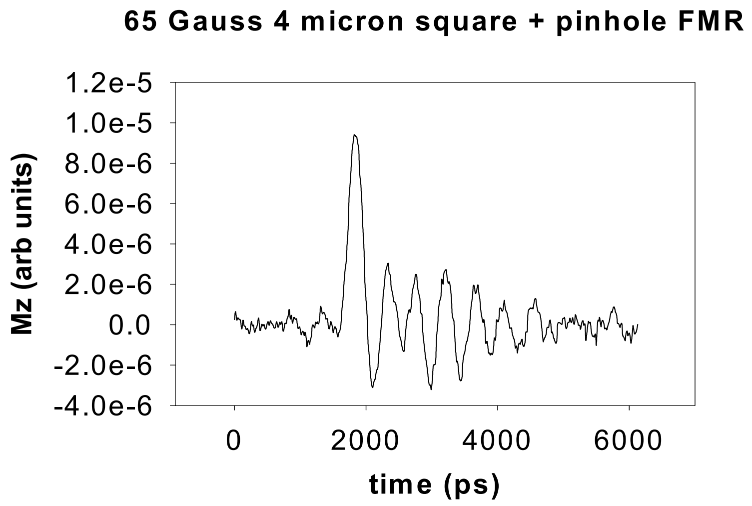

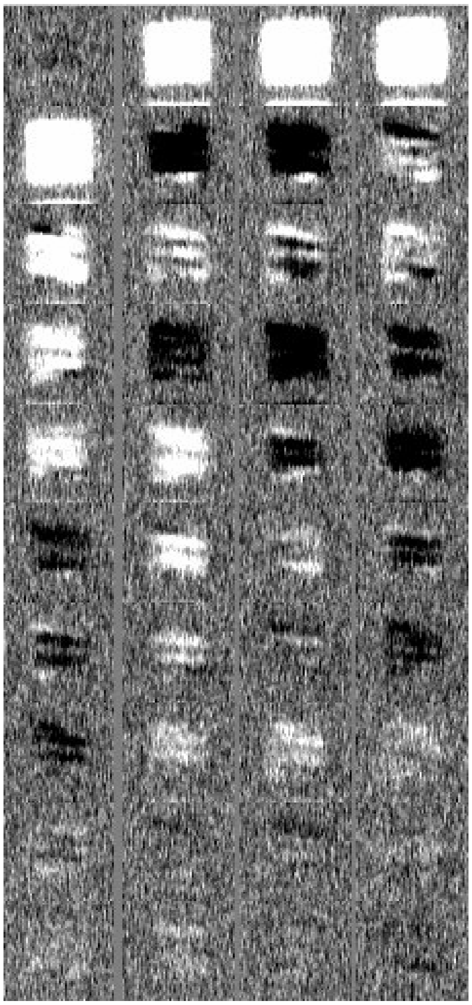

Figure 4.11 FMR in a 4 micron square with a pinhole in its center in a 65 Gauss DC field. Time scan at the center of the sample and spatial scans. First spatial scan frame is taken at t=1900ps. Each additional frame 120 ps later.

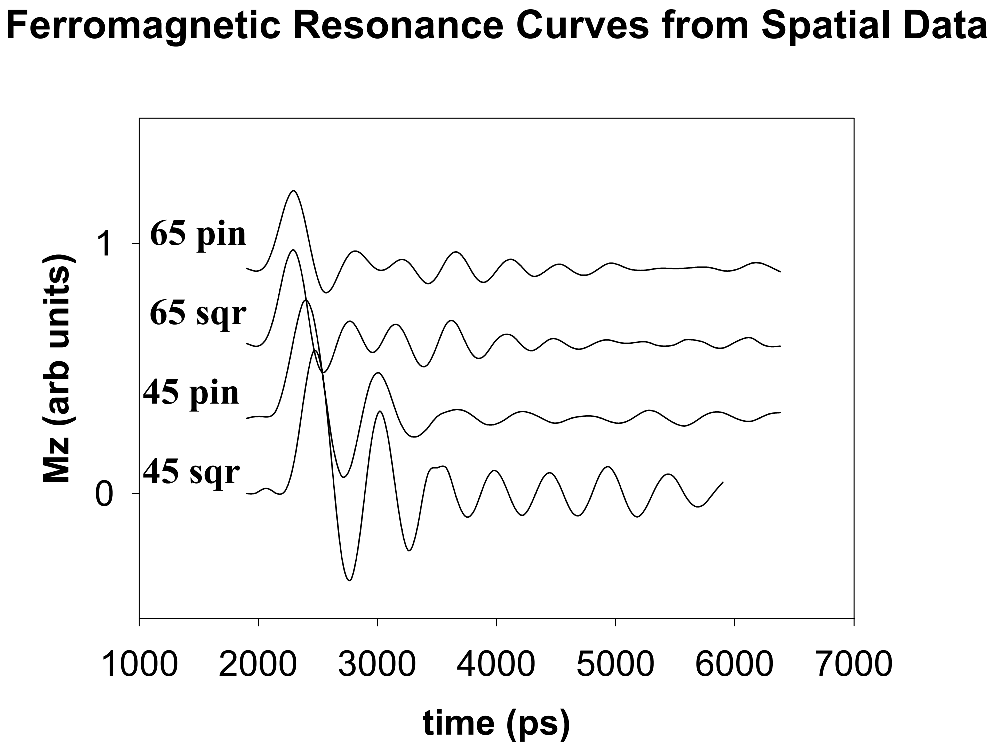

Figure 4.12 Ferromagnetic resonance curves reconstructed from spatial data. This shows spatial data can reproduce time scans.

.the experimental data are shown in figures 4.8 and 4.9 for the square without a defect. 4.8 is in 45 Gauss DC and 4.9 in 65 Gauss DC. The same data for a square with a pinhole in its center is in figures 4.10 (45 Gauss) and 4.11 (65 Gauss). All of these figures show the square in the center of the region oscillating in damped resonance. In general, the sample without a pinhole shows "cleaner" oscillations. The spatial traces are also more uniform for the sample without a pinhole. As a first check of the data, one can use the spatially resolved profiles to generate time curves to see if they agree with one another. Pseudo-time traces generated by averaging the central 700 nm region in the spatial traces are shown in Fig. 4.12. These show that this data is internally consistent. Times are relative to the start of the delay line, and due to realignments of optics etc. time zero moves slightly between some of the runs.

The pinhole in the center of one of the squares can be viewed as a scattering center which will serve to disrupt the coherent damped oscillation in the sample. Thus we should see additional structure in the center of the sample, made up mostly of high frequency spin waves. This structure will be mostly too small for our spatial resolution. It appears as a "stripe" around the middle of the sample (where the pinhole is). We are able to detect the presence of a pinhole which is far below the resolution limit of our microscope system.

Simulating this is a test of our micromagnetic simulation program. We have significantly more data in this run to match, and all material parameters keep the same values as before.

4.5 Simulation of this data

Micromagnetic simulation is done of 4 μm squares with a 15 nm thickness. The sample is broken up into 512 x 512 cells (thus cells are ~7.8 nm a side). This data is shown in Fig. 4.13 & 4.14 for the DC fields of 45 and 65 Gauss respectively.

For the most part, the square samples oscillate coherently for the first couple of oscillations. This breaks up with time. Stripes from the top and bottom ends of the sample start to appear and travel toward the sample center. These break up the coherent oscillation. They leave behind them some high frequency oscillations that would be hard to spatially resolve in experiment. The stripes that appear in simulation match well features seem in experiment.

Getting good agreement in simulation with a patterned defect in the sample center will be quite difficult. The defect's exact size and shape will have a strong influence on scattering in its proximity, and thus dynamic properties as a whole. Meaningful comparisons have not been run. With a small round defect feature, the limitations of square pixels are exposed. The central (defect) region of the sample will be pixelated in a staircase manner which will produce further artificial high frequency features from the pixelation. In order to fix this problem, the demagnetizing calculation will have to be reformulated using circular cells. This will remove periodicity of the cells and prevent FFT's from being used to speed up the demagnetizing calculation, so it is a significant task. In preliminary attempts to simulate this problem, this high frequency artifact from

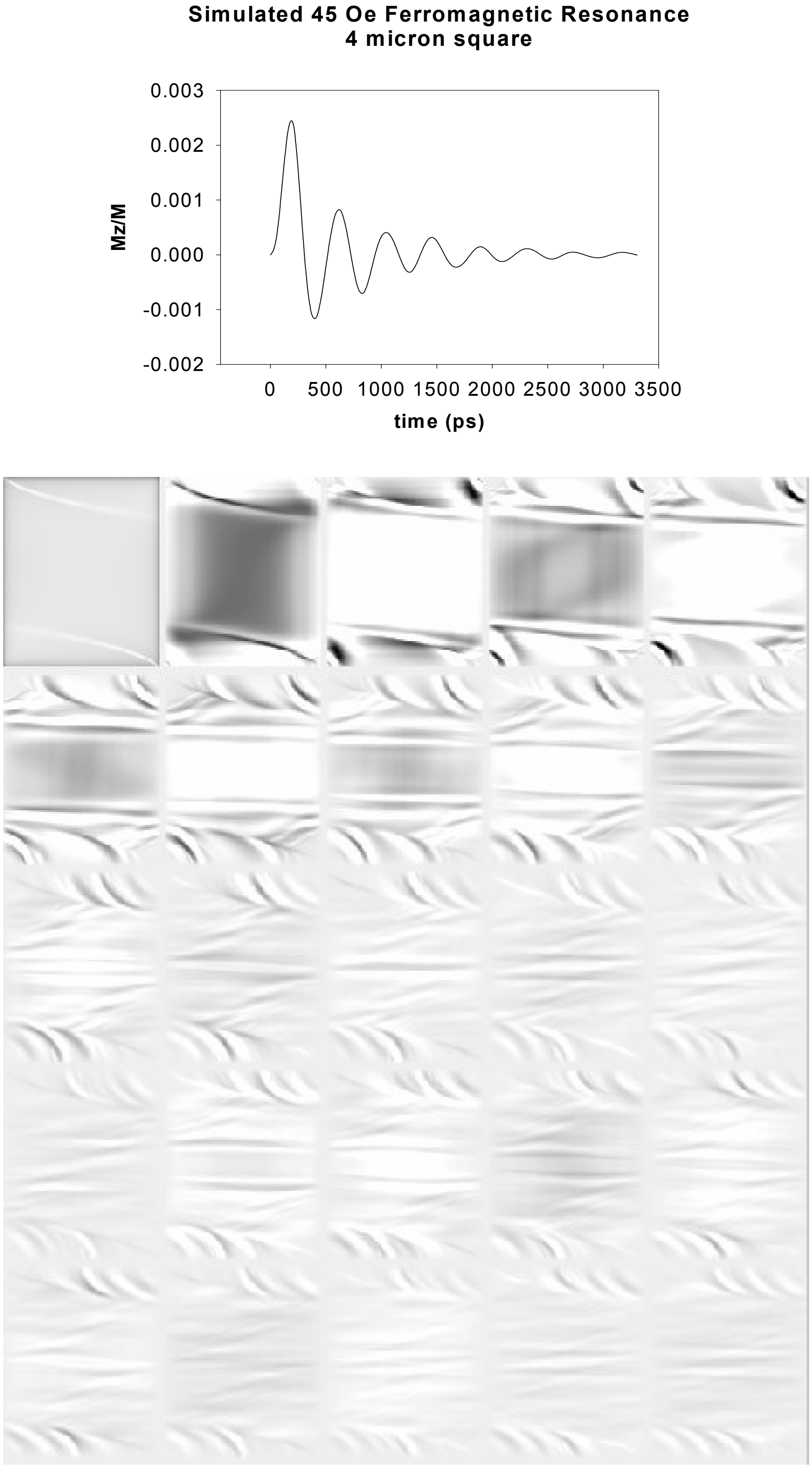

Figure 4.13 Simulated FMR in a 4 micron square in a 45 Gauss DC field. Time scan at the center of the sample and spatial scans. First out of plane spatial scan frame is taken at t=33 ps. Each additional frame 120 ps later. Initial state (t=0 s) subtracted from all frames

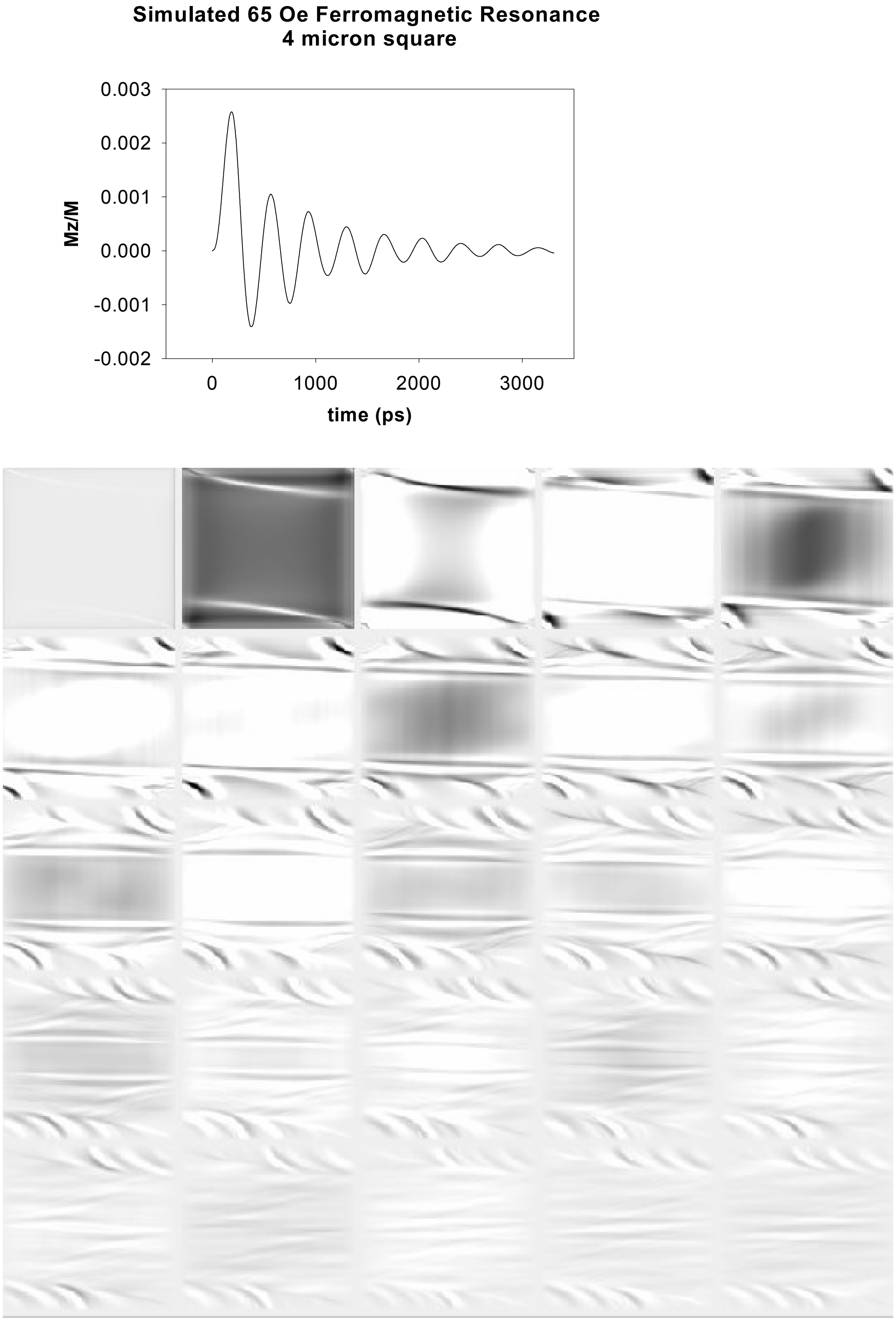
Simulated 65 Oe Ferromagnetic Resonance
4 micron square

Figure 4.14 Simulated FMR in a 4 micron square in a 65 Gauss DC field. Time scan at the center of the sample and spatial scans. First out of plane spatial scan frame is taken at t=33 ps. Each additional frame 120 ps later. Initial state (t=0 s) subtracted from all frames defect pixelation is far to significant to lead to any results which yield any confidence. More work is required to accurately model small defects of arbitrary shape. It is far too dependent upon exact pixalation of the defect to be taken seriously. The effect of a defect can be quite significant (see section 5.7) for this problem addressed in a magnetization reversal situation- however this defect is several pixels large so pixelation becomes a larger issue.

Comparing ferromagnetic resonance time scans is quite complex. The frequency and envelope of the oscillations can vary with position in a sample. This requires the ability to know the sample position with sub micrometer accuracy to ensure that a comparison is valid. This is shown in Fig. 4.17 where a ferromagnetic resonance oscillation curve is plotted from the simulation for several different positions within the sample. The 4 micron square in 65 Oe DC is chosen as an example. Three different regions are chosen to construct FMR curves. Each region is circular with a 700 nm diameter (to simulate a laser spot). The regions are in the sample centre, displaced along

.

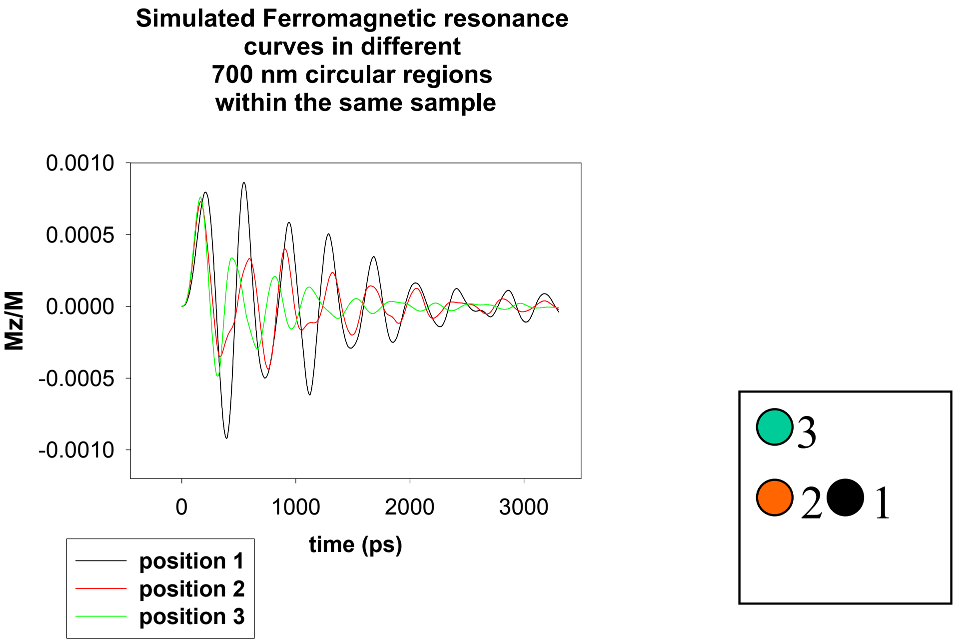

Figure 4.15 Simulated ferromagnetic resonance curves at different points withing a 4 micron square in 65 Oe DC field. Each curve averages a 700 nm circular region. The frequency and shape of the curve is dependent upon position within the sample

one axis only from the sample centre and displaced along both axes from the sample centre. They each lead to very different FMR curves. Thus, only the spatial comparison offered is going to be valid, without strong control on position within the sample.

4.6 Summary of this chapter

In this chapter, the ferromagnetic resonance problem is introduced. Experimental details for carrying out these investigations are presented. Experimental results and simulation with both a photoconductive switch and a photovoltaic diode are presented. The agreement between simulation and experiment shows that the problem is well understood. Care must be taken to properly model small defects of arbitrary shape. This is still an open problem. It also leads to new insight, such as how the FMR time curves are strongly position dependent within the same sample. This chapter shows that the simulation does a good job of capturing dynamics in a low amplitude excitation.

5. Magnetization Reversal

Our lab has done a significant amount of pioneering work in spatially resolved magnetization reversal experiments using time-resolved scanning Kerr effect microscopy (TR-SKEM). This work has been published in many places.[52] This chapter discusses specific experiments and attempts to simulate the results. It concludes with further simulations into the effect of various magnetic field configurations, risetimes and defects in the sample as explorations of how to modify and control the magnetization reversal and exploration of how rich magnetization dynamics can be.

5.1 Experimental Details

The method of time resolved scanning Kerr effect microscopy (TR-SKEM) is discussed in chapter 2. In order to do in-plane magnetization reversal experiments, a sample geometry is needed in which a transient magnetic field will be produced that will

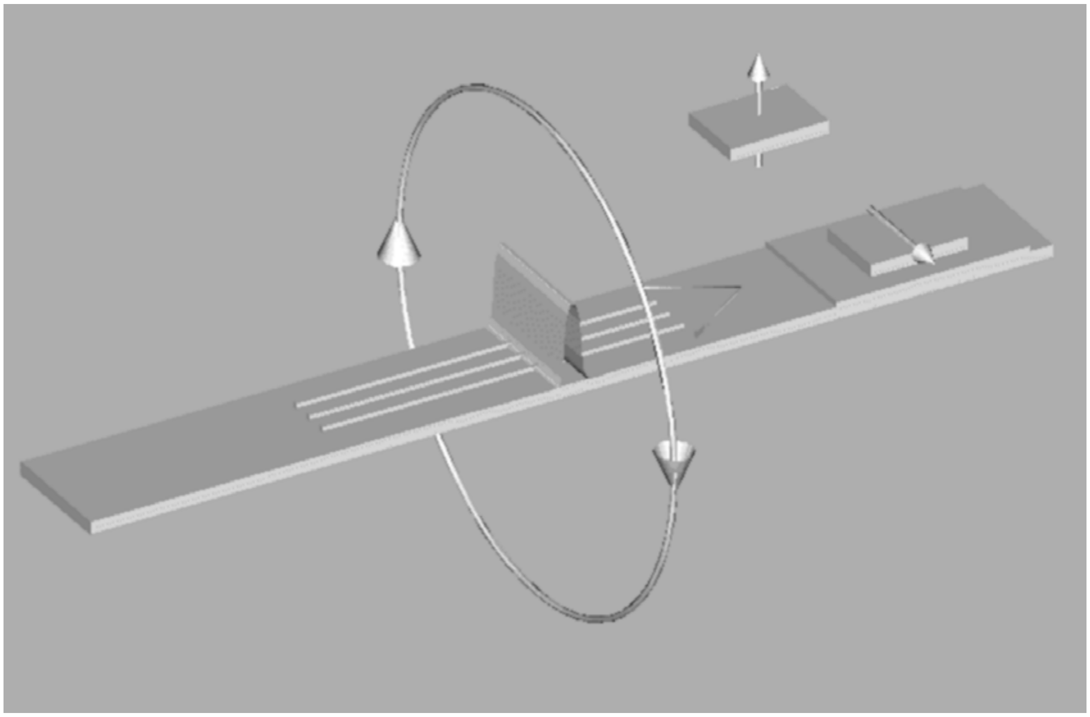

Figure 5.1 Schematic of current (and associated induced magnetic field) through a stripline. Magnetic samples are placed on or near the stripline to be influenced by the associated magnetic field.

be parallel to the sample. This can easily be done, by placing a sample on top of a stripline through which current will be passed. This is shown schematically in Fig. 5.1. In practice, often a spacer layer of SiO_2 is placed in between the stripline and the permalloy magnet. This is to prevent current in the stripline from also passing through the magnet itself and leading to a more complicated magnetic field geometry. Choi's [52,70] results do not use this spacer layer. This is a minor correction. Using Ohm's Law, one can see this

$$\mathbf{J} = \sigma\mathbf{E} \tag{5.1}$$

We assume that the electric field **E** is the same everywhere, which is true when we neglect finite size effects in the conductor and the magnet. Since magnetic fields depend on currents and not current densities we will re-write this as

$$\mathbf{I} = \sigma\mathbf{E}wt \tag{5.2}$$

where w is the width of the layer and t is its thickness. Typical numbers from our samples with gold striplines and permalloy magnets t_{gold}=300 nm $t_{permalloy}$=15 nm w_{gold}=20 μm and $w_{permalloy}$=10 μm. Using σ_{gold} ~ 450 1/mohm•cm [77] and $\sigma_{permalloy}$ ~ 20 1/μohm•cm we find a ratio of 900 thousand(!) between the current flowing in the stripline to the current flowing in the magnet. Thus any correction to the total magnetic field allowing current to flow in the magnet is very small.

With sample pumping understood, repeatably resetting the sample to its intial state after a pump pulse must also be addressed. This is done with a permanent magnet which has a field large enough to return the permalloy magnet back to its initial magnetization state, yet smaller than the magnetic field produced by the pulser that is flowing through the stripline. This geometry is shown in figure 5.2.

In this chapter, first the example of a 10 x 4 μm element (actual size after outsourced optical litho; nominally this element was designed to be 10 x 2 microns and is referred to as a "10x2" sample) that has imperfect lithography leading it to be oval in shape is discussed. The case of a 100 Oe DC bias field with a 160 Oe transient reversal pulse is first studied. Then the cases of different bias fields are systematically studied, followed by different sample shapes. All of these will have comparisons between simulation and experiment. In order to begin this comparison, the TR-SKEM result on this sample is presented. In figure 5.3 we show a time traces of M_x, M_y and M_z versus time for this

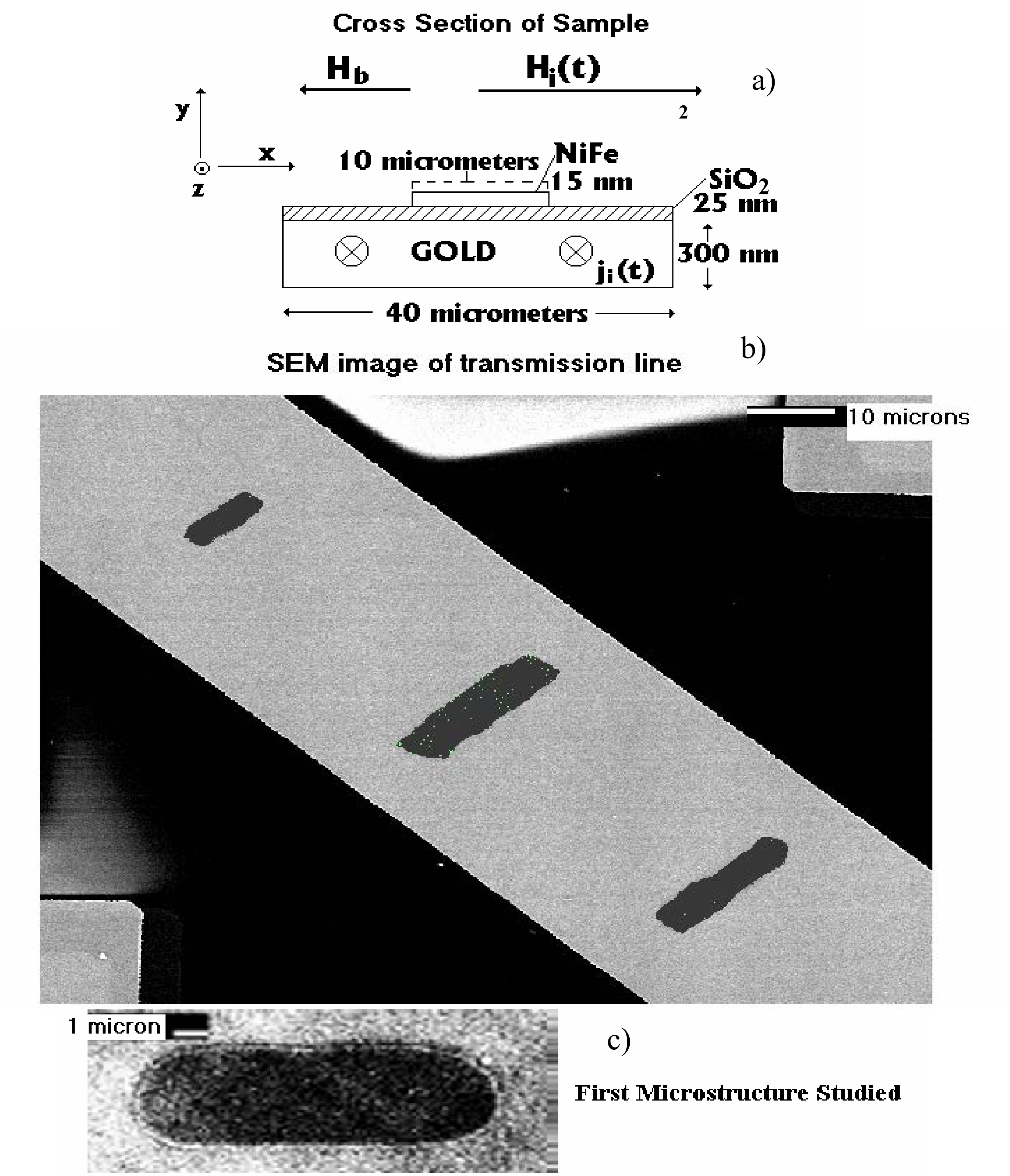

Figure 5.2 **a)** Cross-section of microstructure studied. Permalloy sample is on a gold line with SiO_2 spacer layer in between. **b)** SEM micrograph of samples on a stripline. **c)** Blowup of “10x2” sample which we first studied.

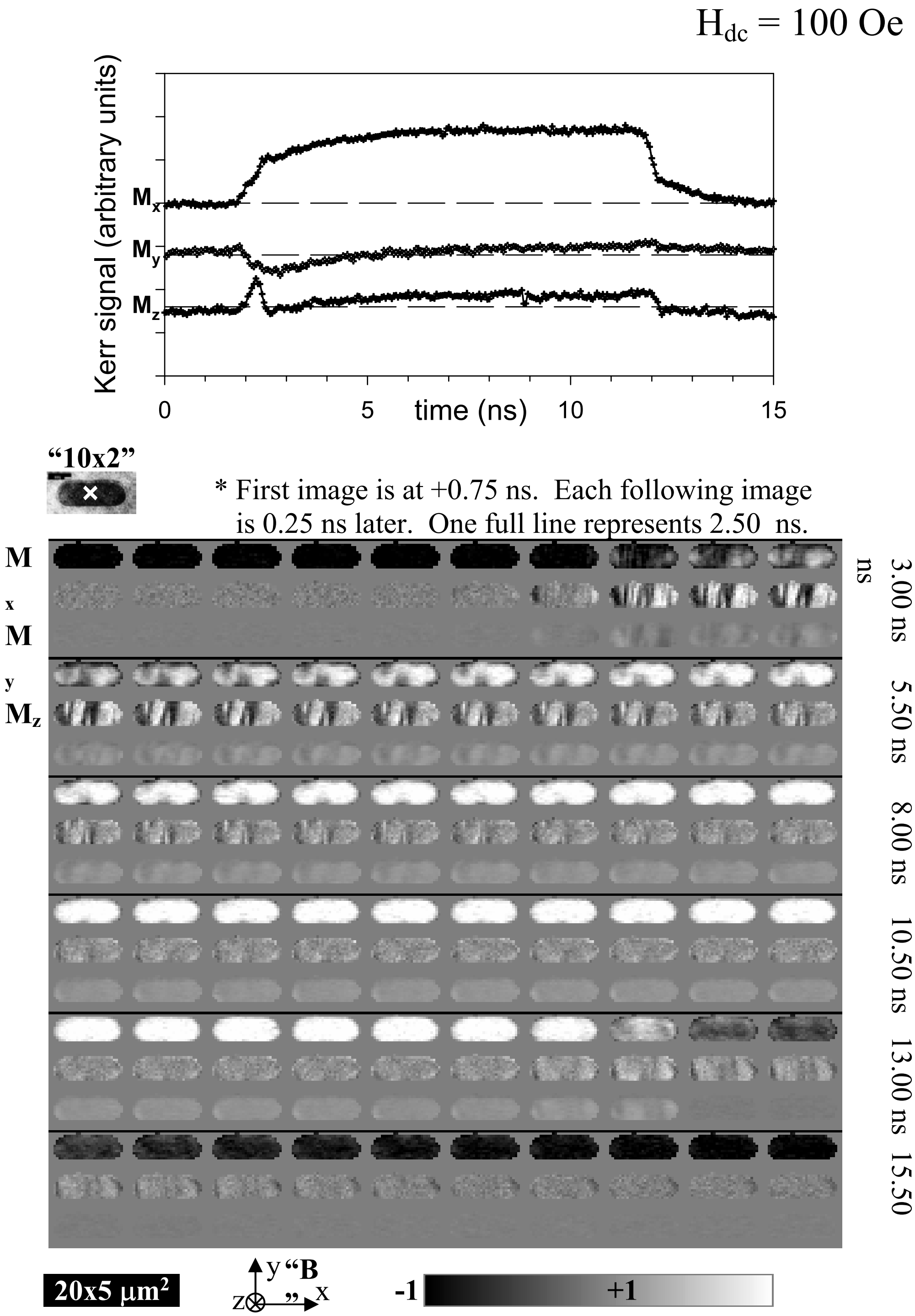

Figure 5.3 Spot trace and montage data for the "10x2" sample in a 100 Oe field. There is 250 ps spacing between frames. The front reversal starts on the left and right edges and proceeds in a stripelike pattern. The back reversal is more uniform. Front is driven largely by magnetostatics. Back is due to averaging of stochastic thermal fluctuations over a few different metastable reversal states.

sample along with spatial images of all three throughout the reversal process. Because the M_z traces rely on the polar Kerr effect and the M_x and M_y traces rely upon the longitudinal Kerr effect, it is hard to calibrate their relative amplitudes. As can be seen in section 2.3 Kerr effect intensities are quite complicated.

They depend upon angle of incidence and thus the objective used, therefore, ratios of M_z to the other two components are not offered with full confidence. Also due to angular dependence on the strength of Kerr effects, there is some uncertainty assigning absolute magnitudes to any component. Experimentally, one obtains the difference in magnetization between the state at the time in question and a reference state (the magnetization at t=0 on the time axis chosen in Fig. 5.3). Thus, the coloring in the M_x direction is a false color. It is calibrated such that the maximal signal in the sample center is the saturation magnetization of the sample pointing in the direction of the transient field. The initial zero is the magnetization pointing in the direction of the DC field, antiparallel to the transient field. The zero point is merely the halfway point on this colorscale. In the M_y and M_z traces, since there is no reason to assume a component in either direction, the initial zero point is taken to be zero. The fact that the signal does not return exactly to zero when the sample is reversed implies that this assumption may not be fully correct. It is possible that there is some remnant domain structure in the "zero state" of the sample (this question will be addressed further as we look into the simulation of the results in section 5.2), or that there is a small non-zero magnetic field in the y and/or z directions during the experiment to which the sample is responding, thus explaining the non-zero signal in the reversed state.

We see that initially, the reversal occurs at the sample edges and propagates into the center in a stripe-like instability, that is visible in all three magnetization components. The reversal proceeds by pushing to the long edges of the sample. The difference in rise and fall times of the sample is explained by the asymmetry in the magnetic fields involved. Note that the back reversal is different from the front one. The sample "grays" roughly uniformly in the M_x direction and there is significantly less signal in the y or z directions. This is a complex scenario that is likely explained in terms of stochastic switching processes. This is a topic that will be developed further in chapter 6. At any

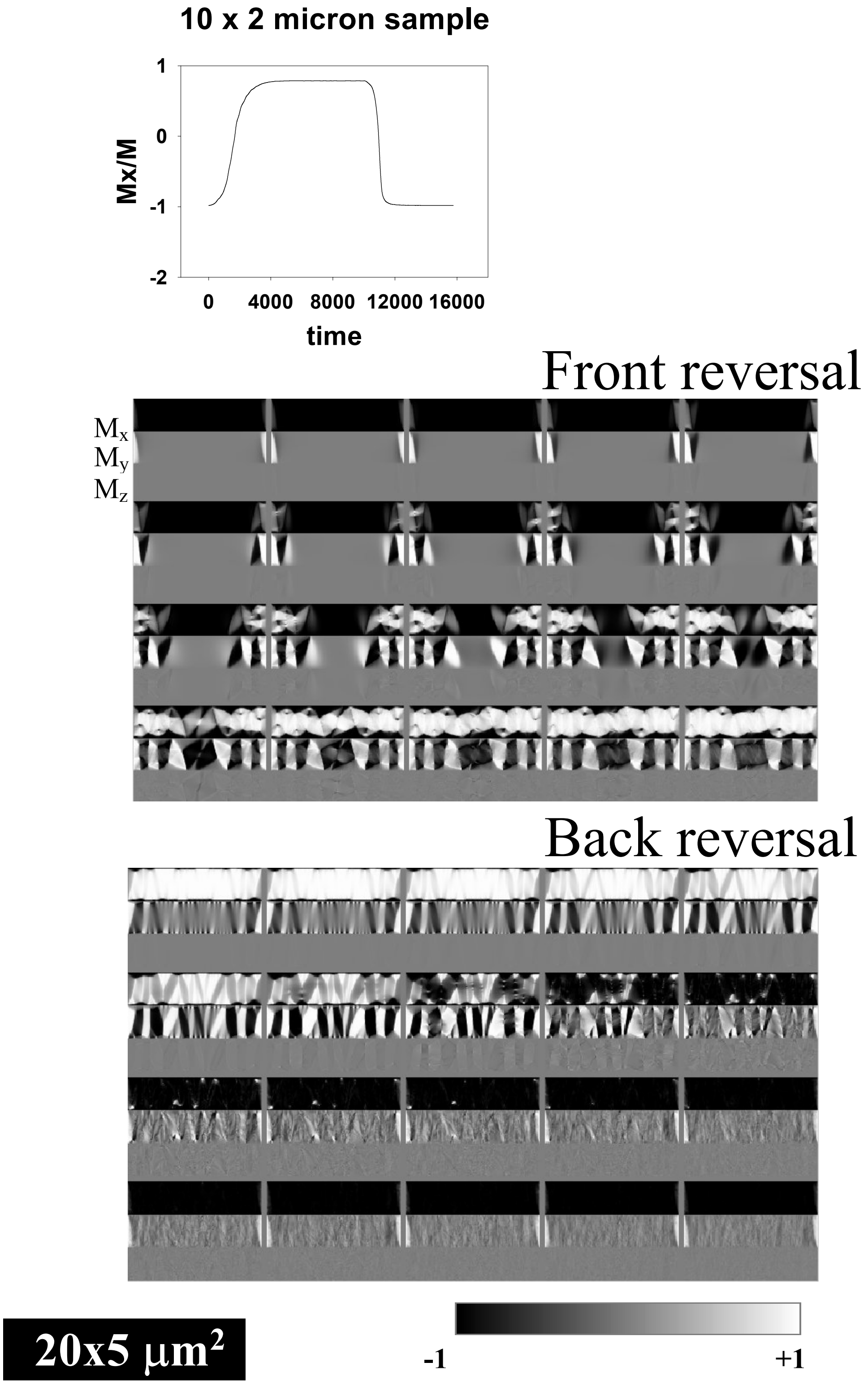

Figure 5.4 Spot trace and montage data for a simulated rectangular 10 x 2 micron sample in a 100 Oe field. There is ~100 ps spacing between frames. The front reversal starts on the left and right edges and proceeds in a stripelike pattern. The back reversal is similar but has a different periodicity of the stripelike structure.

rate, these excitations are clearly large angle excitations. The magnetization direction between adjacent cells may vary by as much as 180°. It is a real test for the same LLG equation with the same parameters to reproduce this motion as in the FMR case.

5.2 Simulation attempts

The first simulation attempt was with a rectangular sample 10 x 2 μm (the orignally intended size). We need an initial magnetization state in which the sample is in at the beginning of the reversal. We can calculate an initial state by starting a sample with all spins pointing along the long axis and allowing it to relax into equilibrium in the 100 Oe DC magnetic field. Then we can switch it with the 160 Oe pulse antiparallel to it. The pulse is based on the parameters measured from the pulser. It has a 10.5 ns full width at half maximum with a 500 ns rise time and a 1 ns fall time included in the 10.5 ns. An M_x vs. time curve is shown for comparison with the experimental one in Fig. 5.4. The sample is broken into 512 x 128 cells leaving a cell size of 19.5 x 15.6 nm. There is some reason to worry about cells being too large to fully capture the dynamics, but due to positive results in the ferromagnetic resonance work (in chapter 4) we will proceed. The spacing between spatial images is ~200 ps and resolution is reduced to 128 x 32 pixels per frame because it is much easier to handle than the full data set produced by the simulation which has sixteen times as many pixels. Initially, the sample is fully magnetized in the x-direction, except for small closure domains at both ends of the long axis. Due to interaction between them, one will be oriented so it is largest on one short end of the sample, and the other will be oriented so it is largest on the other short end of the sample. We add to this the finite size effects of the stripline. There will exist a magnetic field in z coming out of the plane on one side of the sample and into the plane on the other. This gradient in magnetic field can be calculated to be roughly linear with a value of about 4 Oe/μm. This can be calculated using the Mathematica program in Appendix C, which does Biot-Savart law calculations. Due to the gradient, both closure domains have magnetization pointing in the same direction (this is the so called "S-state").

Starting from these closure domains, magnetization begins to propagate toward the sample center in a stripelike pattern that is very reminiscent of the Concertina structure [78]. When the magnetization meets in the middle of the sample, it begins to push toward the sample's long edges, expelling vortices along the way. The 10 ns reversal pulse is not long enough to fully saturate the sample. Its edges remain somewhat unswitched. This produces nucleation sites for the back reversal, which can happen much more quickly over the sample. There is a stripelike instability also observed along the back reversal (especially in the y magnetization), but it is far shorter lived. This comparison is the subject of Ballentine et al.[52] Although there are differences, due in part to a different sample size and shape from the experiment, there are a lot of similarities. Further, the magnetic field gradient serves to reduce symmetry in the sample. It is no longer fully symmetric from left to right. The biggest impact of the gradient is to speed up the reversal slightly. By including magnetic fields in all directions that are produced by the transmission line, we increase the available energy as we increase the Zeeman energy and we provide an out of plane magnetization component which will experience more torque. This leads to an increase in reversal speed. The spatial magnetization patterns are quite similar with and without a gradient, although those without gradient ones are slightly more symmetric from left to right. Hiebert's Ph.D thesis [21] discusses this nearly ideal 10 x 2 μm reversal simulation ("nearly" ideal due to the existence of the magnetic field gradient in the z direction) from a spin wave point of view. Magnetostatic waves exist across the sample and are quite evident in the y magnetization in the spatial frames.

A better agreement is possible using the actual sample shape. The sample shape was measured with a scanning electron microscope. It was masked onto an appropriate pixelated simulation sample and this simulation was again run. The agreement here is better still. It is shown in Fig. 5.5. Because this sample is shaped, and not rectangular, the oval sample is shown within a rectangular area. This forces it to be shown on a smaller scale than the 10 x 2 μm rectangles. This size difference is shown with scale bar in the figure.

The primary difference between the reversal in the shaped sample, when compared to the rectangular one, is that the amount of time required to switch magnetization directions significantly increases in the shaped sample. The stripelike instability is still

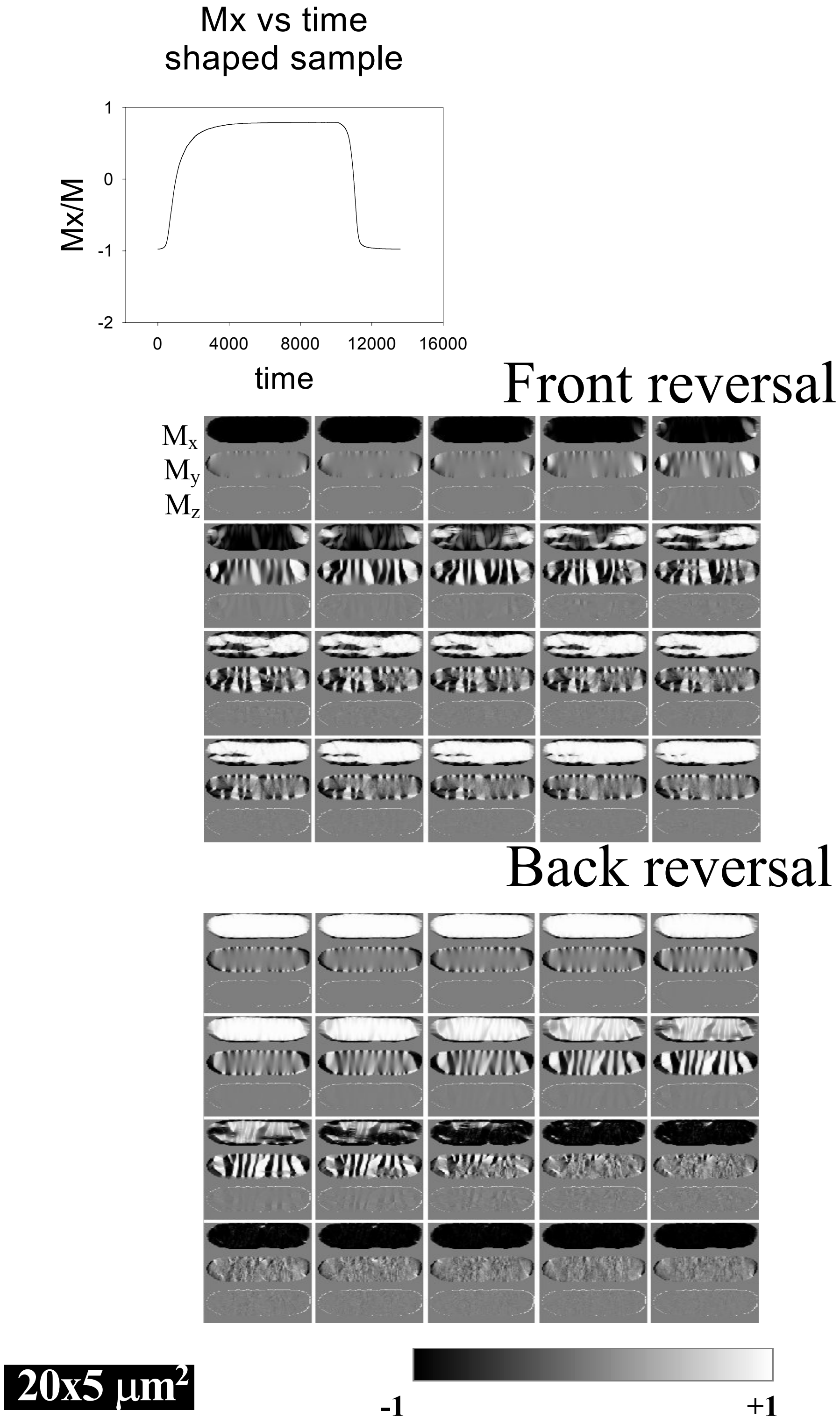

Figure 5.5 Spot trace and montage data for a simulated shaped "10x2" sample in a 100 Oe field. There is ~200 ps spacing between frames. The front reversal starts on the left and right edges and proceeds in a stripelike pattern. The back reversal is similar but has a different arrangement of stripes in the reversal structure.

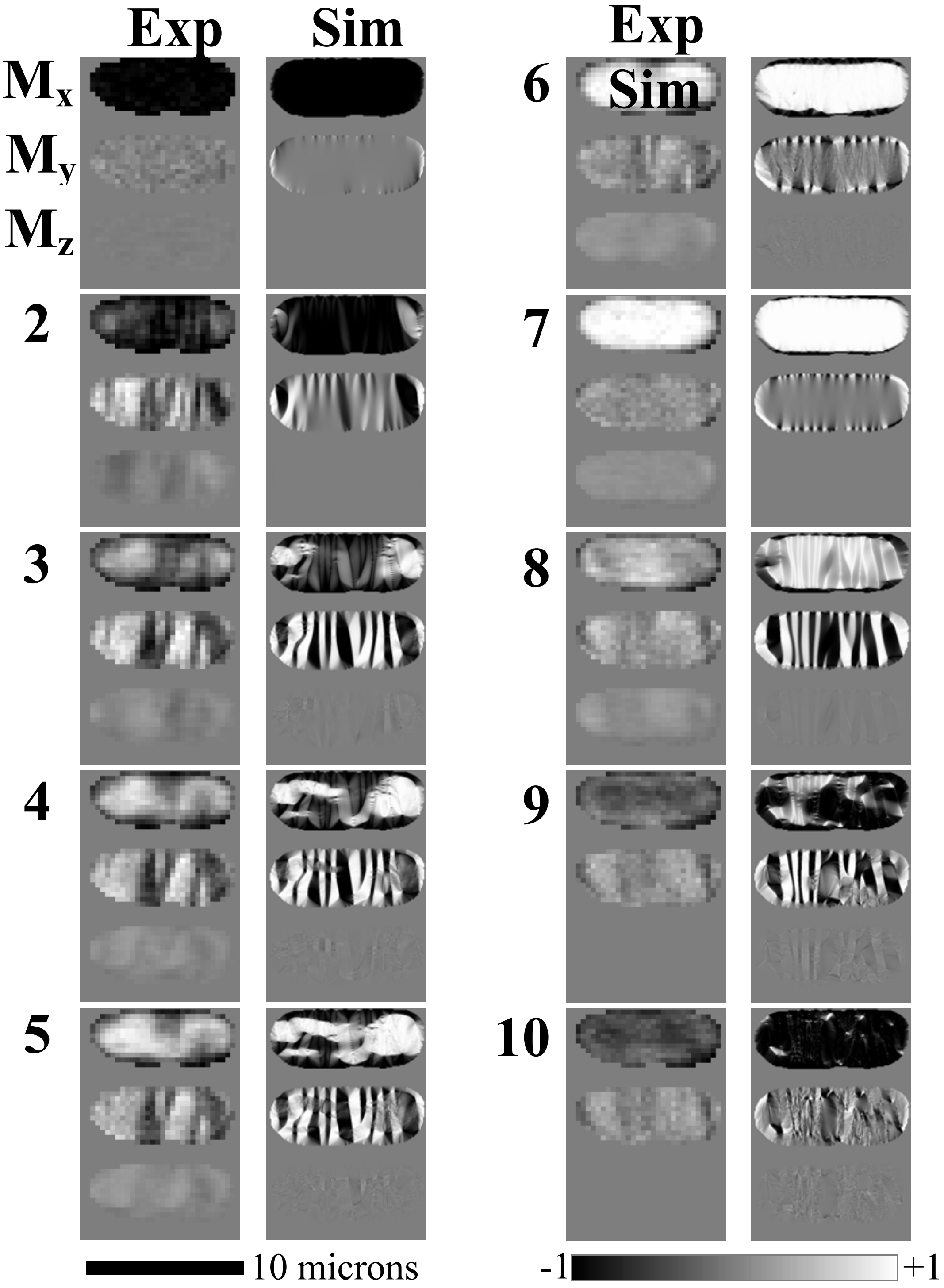

Figure 5.6 Selected frames in the experimental and simulation comparison of the "10x2" sample. External field is 100 Oe. This reversal is incoherent. The sample breaks up into several stripelike domains.

seen, although the positioning of stripes is now somewhat dependent upon sample shape. The reversal response starts earlier because there are more closure domains around the sample edges since they occur at any point of curvature of the edge, instead of only along the two long edges. This allows for more nucleation sites for the magnetization reversal to begin. The end of the reversal also occurs more slowly because the demagnetizing fields from all of these closure regions tend to reduce the local effective magnetic field around the sample edges, thus slowing the dynamics. This curvature of the sample edges increases the switching time significantly. It also reduces the degree of saturation that the sample manages to achieve during the 10 ns reversal pulse. The back reversal is quite similar with stripes developing in roughly the same places.

5.2.1 Comparison with experiment

There are strong similarities between experiment and simulation. To better look at this Fig. 5.6 shows the experimental and simulation reversals with several frames side to side. These frames are chosen at the same percentage reversal, though not necessarily at exactly the same time. The issue of reversal rates is discussed in section 5.3. In this reversal, the rates are quite similar. The comparison shows that the reversal mechanism is quite similar along the front reversal. Both reversals begin along the left and right edges of the sample, and develop in a stripelike instability, which call dynamic domain stripes and meet the center near the curved edge. The back reversal, however, behaves differently. Stripes are not as clear (especially in the y and z magnetizations). In the experimental back reversal, the magnetization “disappears” and then “reappears” in the reversed direction. Possibly this is due to a handful of reversals with stripes appearing in different positions which average to wash out these features.This shows that the Landau-Lifshitz-Gilbert simulation is quite successful even in the case of large angle, strongly driven excitation.

5.2.2 Finite spatial resolution issues

One major discrepancy between simulation and experiment is the finite spatial resolution of the experiment. The data is taken with a 0.75 numerical aperture air objective with 0.7 μm resolution. This means that small spatial features in the simulation cannot be captured in experiment. In order to mimic this, the simulation data is convolved with a Gaussian of diameter 0.7 μm and every 16th data point is chosen, in order to prevent oversampling. These results are shown in Fig. 5.7. The spatial frequencies in the simulation are lowered by this process. They now match reasonably well to experiment. The back reversal still does not agree as well, indicating that its reversal is different in nature. Fig. 5.7 shows that the front reversal is very well captured by simulation.

5.2.3 Crystalline and thermal effects

Some further differences are due to effects that further complicate the experimental case and are not accounted for in simulation. The simulation does not take into effects such as polycrystallinity in the sample and thermal fluctuations of the spin vectors in the sample. We know the sample is polycrystal. This is shown from transmission electron microscope (TEM) snapshots of the permalloy (This is sputtered permalloy which was lifted off the substrate when making a patterned film.) such as Fig. 5.8. It is not possible to know the actual polycrystalline structure of our sample. Even if we did know it, a simulation with a sample as big as the ones we have used in our experiments with as many crystal grains as would exist, with appropriate shapes and sizes would be prohibitively difficult. Smaller samples are needed in order to solve this problem. This problem could be avoided with a single crystal sample, but thus far none have been available. There are reduced exchange coupling and varying anisotropy axes across grain boundaries. This would pin magnetization in certain regions. The polycrystalline nature of the sample would serve to smooth out and slow down the magnetization reversal. Evidence for this pinning is presented in section 5.3. These crystals further complicate the energy landscape giving access to more metastable states in experiment.

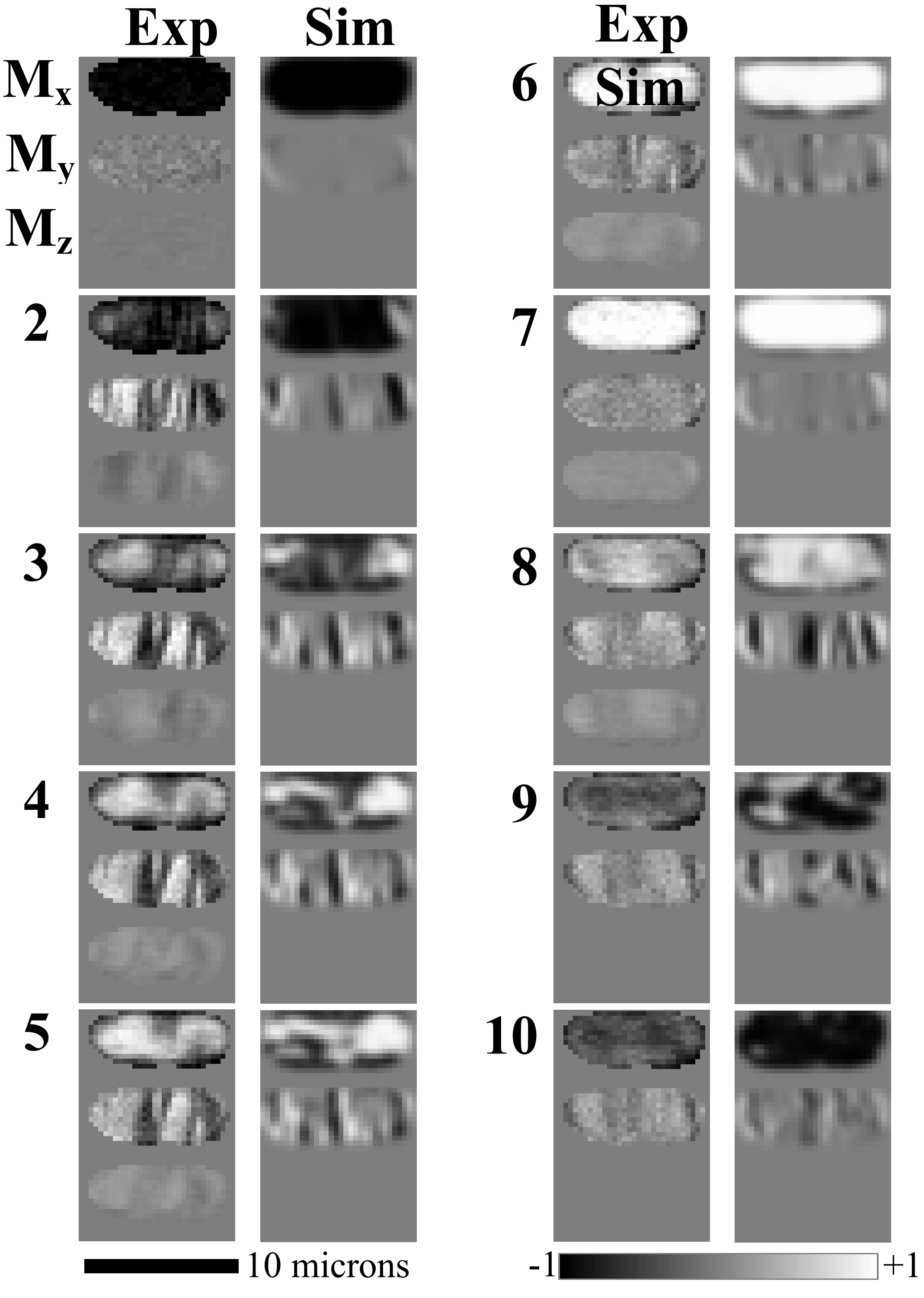

Figure 5.7 Selected frames in the experimental and simulation comparison of the "10x2" sample. External field is 100 Oe. This reversal is incoherent. The simulation frames are Gaussian convolved and every 16th point is selected to better match the scanning algorithm. The magnetostatics dominate this reversal, leading to a good agreement.

Crystallinity further complicates things. Initially, the crystalline sample will be in a state with a “magnetization ripple” [79] in the x-component of magnetization which is caused by the magnetization in some crystal grains being misaligned with the external field due to differing properties (ie. anisotropy axes) in different grains. In “saturation” the sample is not fully saturated due to this effect. This allows for some initial torque withing the sample. This likely leads to an earlier magnetization response within the centre of the sample, as there are spins which are not perfectly aligned with the magnetic

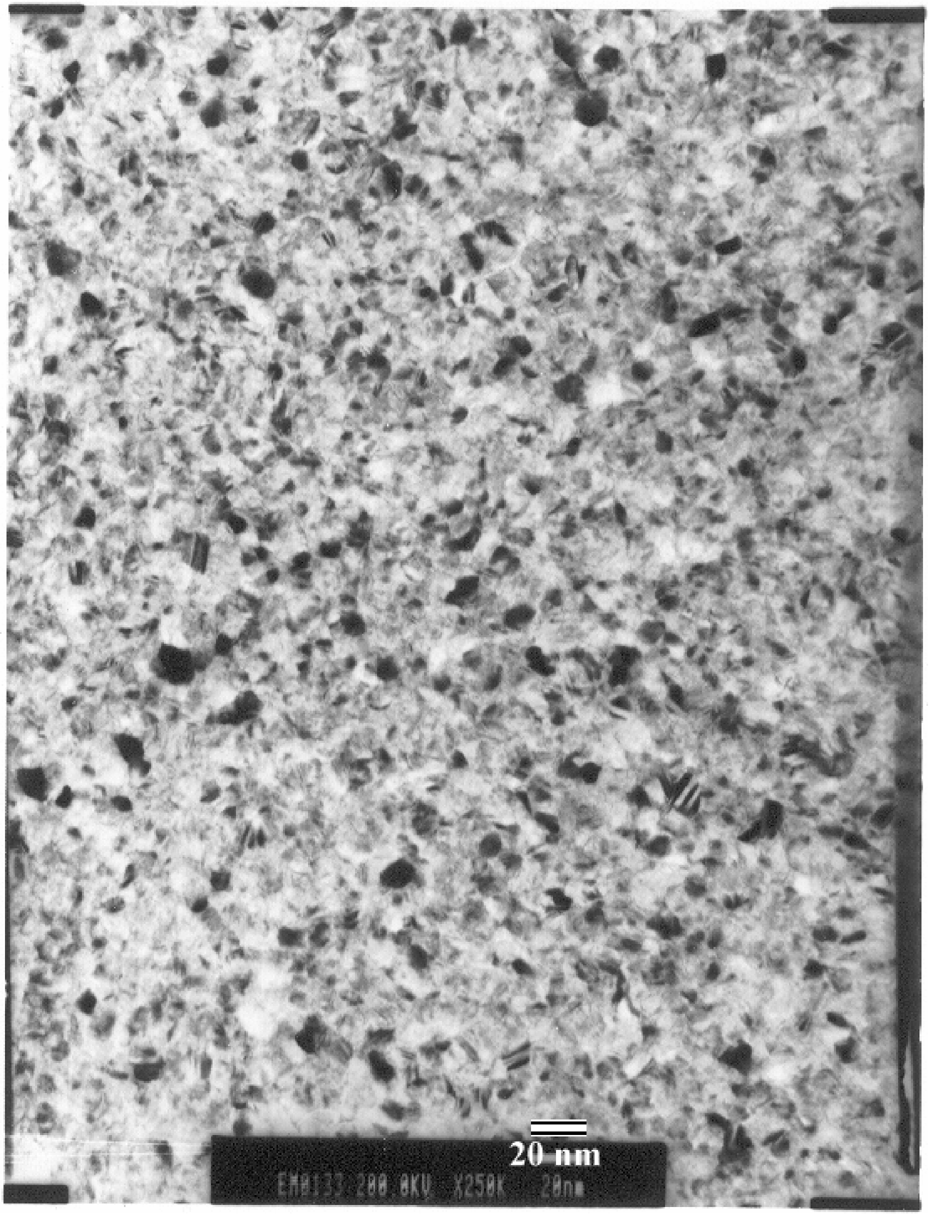

Figure 5.8 Transmission electron micrograph of polycrystal permalloy showing complex crysal structure with nano-sized crystal grains.

field. This helps to explain why the response of the experiment starts earlier in the sample center than it does in simulation.

Because cell sizes used in simulation are larger than the crystal grains, some of the permalloy properties are those of an "effective" medium of several crystal grains and not that of single crystal permalloy. The exchange constant and anisotropy constants used are averages over several grains. In order to attempt a simulation with single crystal permalloy, or with cells that were as small as crystal grains, this would have to be corrected.

Metastability is more of a problem in this comparison when thermal fluctuations are not taken into account, but the experiment is done at finite temperature. Because the experiment is done at room temperature, there will be Brownian motion of the magnetization vectors within the sample. This is addressed in chapter 6. Random thermal fluctuations of the magnetization vector can be added by solving the Fokker-Planck equation.[80] In the real world experimentation, since it is stroboscopic, only the repetitive portion of the dynamics is captured. The reversal would have to be simulated many times with different thermal fluctuations and averaged to give a "stroboscopic" signal. Unfortunately, this is prohibitively hard to do with a sample as big as this one. Thermal fluctuations will serve to average out stroboscopic signals. They make magnetization curves look more exponential after averaging. When lots of metastable states exist, this wash out features in the experimental sample. This appears to be what is seen on the back reversal in the experimental sample. This is understandable because the sample is driven by 60 Oe on the back reversal (vs. 100 Oe on the front). It will be more strongly pinned, and it will have more metastable reversal paths that may become stroboscopically averaged.

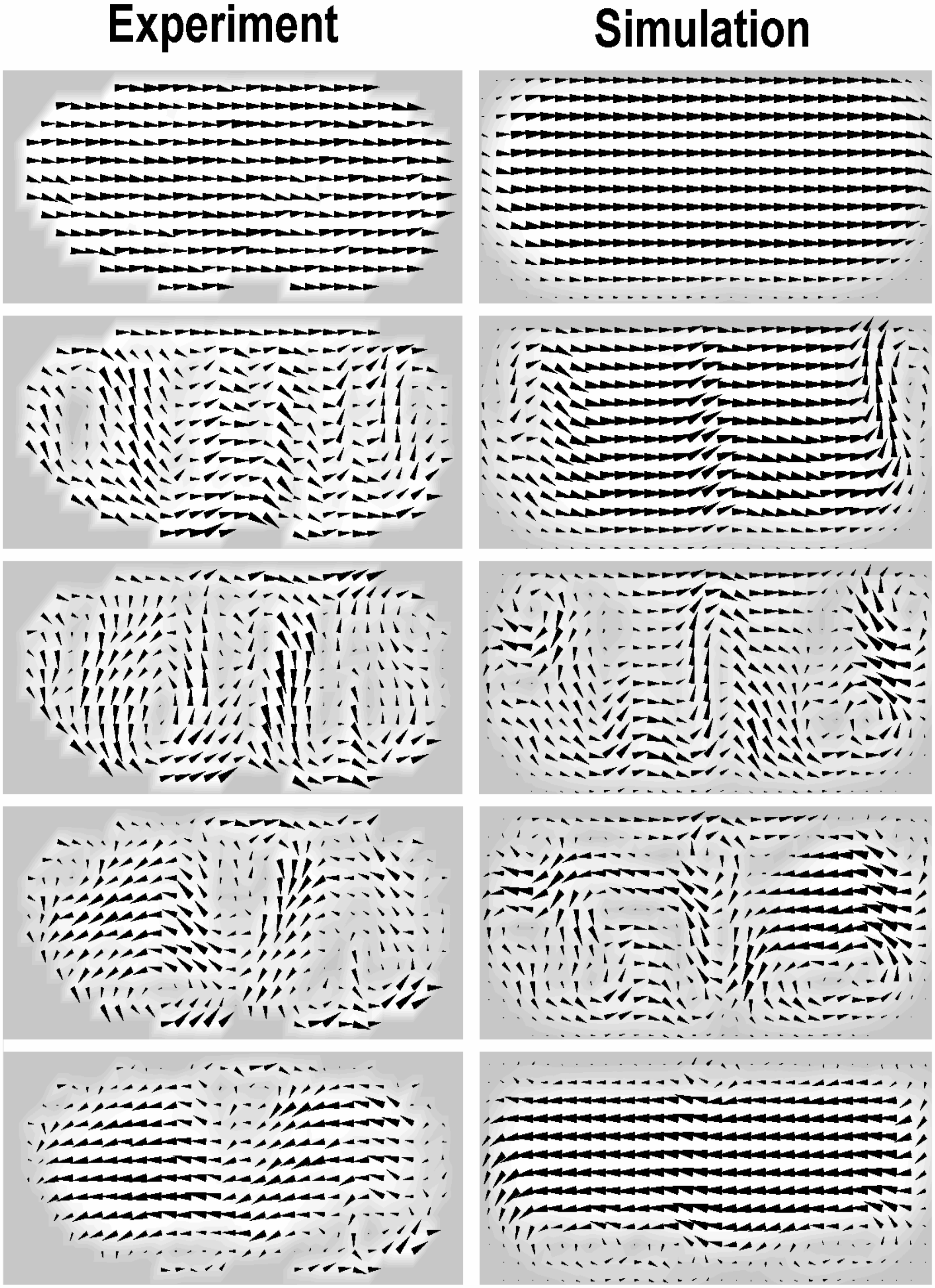

Figure 5.9 Vector maps of “10x2” front reversal. The arrows represent the direction of M and their length its magnitude. Grey scale also shows magnitude of M. Where it is darkest grey, M is reduced due to averaging of simulation of finite spatial resolution of experiment.

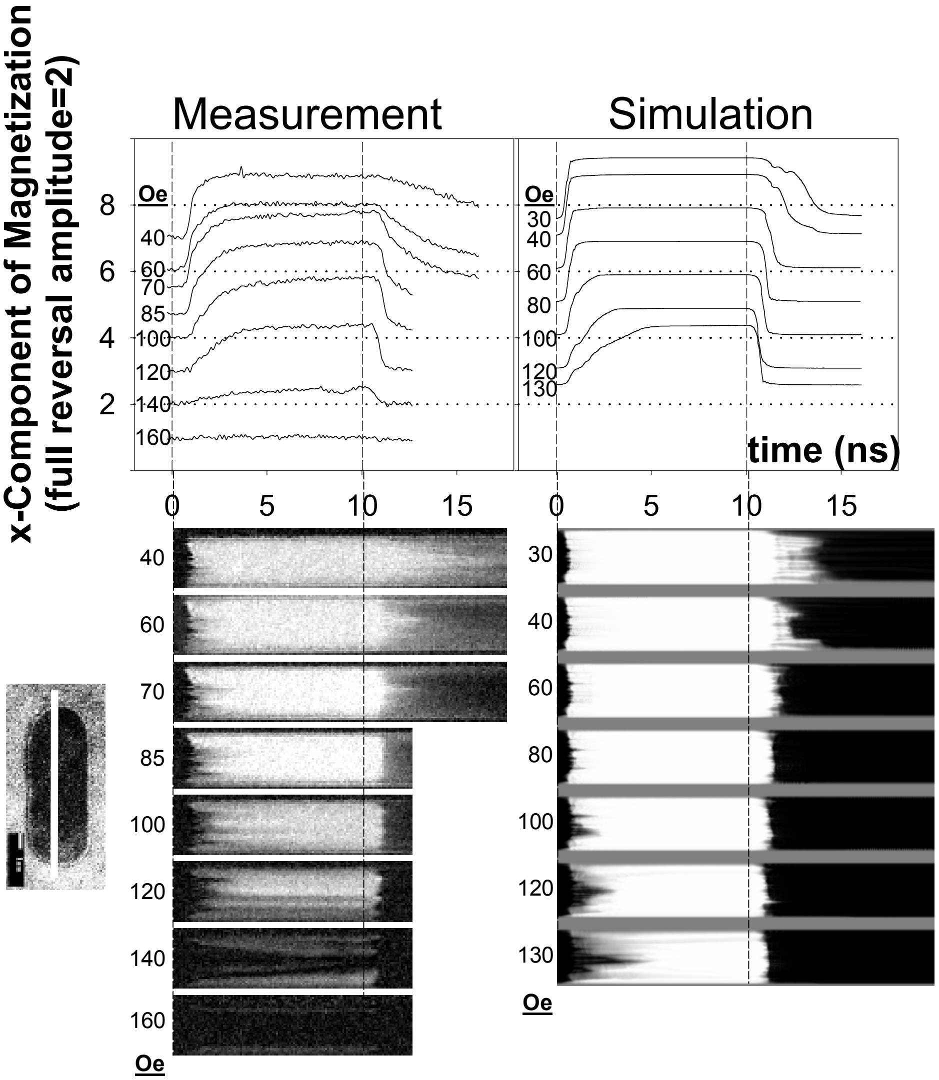

Figure 5.10 Line-scans and line scan averages vs. time (x-component) for "10x2" permalloy element as a function of DC magnetic field. A similar envelope "V" or "U" shape is seen in both experiment and simulation. In both cases the onset is later and the reversal time is longer with lower driving field. At higher driving field both agree well. At lower driving field, simulation is faster. This implies pinning of domain walls etc. on crystal boundaries in experiment.

5.2.4 Vectorial representation

We have enough information in the previous figures to represent the experimental magnetization profile in a vector map and enter the realm of “experimental micromagnetics”, in the sense that experiment can produce results that are directly comparable to that of micromagnetic simulation. The problem of calibrating the polar and longitudinal Kerr effects can be neglected, as almost all of the action occurs in the xy plane and is captured by the longitudinal Kerr effect. Because of spatial averaging, some vectors will be significantly shortened from the saturation magnetization length. A comparison of the rising switch (with best agreement) is shown in a vector map in Fig. 5.9. A greyscale in the background indicates where the magnetization vector is reduced in length due to spatial averaging. This also occurs in the simulation because the Gaussian blurred data is used for this comparison. Both of these vector plots show vortices that enter and are expelled from the sample in similar places along the sample top and bottom edges (reminiscent of Bertram and Zhu [57]).

5.3 Magnetization Reversal with other DC fields

We can now investigate magnetic reversals with varying DC fields in order to see the effect of driving field on the reversal process. We look at “x-t” data across the sample to get an idea of what is going on. Due to symmetry of the sample, one only needs to take data on one horizontal spatial line across the sample and scan it in time. This is far more telling than one spatial spot on the sample. Experimental and simulation comparisons are shown in Fig 5.10. The line scan average curves show relatively similar features. There tends to be a fast rise or fall in magnetization when the driving field is large and a much slower one under a smaller driving field. When driving fields are low, the increase or decrease in magnetization is not smooth, there can be bends in the magnetization curves. Some of the extra “noise” in the experimental curves may be thermal fluctuations in the sample, leading to small changes in magnetization even when the external magnetic field is constant.

Looking at the x-t scans, we can see further agreement. A reversal always happens first at the edges of the sample and happens later in the sample middle. This is shown in the U or V shaped envelopes of the reversal data on both the front and back slopes. There are similar notches (spatial stripes) along both the experiment and simulation. These appear to be long wavelength standing spin waves which are magnetostatic in origin[34].

The most telling difference is the sharpness of switching that occurs. In simulation the switch may take a while in a low driving field (i.e. front slope at 130 Oe DC field), but when it does occur, it is a complete switch. In the experiment the switch is not as sharp. Metastability enters the picture. The experimental sample is more metastable due to crystallinity, possible non-magnetic defects, variation in the thickness, and other things that will serve to make the energy landscape more complex. When thermal fluctuations are also considered, a more complex energy landscape will lead to non-repetitive switching. Even worse, it may lead to non-repetitive initial conditions for each reversal. All this will tend to reduce the sharpness of the switch in the experimental data. This difference is most telling in the experimental data when the driving magnetic field is small. A larger magnetic field will be able to reduce the effects of these imperfections in the experimental sample.

This is consistent with the line-scans. The switches occur at similar rate in high driving fields but are slowed in lower fields, due in part to pinning in the sample. In experiment, when the sample becomes highly metastable, the dynamic domain structure of the reversal is washed out and magnetization vectors shrink significantly. This is what is seen in the back reversal. The crossover from repeatable reversals to metastable ones with this sample appears to occur with driving fields around 85 Oe.

This can be more clearly seen by looking at the switching times shown in Fig. 5.11. Switching times are defined here as the time a sample takes to go from 20% reversed to 80% reversal. These values are chosen because they tend to be within the fast rise on the switching curves. Similar results are seen with other definitions of switching time, as long as they avoid the slow exponential rolloff near saturation that occurs often in experimental traces. For higher driving fields (below about 100 Oe DC on the front reversal and above 80 Oe DC on the back reversal), the switching times agree well. Discrepancy occurs for lower driving field, where pinning is more significant. On the front reversal, the simulated switching time is larger than the experimental one for low driving fields. This suggests that imperfections in the experimental sample, such as crystal boundaries, provide extra nucleation sites allowing the reversal to proceed faster at the center of the sample. On back reversals, the experimental sample switches faster. This is because the same imperfections that slow the front reversal prevent the sample

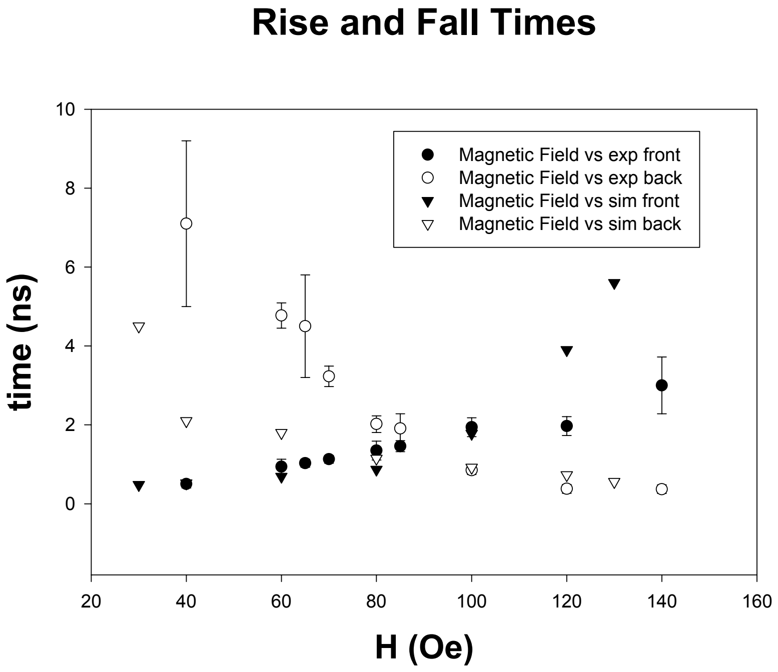

Figure 5.11 Rise and fall times for magnetic reversals in both experiment and simulation. Times are defined as the time to go from 20% to 80% reversed. Good agreement in high driving fields. Discrepancy in low driving fields where pinning becomes significant

from reaching a fully saturated state, so it does not take as long to switch back. Presumably, metastability in switching also occurs in these cases.

5.4 Magnetization Reversals with other sample shape

Further investigations were done with a sample 7.7 x 16.5 μm ("6x15") sample with a long axis perpendicular to the external field direction. Experimental traces and snapshots are shown in Fig. 5.12. The experimental snapshots only show part of the structure because the piezo range is too small to scan the whole sample. The simulation traces and snapshots are in Fig. 5.13. It is obvious that this reversal occurs by different mechanisms than the dynamic domain reversal we saw in the "10x2" sample. First we will focus on the back reversal. In both cases it occurs quickly and oscillations are seen in the y and z magnetizations. There is also a hint of some oscillations present in the x component which are washed out due to temporal jitter in the measurement and "lost" in the large switch in magnetization of the sample. The precession in the x component is at twice the frequency of the precession in y or z component. In the yz plane, the oscillations in y are out of phase with those in z. The spin points in the positive z direction, then the negative y, then negative z and finally positive y directions before repeating. However, in the x direction, when it switches it only points in one direction in x so it will produce maxima in x twice during each rotation. It will produce maxima as it passes through zero along the y axis and once as it passes through zero along the z axis. This is a near-ideal precessional reversal.[81] This can better be seen with vector images that are shown in Fig 5.14 for experiment and Fig 5.15 for simulation.

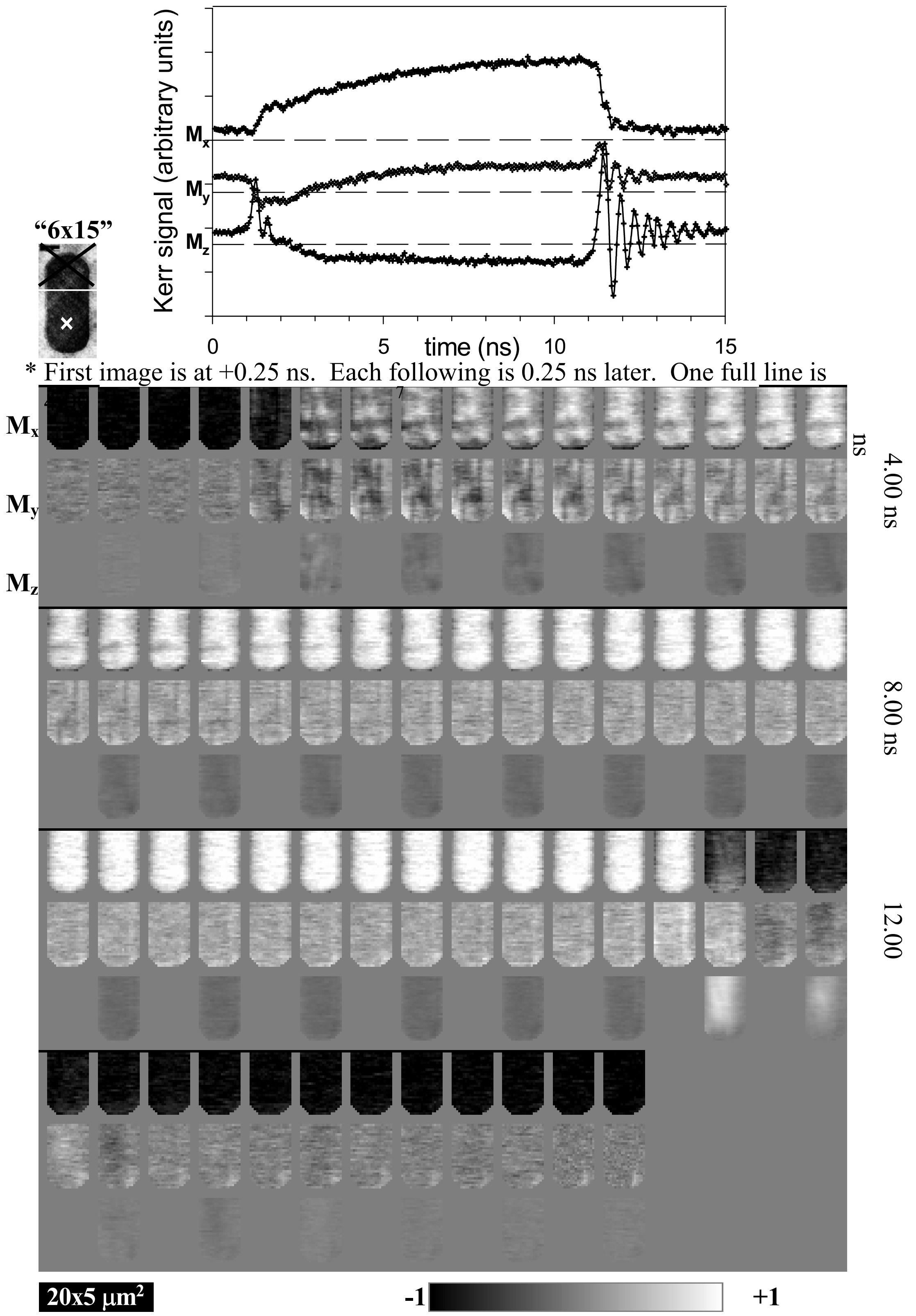

* First image is at +0.25 ns. Each following is 0.25 ns later. One full line is

Figure 5.12 Spot trace and montage data for 7.7 x 16.5 micron element in 100 Oe field. The differing aspect ratio from "10x2" sample leads to more oscillatory behavior.

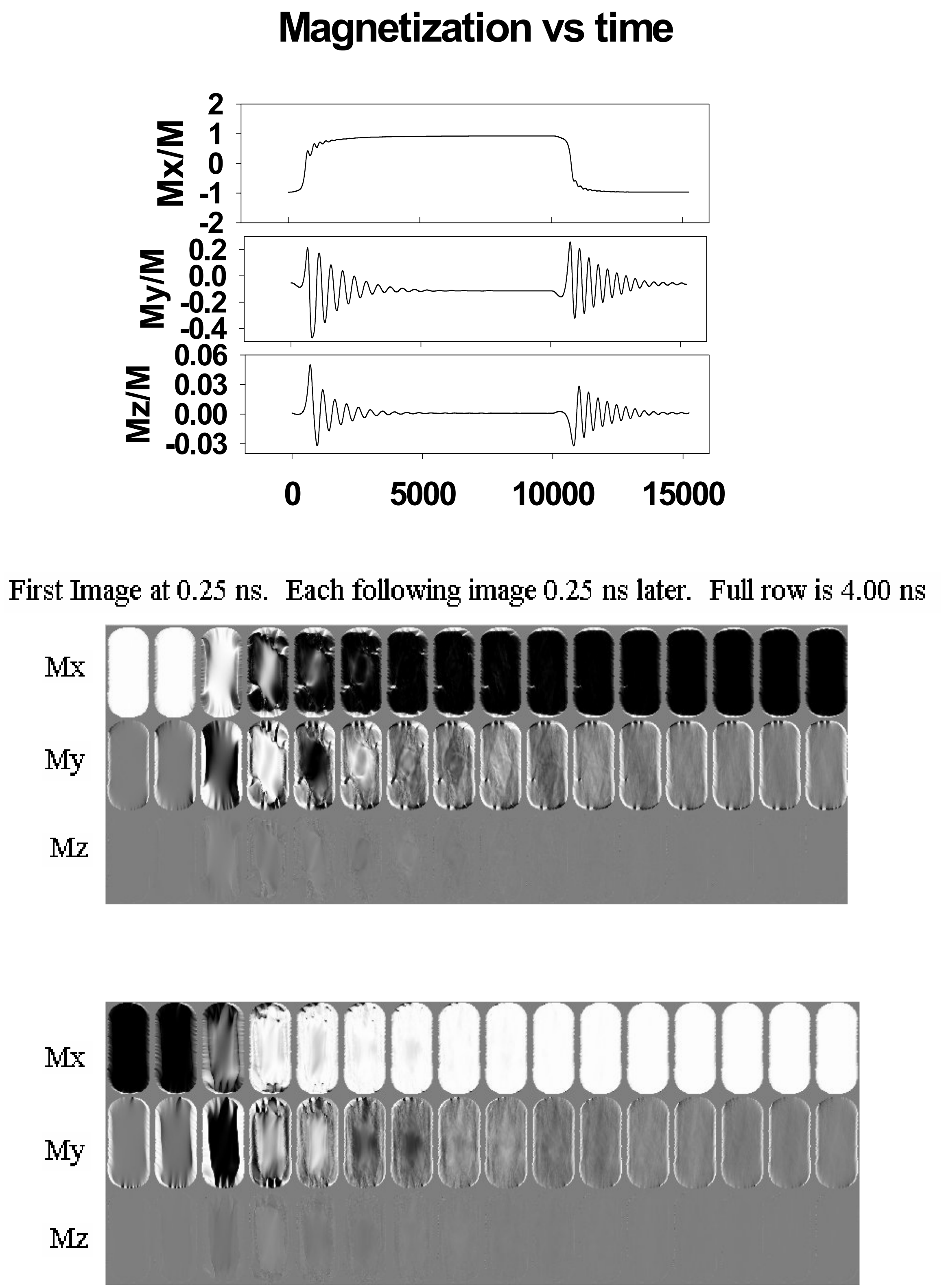

Figure 5.13 Simulated magnetization reversal of 7.7 x 16.5 micron sample in 100 Oe. The differing aspect ratio than the “10x2” sample leads to more oscillatory behavior

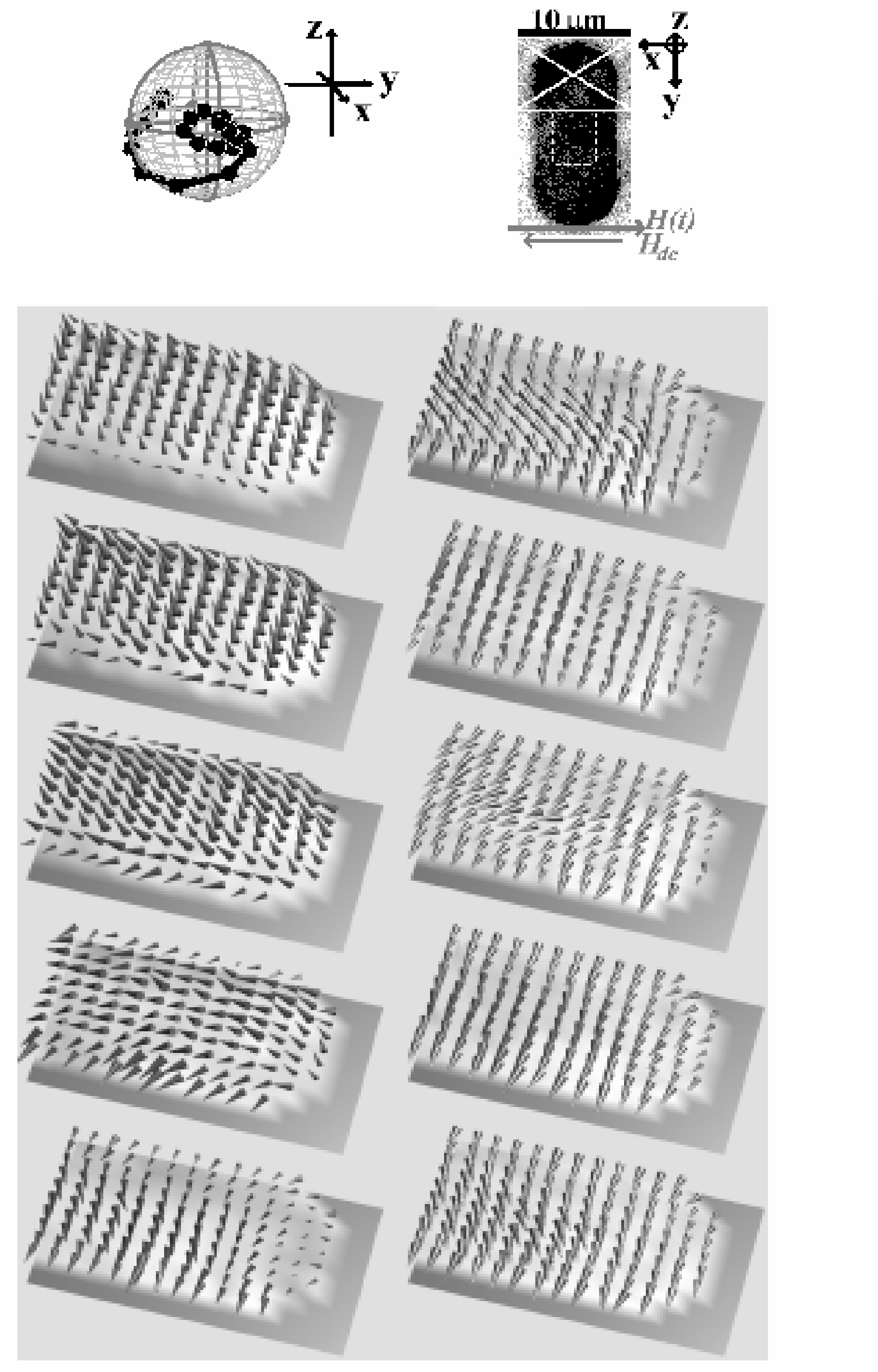

Figure 5.14 Experimental back reversal of “15x6” sample cast into a vector map to better show the coherent rotation. Top left corner shows path of the magnetization vector in the sample center as it rotates coherently. There is uncertainty calibrating strengths of out-of-plane signal to in-plane signal. This is ignored and raw signal strengths are plotted.

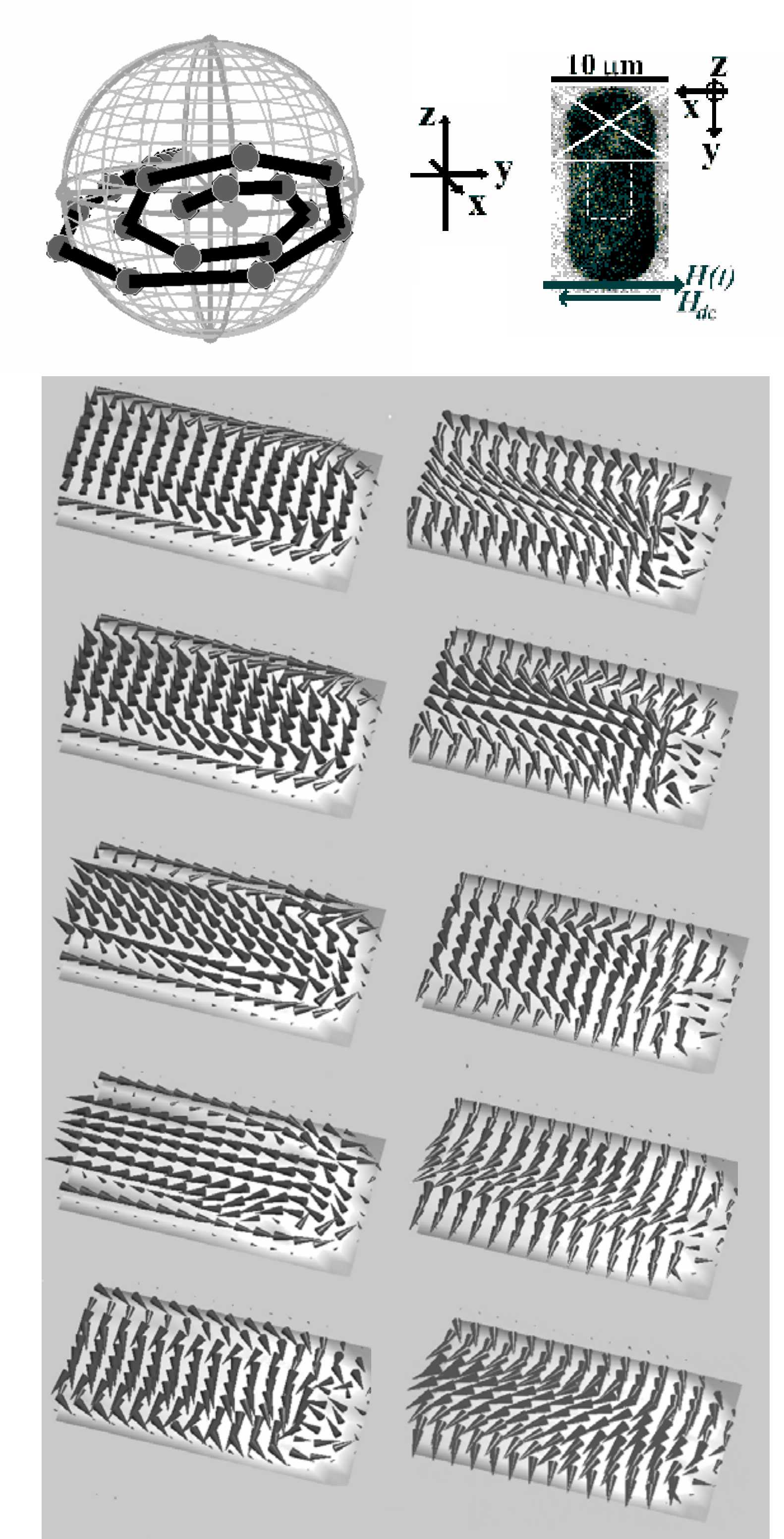

Figure 5.15 Simulated back reversal of “15x6” sample cast into a vector map to better show the coherent rotation. Top left corner shows path of the magnetization vector in the sample center as it rotates coherently. Because of the problem calibrating the relative strengths of in and out of plane Kerr signals in experiment, Z signal is multiplied by 5 in this rendering to better match the experimental data.

There is some uncertainty in how large the z component of magnetization should be, since it relies upon polar Kerr effect instead of longitudinal effects. In this comparison, the experimental data is used "as is" and the z component in the simulation is multiplied by five to roughly mimic the increased sensitivity to the polar Kerr effect. In both cases a precessional reversal [82] is seen. A precessional reversal is a half cycle of uniform ferromagnetic resonance rotation. A transverse magnetic field pulse will send the magnetization out of plane. An out-of-plane demagnetizing field is then created, around which the magnetization in the plane can precess.

There is discrepancy on the front slope of the reversal, where the coherent oscillations in the experimental sample are less evident. Since the driving field is 60 Oe on the front slope and 100 Oe on the back slope, the main reason for this discrepancy increased metastability leading to increased importance of thermal fluctuations.

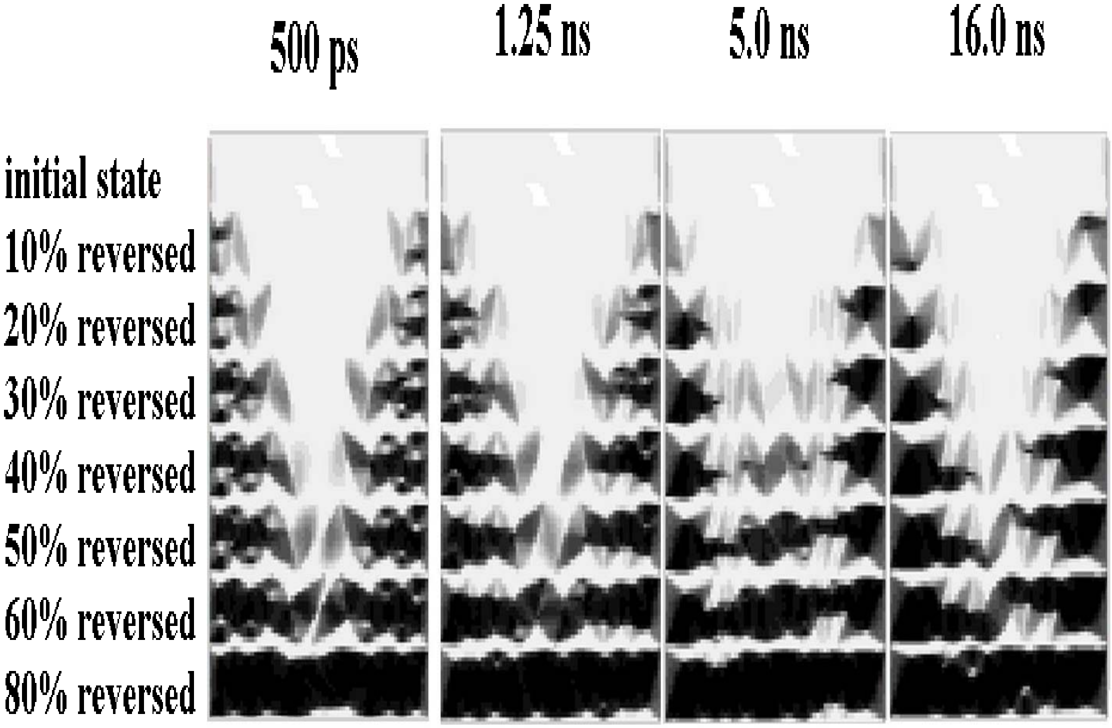

Figure 5.16 10x2 micron sample in 100 Oe DC with 160 Oe reversal pulses of varying rise times. There is significant difference in the dynamics in the intermediate states by changing only pulse risetime.

5.5 Magnetization Reversals with different switching field risetimes

A fundamental issue throughout this work is the fact that these reversals are dynamic. Quasi-static magnetization reversals have been studied extensively in the 1950s and 1960s (Doyle [20] gives a good summary). This work tends to neglect the gyrotropic nature of the magnetization vector and, thus, only look at the magnetization in equilibrium states during the reversal. Of course this begs the question of how it gets from one equilibrium state to the next. In this work, the motion is assumed to be quasi-static, only out of equilibrium by an infinitesimal amount at any given time. It is the non-equilibrium nature of dynamic motion that makes this work new and interesting. Just how different quasi-static and dynamic reversals are is a somewhat open question that can be addressed by simulation. Using a rectangular 10 x 2 μm sample we can run simulations with different rise times of the switching magnetic field. These results are shown in Fig. 5.17. The rise time of the reversal pulse is varied. Like the experiment, the sample is held in a field of 100 Oe, and a 160 Oe reversal pulse that is antiparallel is applied to switch it. Runs are done with switching field risetimes of 500ps, 1.25 ns, 5.0 ns and 16.0 ns. Naturally, the switching time is dependent upon the rise time of the reversal pulse (i.e. it takes longer than the length of the reversal pulse to switch). States are compared by percentage reversal and not time. It is clear that with different rise times, the sample will attain different magnetization states. With fast enough switching, the switch nucleates at the demagnetized ends of the sample and propagates into the sample center in a stripelike pattern. It meets in the sample center and then pushes out to the short edges of the sample. When there is sufficiently slow switching there is time for nucleation in the center of the sample to occur. It occurs first as a continuation of the stripelike spin wave pattern. Energetics in the center of the sample can be quite complex. The pattern in the sample center is very dependent upon exactly how it nucleates. This difference could easily be detected in a TR-SKEM experiment as long as it is repetitive. There is concern that because the energetics are so complex, there may be metastability that will make this detection more complicated. It is clear that there are noticeable differences between quasi-static and dynamic reversals.

5.6 Magnetic reversal with different orientation of transient and DC fields

The dynamic domain reversal that we see in most of these reversals is a consequence of the fact that initially there is no torque on most of the sample. **M x H** is zero when **M** and **H** are anti-parallel, so the reversal is driven mostly by magnetostatics starting from the two end closure domains. This situation can be avoided by providing a transient field which is not completely anti-parallel to the DC field (and thus the initial magnetization). This will speed up the reversal, making it more of a precessional reversal. An example of this is shown when the transient field is canted so that it is 150° with respect to the DC (as opposed to 180° in the anti-parallel case) in Fig 5.17. This rotation is quite coherent. Large oscillations in the magnetization are seen. When the field mismatch is 10° (170° canting), the oscillations are gone, but the spatial pictures show that the reversal is much more of a coherent rotation. This is shown in Fig. 5.18. When the field mismatch is 5° (175° canting), the spatial pictures reveal that the sample breaks up into stripelike domains that reverse both clockwise and counterclockwise. There is still a significant difference between the 5 degree mismatch and zero mismatch as a non-reversed domain remians trapped in the sample centere and takes a long time to reverse. The rotation becomes much more incoherent (as is the case with zero field mismatch. seen in section 5.2). These examples show that by merely varying the angle between the field, wide changes in behavior are possible. Combining these effects with varying rise times and varying sample shapes provide a huge range of magnetic reversal behavior that can be studied. Some experimental exploration into this area is provided by Choi et al [52,70] .

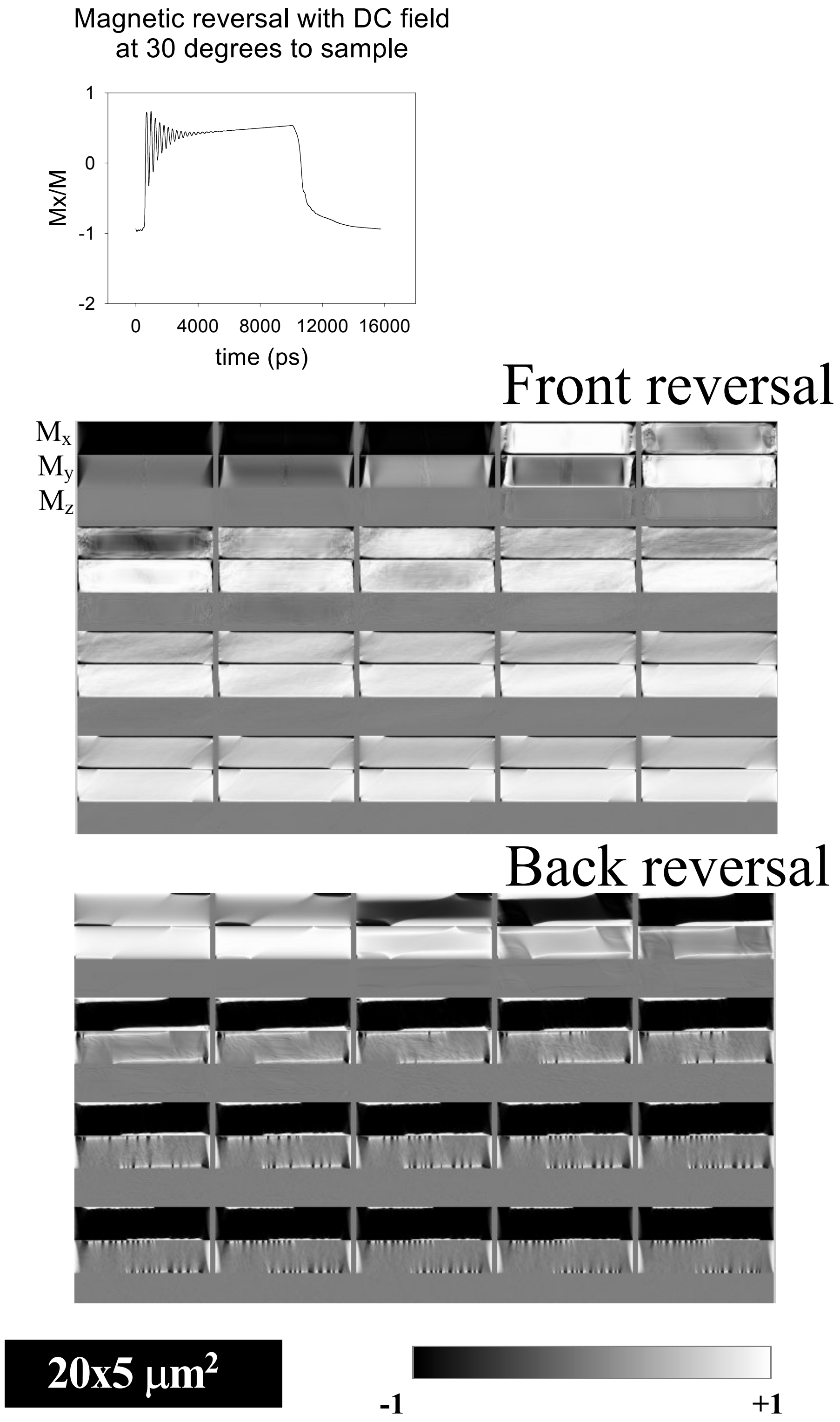

Figure 5.17 Simulated magnetization reversal of 10 x 2 micron sample in 100 Oe with a 160 Oe reversal pulse directed 30 degrees from anti-parallel. A coherent rotation occurs due to the hard axis pulse breaking symmetry

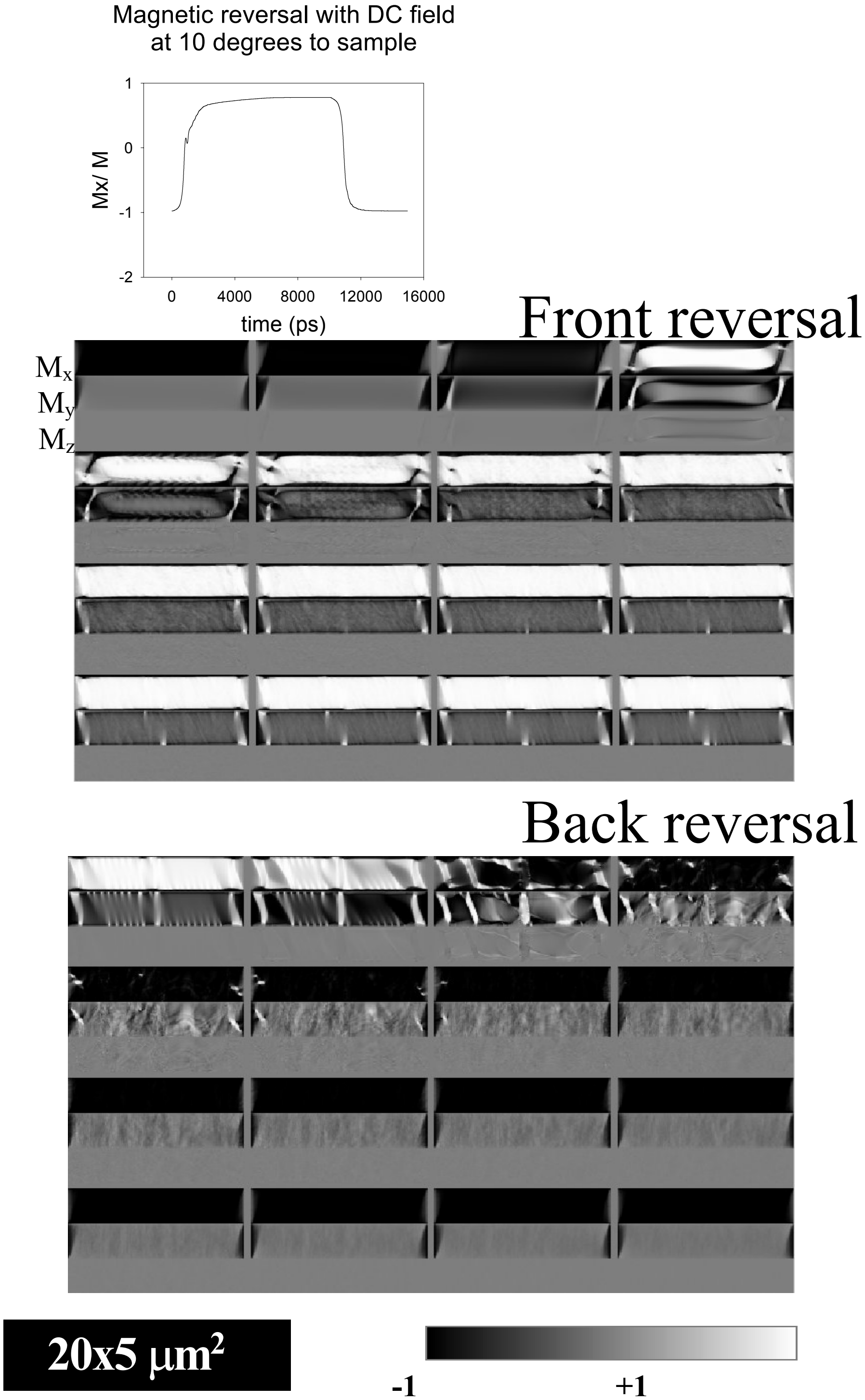

Figure 5.18 Simulated magnetization reversal of 10 x 2 micron sample in 100 Oe with a 160 Oe reversal pulse directed 10 degrees from anti-parallel. Rotation is more coherent but oscillations are not seen.

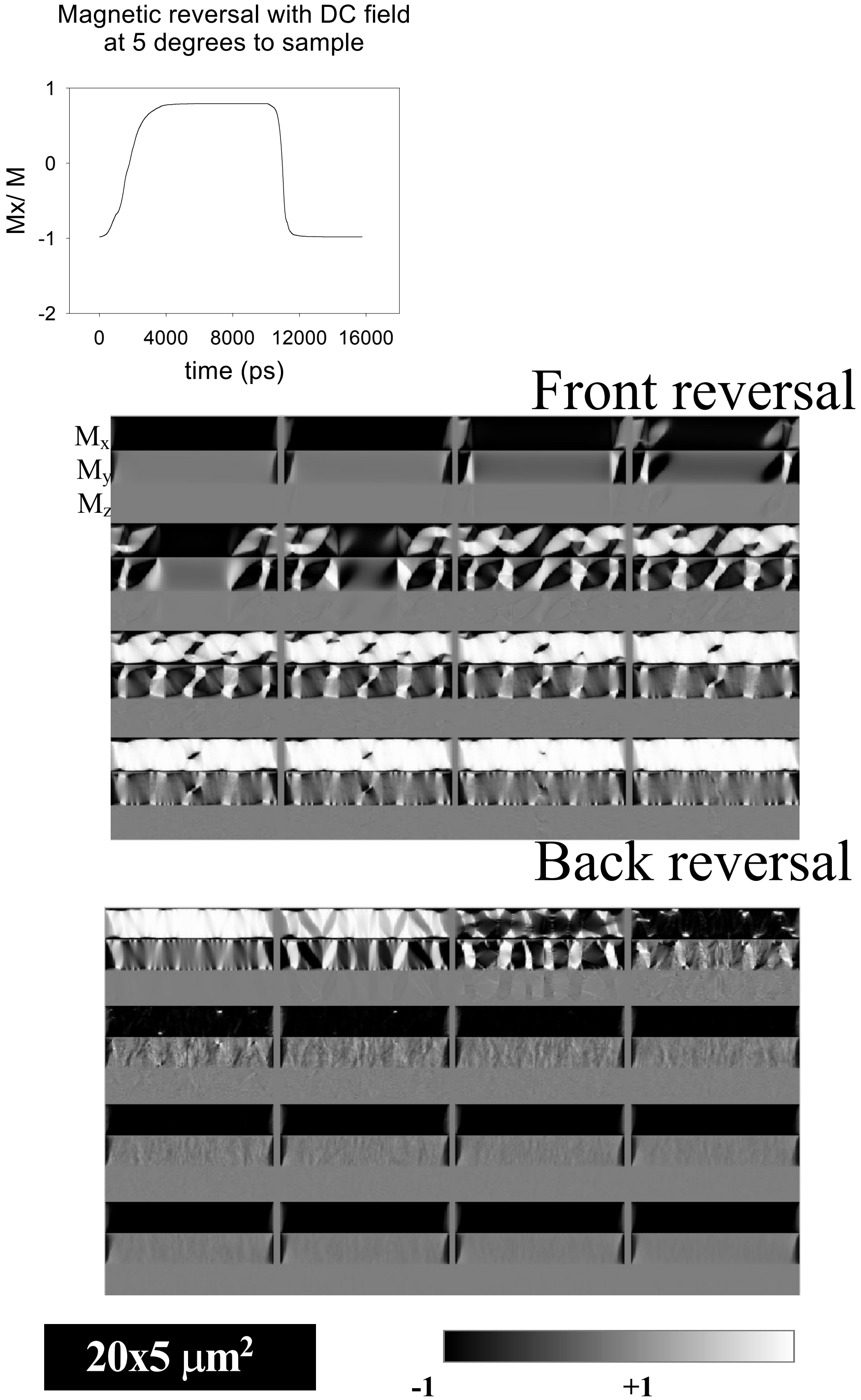

Figure 5.19 Simulated magnetization reversal of 10 x 2 micron sample in 100 Oe with a 160 Oe reversal pulse directed 5 degrees from anti-parallel. Rotation is more incoherent. Striplike domains are seen.

5.7 Magnetic reversal in samples with defects

The effect of a defect can also be checked with simulation. One or more cells within the sample can be masked such that they have a saturation magnetization that is zero or less than the saturation magnetization in the rest of the sample. One defect can have significant effect on the magnetic reversal in the sample. This will be shown through several examples. The 10 x 2 μm sample is simulated again with a 1 cell defect in the center, a 1 x 3 cell defect in the center, a 3 x 3 cell defect in the center and two 1 cell defects at thirds along the center line of the long axis. These can have significant effect upon reversal rates. A graph of this is shown in Fig 5.20. Larger defects tend to have closure domains around them, which can serve as nucleation sites during the reversal, thus reducing the pinning effect of the defect. Smaller defects are not large enough to create closure domains and merely pin magnetization around them, thus the simulations with one cell defects are the slowest to reverse. As defect size becomes small when compared to the exchange length of the material, this trend probably reverses, as the defect is less significant. The simulation code is not capable of exploring that scale with samples of that size, so that remains speculation. This is a possible explanation for the simulation reversals being faster than the experimental ones. The experimental ones may have small defects. These defects may not be points where magnetization is zero as in these simulations, but there may be a significantly reduced magnetization in these regions of the sample. This would serve to slow magnetization reversal as well as complicate the energy landscape. Adding defects is yet another variable that can be explored in magnetization dynamics experiments.

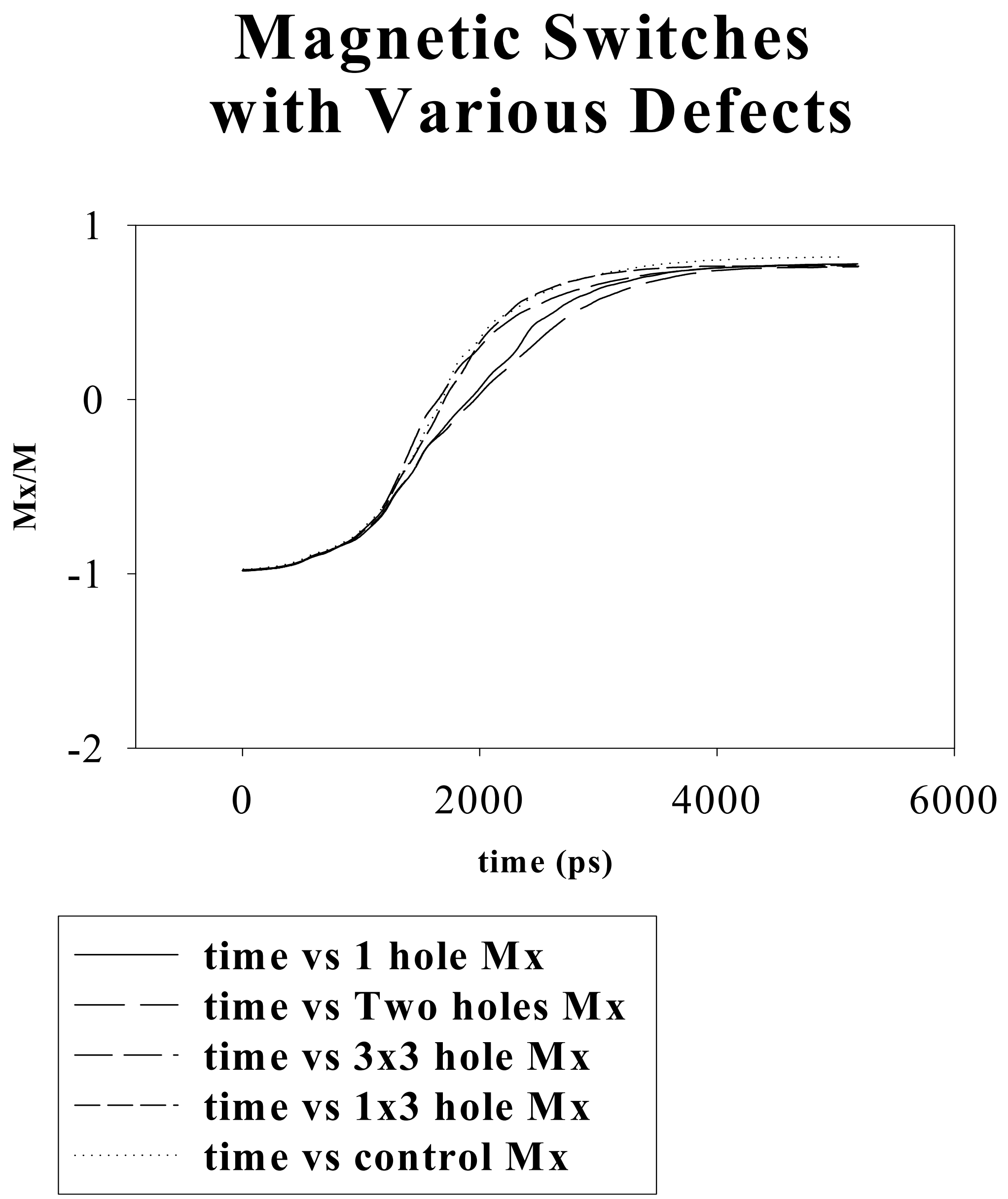

Figure 5.20 Simulated magnetic switches of various 10x2 micron samples in 100 Oe DC with patterned defects. Defects slow reversal, due to pinning.

1024 x 256 cells

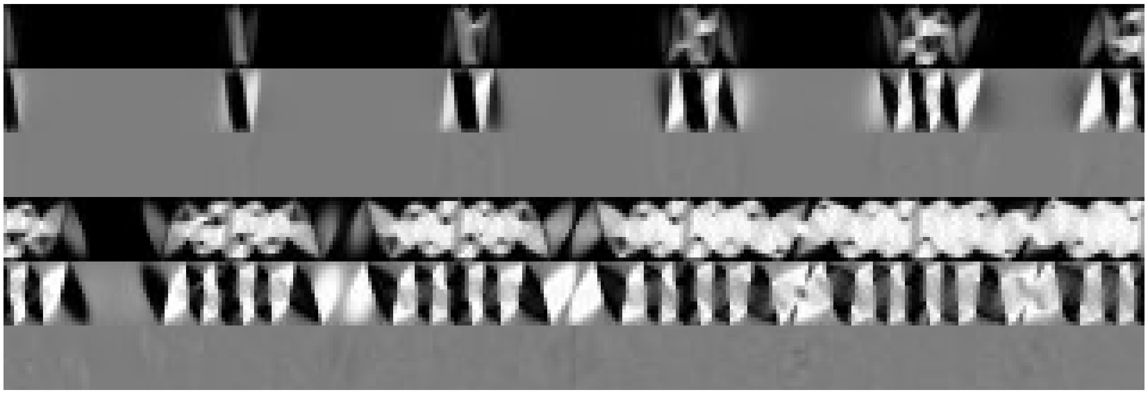

512 x 128 cells

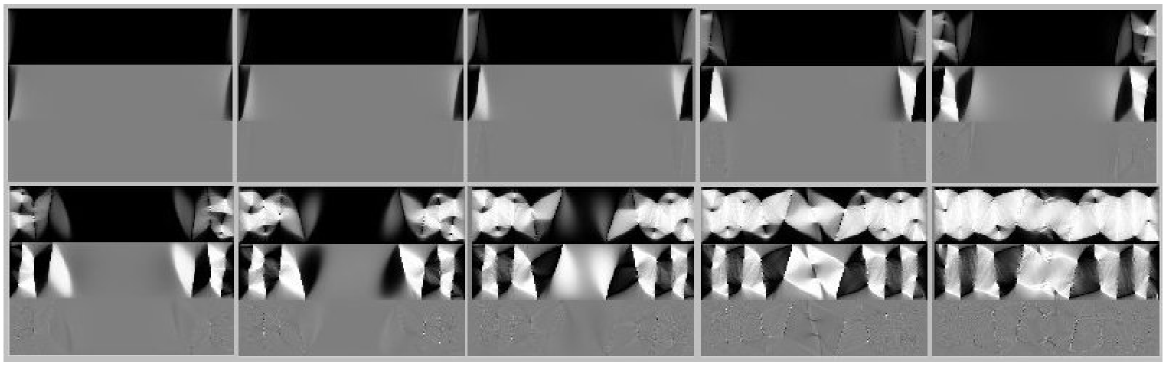

Figure 5.21 Simulated initial switch of magnetization reversal of 10 x 2 micron sample in 100 Oe with a 160 Oe reversal pulse with smaller cells (1024 x 256 cells) compared to the switch with 512 x 128 cells. Since this is very similar to previous simulations, we have confidence cell size is not an issue.

5.8 Cell size test

These reversal simulations have all used cells approximately 15 nm in size. Since this is larger than demagnetizing exchange lengths, there is concern that it may not be an accurate result. Its correspondence with experimental results puts this issue somewhat to rest, however repeating a simulation with even smaller cells and finding the results to be almost identical is more convincing. The 10 x 2 μm reversal is repeated with 1024 x 256 cells (making for cells of dimension 9.77 x 7.81 nm). This is shown in Fig. 5.21. It looks very similar to the previous simulation in Fig. 5.4 with larger cells. Thus we can conclude that cells used in these simulations are small enough to capture the dynamics.

5.9 Energy in Magnetic Reversal

With these simulation and experimental results, it is possible to analyze the various energy terms during the reversal. We will look at the 10 x 2 μm reversal that has been studied before. Fig. 5.22 shows the major energy terms, exchange, demagnetizing and Zeeman in this reversal (Since anisotropy energy, averaged over the whole sample, does not change much during the reversal it is omitted from this graph.). The simulation with 1024 x 256 cells is used to generate this graph. During the changes in magnetic field, there is a large spike in the total energy of the sample, and in its components. This energy is dissipated quickly due to damping. Because it is in a different magnetic field, the sample will come to a different equilibrium in energy during the magnetic field pulse, than when it is in outside of it. When the pulse is removed, the sample returns to its initial energy values. There is not enough spatial resolution in the experiment to make a meaningful energy plot. Both the exchange and demagnetizing energy will be significantly underestimated because the higher frequency magnetization changes are lost.

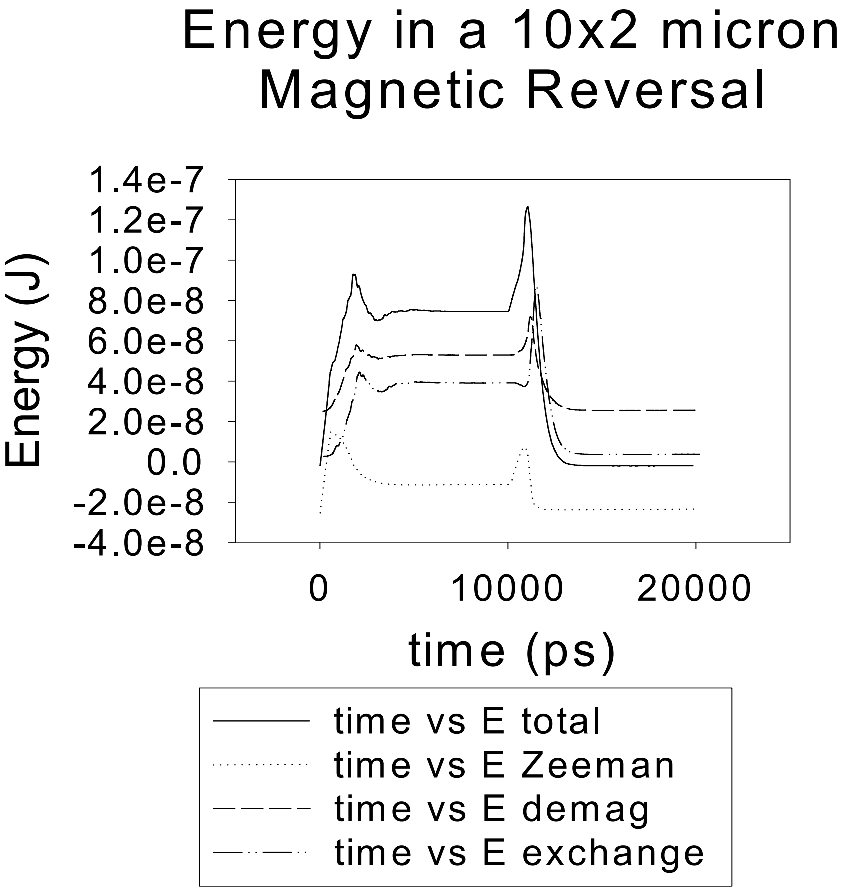

Figure 5.22 Energy plot during 10x2 micron reversal. Energy terms peak when external magnetic field changes and damp back to equilibrium afterward. In this plot the zero point is chosen arbitrary so that initial state has zero energy.

5.10 Summary of this Chapter

In this chapter the magnetization reversal problem is explored. Experimental results and micromagnetic simulations of several problems are introduced and compared. The details of the experimental time resolved scanning Kerr effect microscopy (TR-SKEM) method is reviewed and the sample geometry is discussed. Experimental results of an incoherent rotation in a magnetic reversal in the “10x2” sample are given as well as the micromagnetic simulation of the same problem. The issue of the differing spatial resolution between experiment and simulation is addressed. The reversal is cast into a vectorial representation, showing the full power of the experimental micromagnetic techniques and the detailed experimental comparisons that are possible. Reversal results in other magnetic fields are shown to help give a systematic understanding of the problem. Data from other sample shapes are presented, showing coherent rotation is possible by merely changing geometry. Through simulation, reversal with different risetimes of transient magnetic fields are addressed, highlighting the dynamic nature of these reversals. Simulation results with different orientation of magnetic fields are presented. These too can dramatically effect reversal. Dramatic risetime differences are found by adding non-magnetic defects into the sample, further highlighting the range of possibility in magnetization reversal. As a test of these results, the 10 x 2 μm incoherent rotation simulation is repeated with smaller cells to give very similar results. This data is used to plot the various energy terms as a function of time during a reversal. This section shows the complexity of magnetization reversal, in that minor changes of many parameters can dramatically effect results. It also shows that despite these issues, good correspondence between experiment and simulation has now been achieved in some cases.

6. Thermal Fluctuations

The biggest assumption in any stroboscopic experiment such as a TR-SKEM experiment is that the dynamics are repeatable from event to event. Does this assumption hold in micromagnetics? The Landau-Lifshitz-Gilbert (LLG) theory as presented in chapter one is fully deterministic, but reality is not so simple. The largest reason for non-deterministic, non-repeatable behavior in micromagnetic systems is thermal fluctuation of the magnetization vectors within the sample. The experiments occur at room temperature, although this is far below the Curie temperature of permalloy (869 K), thermal energy is large enough to affect dynamics. In this chapter, we present the Fokker-Planck theory of thermal fluctuations and use it to calculate the statistical properties of fluctuating magnetization vectors necessary for micromagnetic simulation with thermal fluctuation of magnetization vectors taken into account. We show preliminary tests of the thermal fluctuation simulation code and show examples of stochastic behavior in simulation. Scaling behavior of the thermal code is discussed to show that it is not practical to run simulations that are larger than a couple of micrometers big. Unfortunately, no statistical analysis of thermal switching in a 10 x 2 μm sample is possible at this time.

6.1 Theory of Thermal Fluctuations

Thus far we have assumed that micromagnetic dynamics is purely deterministic. This is rarely true. The system is often not in equilibrium and rarely proceeds exactly as proscribed by the LLG equation along the least energy pathway. The magnetization vectors oscillate due to thermal energy. This fluctuation is orders of magnitude faster than the micromagnetic dynamical motion. Because of this, it can be treated as a stochastic noise term added into the LLG equation.

Stochastic activation is introduced as a thermal magnetic field $\mathbf{H}_{\mathbf{th}}$ which is added to the effective magnetic field. It accounts for all thermally driven interactions of the magnetization vector with phonons, conduction electrons, nuclear spins, etc. and, thus, has many degrees of freedom. These interactions can also be responsible for damping since these fluctuations of the magnetization vector can lead to magnetization energy being dissipated in the environment. This treatment of thermal fluctuations roughly follows Scholz.[83]

Since there are a large number of microscopic degrees of freedom in this mechanism, the thermal field can be assumed to be a Gaussian random process with zero mean.

$$\left\langle H_{th,i}(t) \right\rangle = 0 \tag{6.1}$$

This means that the thermal field on average vanishes in each direction. A much more involved calculation is required to calculate the variance of this distribution. We will assume that each Cartesian component of the thermal field is uncorrelated both in space and in time. On the time scale we are sampling the thermal field, this is likely a very good approximation. We can write the variance for now as

$$\left\langle H_{th,i}(t) H_{th,j}(t') \right\rangle = 2D\delta_{ij}\delta(t-t') \tag{6.2}$$

Here D is a constant that we have not yet determined. The Kronecker δ expresses the fact that different components of the thermal field are uncorrelated, and the Dirac δ shows the fact that the autocorrelation time of the thermal field is much shorter than the response time of the system, and, thus, it can be viewed as uncorrelated in time. Hence, this is a source of white noise.

6.1.1 Gaussian White Noise

Since it is assumed that thermal activation processes are of a much higher frequency then the sample response time (precession frequency of the magnetization vector), the fluctuating field used to simulate thermal activation is a stochastic process. Any stochastic process of zero mean with a two time covariance function given by

$$\left\langle \eta(t) \right\rangle = 0 \qquad \left\langle \eta(t)\eta(t+\tau) \right\rangle = \sigma^2\delta(\tau) \tag{6.3}$$

where η is the stochastic variable, is called Gaussian white noise. This is because the Fourier transform of the stationary two time covariance function is

$$F(\omega) = \int d\tau \langle \eta(t)\eta(t+\tau) \rangle e^{i\omega\tau} = \sigma^2 \qquad (6.4)$$

which is independent of frequency.

6.1.2 Stochastic Integrals

Integration of stochastic processes is somewhat mathematically complex. The theory is covered in books such as van Kampen and Gillespie.[84] As an example, let us consider a one dimensional stochastic differential equation with multiplicative noise. (This is a simplified version of the Langevin equation.)

$$\frac{dX(t)}{dt} = a(X(t),t) + b(X(t),t)\eta(t) \qquad (6.5)$$

Thus, the increment dX during a short time interval dt is given by

$$dX(t) = a(X(t),t)dt + \int_t^{t+dt} b(X(t'),t')\eta(t')dt' \qquad (6.6)$$

The second term is a stochastic integral and needs to be looked at in more detail. We can evaluate the integrand at the beginning of the interval [t, t+dt] and multiply it by the length of the interval dt and use this result as the increment for dX

However, we could also evaluate the integrand at any other time t+βdt in the interval [t,t+dt]. Hence β is on the interval [0,1]. Then the mean value of X is given by

$$\overline{X}(t) = (1-\beta)X(t) + \beta X(t+dt) = X(t) + \beta dX(t) \qquad (6.7)$$

In this general case dX is given by

$$dX(t) = a(\overline{X}(t),t')dt + b(X(t) + \alpha dX(t),t')\eta(t)\sqrt{dt} \qquad (6.8)$$

We can Taylor expand the second term to get dX(t)

$$dX(t) = \left[a(X(t),t) + \beta \frac{\partial b(X(t),t)}{\partial X} b(X(t),t)\eta^2(t) \right] dt + b(X(t),t)\eta(t)\sqrt{dt} \qquad (6.9)$$

Depending upon the choice of α we get different drift terms. If we set β=0 we get the Ito interpretation of the stochastic differential equation.

$$X(t) = a(X(t),t)dt + b(X(t),t)\eta(t)\sqrt{dt} \qquad (6.10)$$

For β=1/2 we get the Stratanovich interpretation.

$$X(t)=\left[a(X(t),t)+\frac{1}{2}\frac{\partial b(X(t),t)}{\partial X}b(X(t),t)\right]dt+b(X(t),t)\eta(t)\sqrt{dt}\quad(6.11)$$

Thus, we have to be careful to distinguish between the interpretation of a stochastic differential equation. Different versions can, in principle, give different dynamical properties. In this work, the Stratanovich interpretation is selected because it gives the appropriate noise properties. The white noise in our case is actually an idealization of a "colored" noise in which the two time covariance function is given by

$$\langle\eta(t)\eta(t+\tau)\rangle=\frac{\sigma^2}{2m}e^{-m|\tau|}\qquad(6.12)$$

with a short time constant 1/m.

The Wong-Zakai theorem [85] states that in the Stratanovich interpretation, as m → ∞ this colored noise becomes white. Therefore, in most physical applications, Stratanovich calculus is preferred.

This example with the Langevin equation is not a truly trivial example, as the LLG equation with thermal noise can be written as a form of the this equation. The stochastic LL equation (the Landau-Lifshitz version is used because it is easier to isolate the functions $A_i(\mathbf{M},t)$ and $B_{ik}(\mathbf{M},t)$ at the end of the derivation we return to LLG) is

$$\frac{d\mathbf{M}}{dt}=-\gamma'\mathbf{M}\times(\mathbf{H_{eff}}+\mathbf{H_{th}})-\frac{\alpha\gamma'}{M_s}\mathbf{M}\times(\mathbf{M}\times(\mathbf{H_{eff}}+\mathbf{H_{th}}))\quad(6.13)$$

This can be rewritten (in component form) as

$$\frac{dM_i}{dt}=A_i(\mathbf{M},t)+B_{ik}(\mathbf{M},t)H_{th,k}(t)\qquad(6.14)$$

where the functions $A_i(\mathbf{M},t)$ and $B_{ik}(\mathbf{M},t)$ are defined as

$$A_i(\mathbf{M},t)=\left[-\gamma'\mathbf{M}\times\mathbf{H_{eff}}-\frac{\alpha\gamma'}{M_s}\mathbf{M}\times(\mathbf{M}\times\mathbf{H_{eff}})\right]_i\qquad(6.15)$$

$$B_{ik}(\mathbf{M},t)=-\gamma'\varepsilon_{ijk}M_j-\frac{\alpha\gamma'}{M_s}(M_iM_k-\delta_{ik}M^2)$$

where we are using the Einstein summation convention and ε_{ijk} is the Levi-Civita symbol. Thus we have written the stochastic LLG equation as the general form of a system of Langevin equations.

6.1.3 Fokker-Planck Equation

The Fokker-Planck equation describes the non-equilibrium probability distribution P(**M**,t) of a set of Langevin equations. It is one method to obtain the variance of the thermal fluctuations required for micromagnetic simulation. In the Stratanovich interpretation the Fokker-Planck equation is given by

$$\frac{\partial P}{\partial t} = -\frac{\partial}{\partial M_i}\left[\left(A_i + DB_{jk}\frac{\partial B_{ik}}{\partial M_j}\right)P\right] + \frac{\partial^2}{\partial M_i \partial M_j}\left[\left(DB_{ik}B_{jk}\right)P\right] \qquad (6.16)$$

Any probability distribution calculated will have to be normalized by the requirement that $\int P dt = 1$.

We can transform eqn 6.16 into a continuity equation to get

$$\frac{\partial P}{\partial t} = -\frac{\partial}{\partial M_i}\left[\left(A_i + DB_{ik}\frac{\partial B_{jk}}{\partial M_j} - DB_{ik}B_{jk}\frac{\partial}{\partial M_j}\right)P\right] \qquad (6.17)$$

Substituing the results from the stochastic LLG equation (eqn 6.15) we find

$$\frac{\partial B_{ik}}{\partial M_j} = -\gamma'\varepsilon_{ijk} - \frac{\alpha\gamma'}{M_s}\left(\delta_{ij}M_k + \delta_{jk}M_i - 2\delta_{ik}M_j\right) = -\frac{\alpha\gamma'}{M_s}2M_k \qquad (6.18)$$

and

$$B_{ik}\frac{\partial B_{jk}}{\partial M_j} = \left[-\gamma'\varepsilon_{ijk}M_j + \frac{\alpha\gamma'}{M_s}\left(M_iM_k - \partial_{ik}M^2\right)\right]\left(-\frac{2\alpha\gamma' M_k}{M_s}\right) = 0 \quad (6.19)$$

Thus the second term on the right hand side of the equation is zero. The third term is

$$B_{ik}B_{jk}\frac{\partial P}{\partial M_j} = \gamma'^2\left[-\varepsilon_{ilk}M_l - \frac{\alpha}{M_s}\left(M_iM_k - \delta_{ik}M^2\right)\right] \qquad (6.20)$$

$$\left[-\varepsilon_{jpk}M_p - \frac{\alpha}{M_s}\left(M_jM_k - \delta_{jk}M^2\right)\right]\frac{\partial P}{\partial Mj}$$

$$= \gamma'^2\left(\alpha^2 + 1\right)\left[\mathbf{M}\times\left(\mathbf{M}\times\frac{\partial P}{\partial Mj}\right)\right]_i$$

Thus our version of the Fokker-Planck equation is

$$\frac{\partial P}{\partial t} = -\frac{\partial}{\partial \mathbf{M}} \bullet \left\{ \begin{bmatrix} -\gamma \mathbf{M} \times \mathbf{H_{eff}} - \frac{\alpha\gamma'}{M_s} \mathbf{M} \times \left(\mathbf{M} \times \mathbf{H_{eff}} \right) - \\ D\gamma'^2 (1+\alpha^2) \mathbf{M} \times \left(\mathbf{M} \times \frac{\partial}{\partial \mathbf{M}} \right) \end{bmatrix} P \right\} \quad (6.21)$$

The first two terms are dynamical terms from the original LLG equation and the third is an additional term due to thermal fluctuations. We will only look at this term for now.

$$\frac{\partial P}{\partial t} = \frac{\partial}{\partial \mathbf{M}} \bullet D\gamma'^2 (1+\alpha^2) \mathbf{M} \times \left(\mathbf{M} \times \frac{\partial}{\partial \mathbf{M}} \right) P \quad (6.22)$$

After a vector identity this is

$$\frac{\partial P}{\partial t} = \frac{\partial}{\partial \mathbf{M}} \bullet D\gamma'^2 \left(1+\alpha^2\right) \mathbf{M} \times \left(\mathbf{M} \times \frac{\partial}{\partial \mathbf{M}} \right) P - \nabla^{\mathbf{2}} \left(D\gamma'^2 \left(1+\alpha^2\right) M^2 P \right) \quad (6.23)$$

In the case that the sample is in equilibrium except for thermal fluctuations, **M** is nearly constant. Therefore, even though P is a function of **M**, it can be assumed to be roughly constant for fluctuations near equilibrium. Thus the equation simplifies to

$$\frac{\partial P}{\partial t} = -2D\gamma'^2 \left(1+\alpha^2\right) P \quad (6.24)$$

The solution to this equation is

$$P = Ce^{-2D\gamma'^2 (1+\alpha^2) t} \quad (6.25)$$

and we have an exponential with a time constant (called the Neel time).

$$t_N = \frac{1}{2D\gamma'^2 (1+\alpha^2)} \quad (6.26)$$

We must ensure that the stationary properties of the stochastic LLG equation and the statistical properties of the thermal field coincide with the appropriate properties in thermal equilibrium. We must have the stationary state solution of the Fokker-Planck equation correspond to the Boltzmann distribution.

$$P(M) = P_o e^{-\frac{MH_{eff} V}{kT}} \quad (6.27)$$

So we can get

$$\frac{\partial P}{\partial M} = -\frac{H_{eff}V}{kT}P \tag{6.28}$$

We need to look at the stationary Fokker-Planck equation

$$0 = \frac{\partial}{\partial \mathbf{M}} \bullet \left\{ \begin{bmatrix} (\gamma' \mathbf{M} \times \mathbf{H}_{\mathbf{eff}}) - \frac{\alpha\gamma'}{M_s} \mathbf{M} \times (\mathbf{M} \times \mathbf{H}_{\mathbf{eff}}) P + \\ \frac{D\gamma'^2 V(1+\alpha^2)}{kT} \mathbf{M} \times (\mathbf{M} \times \mathbf{H}_{\mathbf{eff}}) \end{bmatrix} P \right\} \tag{6.29}$$

We can look at the first term in this equation as

$$\frac{\partial}{\partial \mathbf{M}} \bullet (\gamma' \mathbf{M} \times \mathbf{H}_{\mathbf{eff}}) = -\frac{\gamma' kT}{PV} \frac{\partial}{\partial \mathbf{M}} \bullet \left(\mathbf{M} \times \frac{\partial P}{\partial \mathbf{M}} \right) \tag{6.30}$$

One component of the vector triple product is

$$\left[\frac{\partial}{\partial \mathbf{M}} \bullet \left(\mathbf{M} \times \frac{\partial P}{\partial \mathbf{M}} \right) \right]_i = \partial_{M_i} \left(\varepsilon_{ijk} M_j \partial_{M_k} P \right) = 0 \tag{6.31}$$

Thus, this term is zero, so the Fokker-Planck equation with the stationary solution becomes

$$0 = -\frac{\alpha\gamma'}{M_s} \mathbf{M} \times (\mathbf{M} \times \mathbf{H}_{\mathbf{eff}}) P + \frac{D\gamma'^2 V(1+\alpha^2)}{kT} \mathbf{M} \times (\mathbf{M} \times \mathbf{H}_{\mathbf{eff}}) P \tag{6.32}$$

Hence, the coefficients must be equal.

$$\frac{\alpha\gamma'}{M_s} = \frac{D\gamma'^2 V(1+\alpha^2)}{kT} \tag{6.33}$$

Hence we get

$$D = \frac{\alpha kT}{\gamma' V M_s (1+\alpha^2)} \tag{6.34}$$

Recalling the definition of γ' (Thus, we return to the LLG equation.), this is

$$D = \frac{\alpha KT}{\gamma V M_s} \tag{6.35}$$

So the correlation of the thermal field is thus

$$\left\langle H_{th,i}(t) H_{th,j}(t') \right\rangle = 2\frac{\alpha KT}{\gamma V M_s} \delta_{ij} \delta(t - t') \tag{6.36}$$

This result could also be obtained from the fluctuation dissipation theorem.[86] Therefore, we now have the variance in the thermal field.

6.2 Preliminary runs of Thermal Code

The first thing to do with thermal code is to devise a test to ensure that it is working properly. The main problem is that thermal fluctuations introduce a stochastic element into the simulation and thus can only be tested statistically. Therefore, several events are necessary, with statistical properties being checked. One test that will give some idea of how well the code performs is to compare its results to those predicted by the Arrhenius-Neel Law. This law is simple.[87] It states that for a particular small sample the magnetization will fluctuate around an energy minimum. From time to time reversal processes will occur when the magnetization crosses the energy barrier and switches to the other energy minimum. The probability per unit time that the magnetization jumps over the energy barrier in thermal equilibrium is given by the Boltzmann distribution and is proportional to:

$$\exp\left(-\frac{E}{k_B T}\right) \tag{6.37}$$

If we consider a single energy barrier model in a square sample (thus only crystalline anisotropy creates the energy barrier), then the reciprocal of the switching probability is the relaxation time τ and can be written in the form of the Arrhenius-Neel law

$$\frac{1}{\tau} = f_o \exp\left(-\frac{KV}{k_B T}\right) \tag{6.38}$$

where f_o is a characteristic dynamic frequency which is a material parameter.

The only barrier to thermal switching comes from the sample's induced anisotropy magnetic field. In order to make the number of thermal switching events manageable, it is necessary to increase the anisotropy magnetic field of the sample from its experimental value of 8.6 Oe (in our permalloy), by a factor of ten, to 86 Oe. This makes the energy barrier more significant, thus reducing the number of switching events. With lower anisotropy, the sample switches so frequently that it is almost always switching. Then the time spent in either the switched or unswitched state is only dependent upon the gyromagnetic properties of the sample, as it would be continuously switching. The sample for this trial is chosen to be a square sample, so as to remove shape anisotropy. It is 32 x 32 nm and 4 nm thick. It is broken up into a grid of 8 x 8 cubic cells. The sample is in zero external field and left only to thermal fluctuations at 300 K to provide dynamic motion. It will have two metastable equilibria. One with magnetization directed along

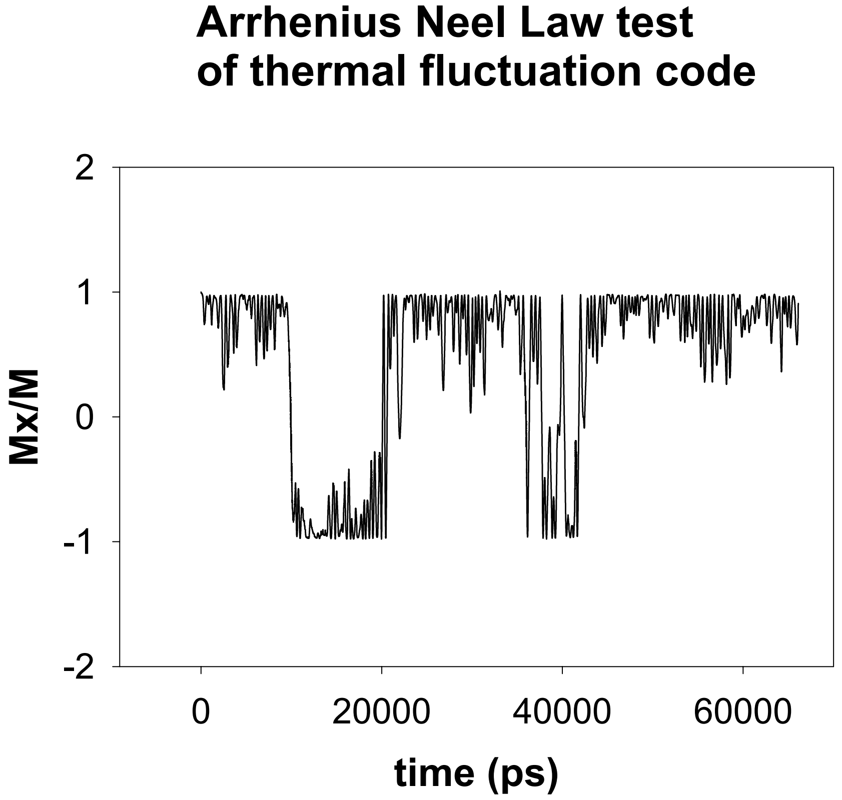

Figure 6.1 Arrhenius-Neel test of thermal fluctuation code. 32 x 32 nm sample is at 300 K with no external field is left to switch thermally to test the stochastic nature of switching in the micromagnetic code.

the positive easy axis (x axis) and one with magnetization directed along the negative easy axis (- x axis). It will randomly switch back and forth between these states according to the Arrhenius-Neel Law. A plot of such a run is shown in Fig. 6.1.

In order to analyse this plot, one must define what it means to "switch". In this section, a switch will be defined as any time that the sample goes from a value of $M_x/M = 0.75$ to $M_x/M=-0.75$ or vice versa. This removes from consideration times when a sample may partially switch, but return to its initial equilibrium without completing a full switch. By this switching definition, there are 10 switching events in this simulation. It is interesting that many of the switching events happen in relatively quick succession after one another. Presumably, these are times when the sample has lots of excess energy which has not yet had time to be damped from the system. There is an average of 6620 ps spent in either the switched or unswitched state in between switching events in this simulation. Sticking this value in eqn. 6.38, f_o is found to be $2.5 * 10^{11}$ 1/s. This value compares well with the values in Scholz [82].

6.3 Magnetization Reversal with Thermal Fluctuations

In order to test the effects that thermal fluctuations can have in a magnetization reversal, a simulation can be run upon a case where there is high metastability because driving fields barely exceed coercivity. One such situation is the case of a 1 μm x 200

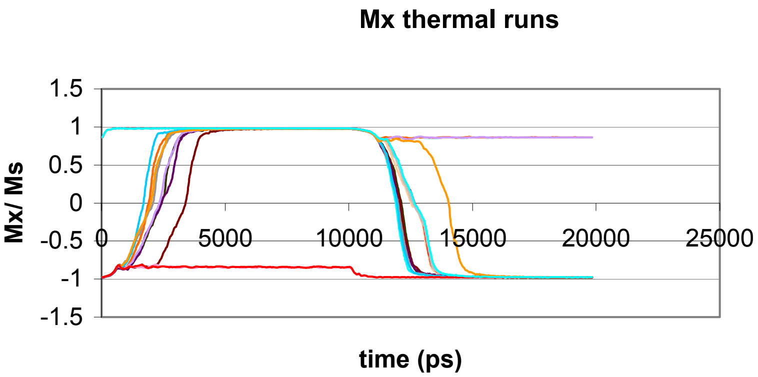

Figure 6.2 16 magnetization reversal with thermal fluctuation runs at 300 K. Sample is 1000 x 200 x 15 nm. Sometimes sample switches, and sometimes it doesn't. Sometimes sample switches back, and sometimes it doesn't. Sometimes it starts from an already switched state. Even when it does switch, there is a wide range in switching times.

nm x 15 nm permalloy sample broken up into 64 x 16 cells in a two dimensional simulation. The sample is in a 300 Oe DC magnetic field, with a 580 Oe antiparallel transient switching field. A plot of 16 runs under these conditions is shown in Fig. 6.2.

A wide range of switching behaviours is seen. Sometimes the sample switches under the transient pulse; sometimes it does not. Sometimes it switches back when the transient pulse ends; other times it does not. Sometimes it begins in an unswitched state, because it had not switched back on the previous pulse. Even when the sample does switch, the time it takes to switch may be widely varied from one event to the next. This trial shows how important thermal fluctuations can be when the sample is in a highly metastable situation. If we average these runs, and the associated spatial images, we see what would theoretically be seen in a TR-SKEM experiment, if thermal fluctuation is the only source of non-repetitive motion. An average of these runs is shown in Fig. 6.3.

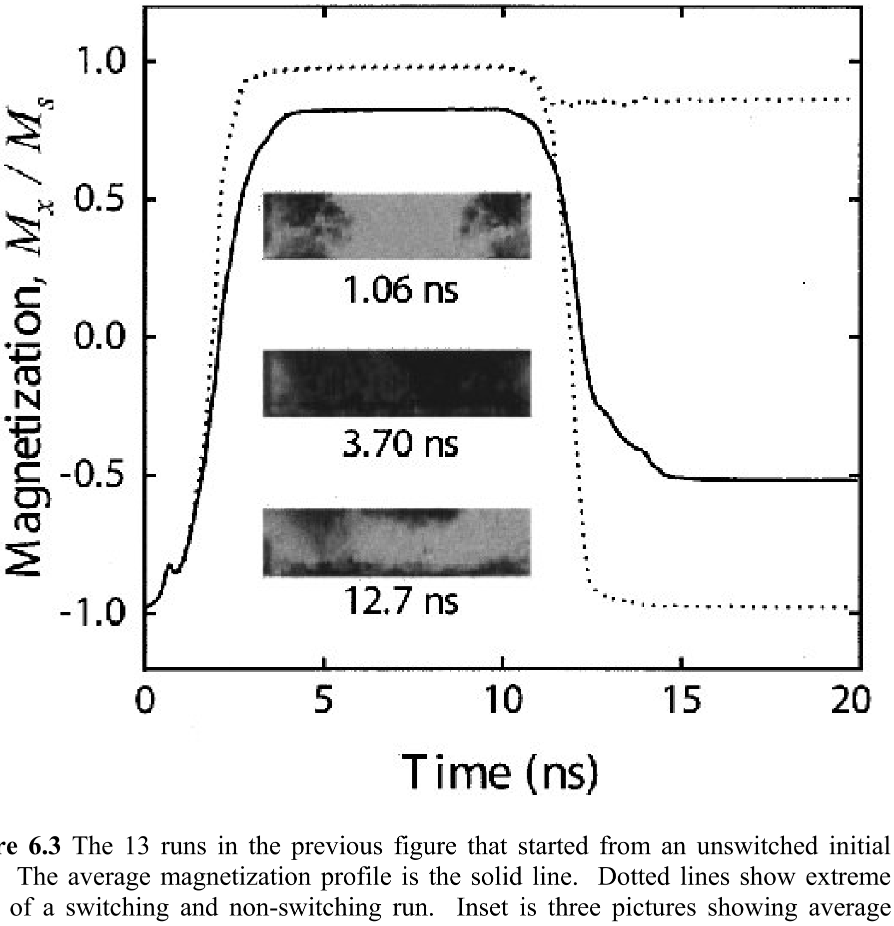

Figure 6.3 The 13 runs in the previous figure that started from an unswitched initial state. The average magnetization profile is the solid line. Dotted lines show extreme cases of a switching and non-switching run. Inset is three pictures showing average spatial images. Features are not as sharp due to stochastic averaging. This causes an apparent drop in spatial resolution.

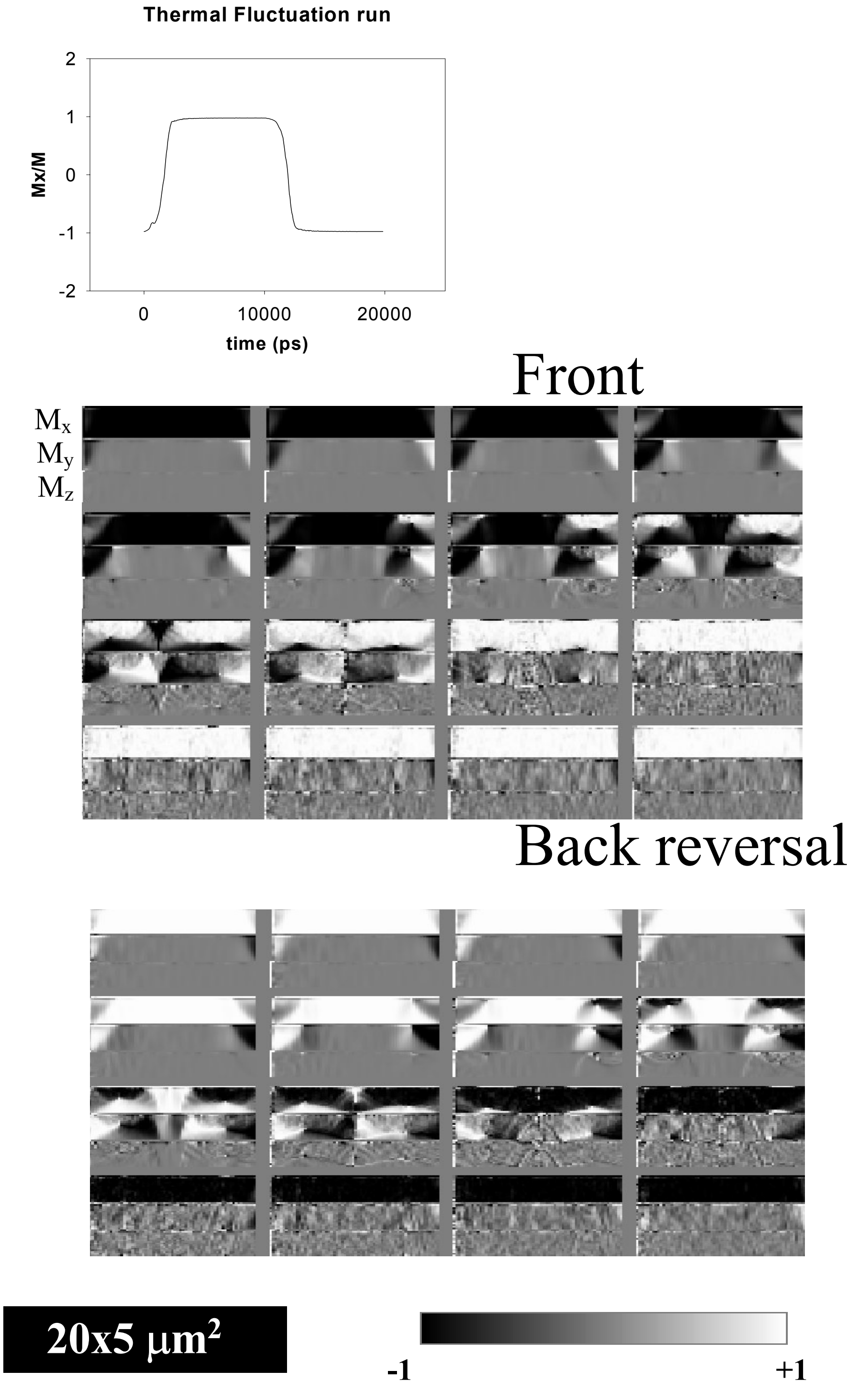

Figure 6.4 Reversal in a 1 μm x 200 nm sample with thermal fluctuations. Symmetry is broken, but there is still evidence of a stripelike instability and incoherent rotation.

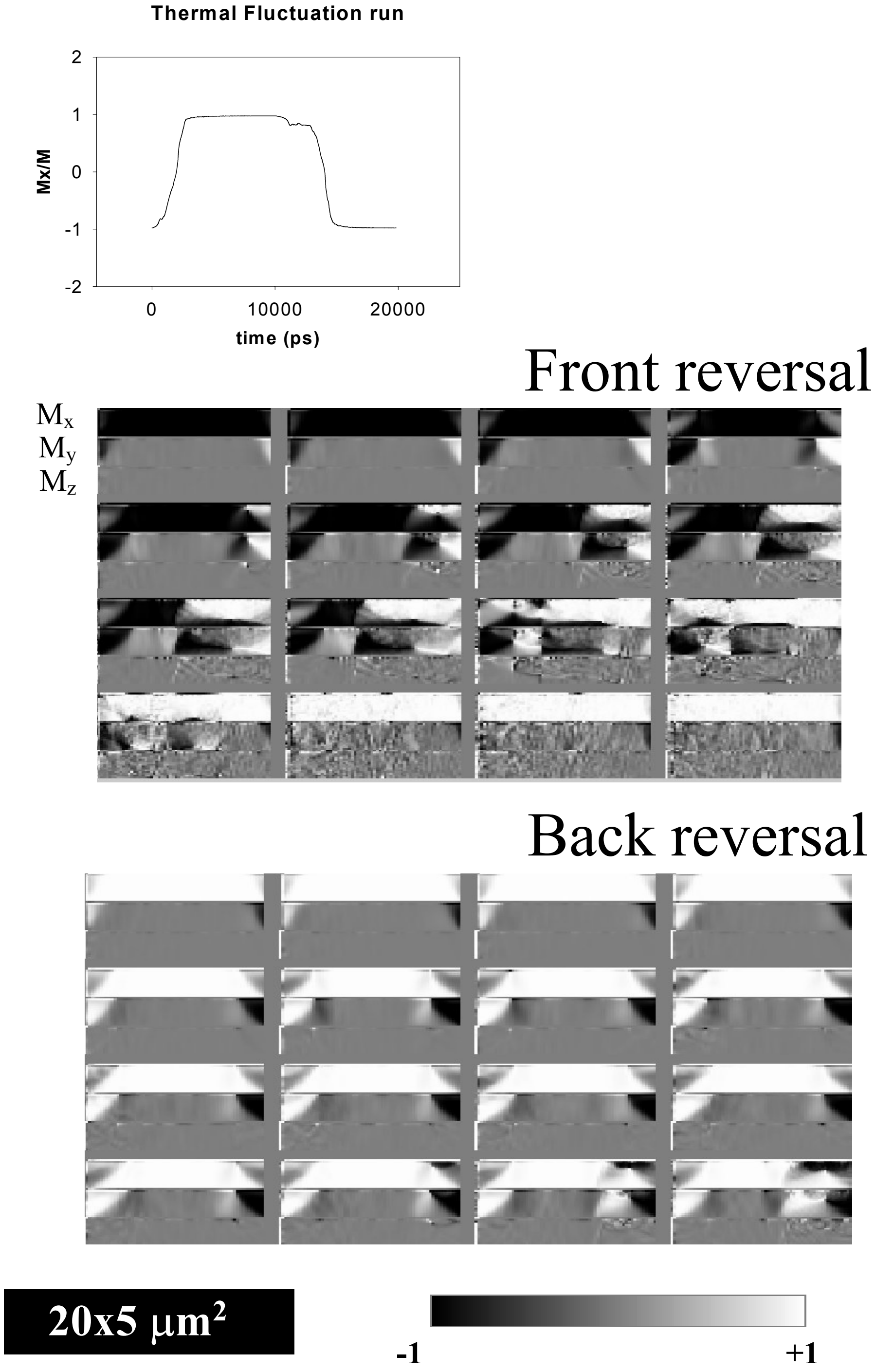

Figure 6.5 Reversal in a 1 μm x 200 nm sample with thermal fluctuations. Symmetry is broken, but there is still evidence of a stripelike instability and incoherent rotation. In this case, the back reversal nucleation is significantly delayed.

Thermal fluctuations serve to increase the switching time of a stochastic average over that of a single event. They serve to reduce the change in magnetization observed, if the sample remains unswitched on occasion. They cause an apparent reduction in spatial resolution in spatial images because what is imaged is an average of several different reversals.

In order to get an idea of what variation may occur in different reversals where thermal fluctuations dominate, a couple of these thermal runs are presented. In Fig. 6.4, one reversal is shown. In this reversal, the sample switches and switches back reasonably quickly. This reversal is less symmetric than those presented before. The domain on the right grows faster than the domain on the left in this case. In this run, thermal fluctuations may be evident, although there is still evidence of a dynamic domain reversal.

In Fig. 6.5, another run with thermal fluctuations is shown. The major difference between these reversals is that the back reversal is much slower to nucleate. It is only beginning to switch, at the time when the previous switch was completed.

These examples show that in certain circumstances, thermal fluctuations can make a huge difference in the magnetization reversal. In these cases, stroboscopic experiments will not be particularly fruitful. Stroboscopic experiments work best in the repetitive, deterministic reversals where thermal fluctuations are smaller. These are the cases where the coercivity of the sample is exceeded significantly by the driving magnetic field.

6.4 Prospects for a “10x2” Thermal Fluctuation run

All runs with thermal fluctuations shown in this thesis are on samples much smaller than the “10x2” sample which has been shown in much of this thesis. This is because, at this point, it is not possible for one run on a 10 x 2 μm sample to conclude in any reasonable amount of time. To gather any information about the effect of thermal fluctuations on a sample, many runs are needed to determine an average effect. The runs on a 1 μm x 200 nm sample took approximately three days each to run. They had 64 x 16 cells. In order to scale up to 512 x128 cells, an increase by 64 times the total number of cells in the simulation, keeping cells the same size, one would expect the run to take 512

(!) times as long. This is likely an underestimate because returning to the cell size used in the previous “10x2” simulations would mean there would be larger cells. Increasing cell size may lead to the simulation departing from a physically meaningful situation. If this is not a problem increasing cell size will lead to a decrease is the possible time steps that can be taken throughout the simulation because the random thermal fluctuations in each cell will be larger due to its increasing size. This problem may be avoidable by running a simulation in a situation where other terms (such as Zeeman energy) drive the dynamics. There is little point to this because one would be studying thermal fluctuations in a region where thermal fluctuations are often negligible. In order to have meaningful experimental comparison with thermal fluctuation micromagnetic simulation, it is necessary to have smaller samples (on the order of 1 μm x 200 nm). This leads to a loss of resolution in TR-SKEM experiments, so this remains an unresolved problem.

6.5 Summary of the Chapter

In this chapter, the theory of thermal fluctuations is introduced. After discussing stochastic integrals, a Fokker-Planck equation is introduced, which leads to a variance in the distribution of thermal fluctuations that can be incorporated into simulation. Initial tests are done to see that this code corresponds with the Arrhenius-Neel law. Runs are done with a smaller sample than those used in experiment to understand the effect of thermal fluctuation upon magnetization reversal. Runs with a larger sample cannot be done at this point, as they would take too long to run. A discussion of why this is and how long such a run might take concludes this chapter.

7. Summary and Future Prospects

7.1 Conclusion of this work

In this thesis, some of the initial work using a time-resolved scanning Kerr effect microscopy (TR-SKEM) system is presented. Data in both ferromagnetic resonance and magnetization reversal experiments are presented. Micromagnetic simulation results are compared to these experiments, showing very good agreement. This has allowed for a considerable understanding of micromagnetic dynamics processes in the time domain.

In chapter one, the background theory required to understand this thesis is introduced. The context surrounding this work in light of historical developments and contemporary work is discussed.

Chapter two outlines the experimental technique of TR-SKEM. Combining the sub-micrometer resolution of scanning optical microscopy and the picosecond temporal resolution of ultrafast laser optics, this technique is able to provide much information about micromagnetic dynamics that has previously been too fast to image.

Chapter three outlines the micromagnetic simulation details. It explains the technique of solving the Landau-Lifshitz-Gilbert equation with a finite element simulation and the numerical issues surrounding it. It gives an overview of the micromagnetic simulation code used in this thesis. It gives a broader context of micromagnetic simulations, introducing other techniques used to simulate similar magnetic dynamic problems. Finally, it explains the standard problem run to prove that our code is correct with complete simulation data presentation.

Chapter four outlines the ferromagnetic resonance problem, a low angle micromagnetic dynamic excitation, and presents TR-SKEM data. Simulations of this data are provided showing good agreement, with a discussion of the issues surrounding these simulations.

Chapter five outlines the magnetization reversal problem, a high angle micromagnetic dynamic excitation, and presents TR-SKEM data. Various methods of reversal are observed. This is followed with simulation of these results. Further simulation of magnetic reversal problems shows that possible dynamic behaviour is very rich. Large changes in reversal can be observed by making small changes to the sample or its set-up.

Chapter six discusses the problem of thermal fluctuation of the magnetization vector. It addresses how this problem can be tackled in simulation. Runs of simulated reversals with thermal fluctuations on small samples are provided to give an idea of what effect they can have. A discussion is presented of why simulations with thermal fluctuations of the larger samples shown earlier in the thesis is not possible. It is possible to get an idea of what effect thermal fluctuations have in experimental data, and many of these effects are seen.

This work shows that TR-SKEM magnetization dynamics experiments can be understood with a time domain LLG simulation. Good agreement can be obtained in both low angle ferromagnetic resonance excitations and in higher angle magnetization reversal experiments. The magnetization reversal experiments are the more complex problem and lead to hints of where this comparison may break down. This is addressed partially by studying thermal fluctuation of the magnetization vector.

The most significant point to this work is the beginning of a convergence between experimental and simulated micromagnetic dynamics. More work needs to be done to come to a full convergence, but this process has begun. This process will lead to a much better understanding of micromagnetics.

7.2 Future Work

Future possibilities to extend this research include the following. The technique of TR-SKEM can be advanced; other microscopy techniques can be time resolved to give better spatial resolution; other problems can be looked at experimentally; other problems can be simulated, and the micromagnetic simulation code can be advanced. The strategy of using simulation in tandem with experiment to understand the problem is a good one.

Advances to the TR-SKEM technique would include increasing spatial resolution by using near field optics. Oil immersion and solid immersion lenses [88] are two relatively easy additions to increase spatial resolution. Another method is to decrease the wavelength of the light by frequency doubling the laser, although this makes optics a problem, as most standard optics are not transparent in the ultraviolet. Using a coated fibre, as in a near field optical microscope [89] to increase spatial resolution is probably not possible since it will significantly increase the time required to gather a signal. Detection schemes can be improved, in part by using photomultiplier tubes, as it will increase sensitivity and allow for a better range of frequency of light that can be used. Another issue of concern is reducing the number of events that have to be averaged to build up a stroboscopic signal. This will limit the effect of stochastic processes in individual images and allow for a better understanding of them. Stroboscopic noise imaging [90] is one step along that direction.

Other microscopy techniques can be time resolved leading to the possibility of observing magnetization dynamics in other situations. These include ultrafast, stroboscopic x-ray techniques [91] which allow for magnetic detection using circular dichroism [92] and photoemission electron microscopy.[93] Using electrons for detection, one can use stroboscopic electron beam tomography,[94] ballistic electron magnetic microscopy,[42] scanning electron microscopy with polarization analysis [95] and spin-polarized scanning tunneling microscopy.[96]

New problems exist that can be looked at in experiment. Magnetic reversals with patterned defects, varying magnetic field rise times, and canting of the reversal magnetic field with respect to the DC magnetic field can be explored. Local sample excitation using, for example, a magnetic recording head to launch spin waves can be done. This work can be expanded to use other materials, as long as coercive fields can be overcome to cause switching. Experimentally, more industrially relevant structures can be looked at including magnetic multilayers, Hall cross devices and magnetic recording heads.[97]

In simulation, many of these above problems can also be looked into. As well, it will be fruitful to continue to speed up the micromagnetics code. It still does not scale well as more processors are added. It may be fruitful to try using an adaptive cell size,[62] so that only regions of highly changing magnetization use small cells, but this requires completely changing the demagnetizing field calculation method. In order to improve the comparison between simulation and experiment, smaller samples are needed in order to allow more complex simulations that take into account effects such as polycrystallinity and thermal fluctuations. However, spatial resolution needs to be improved to handle this in experiment. Thus a tandem approach of improving the experimental apparatus along with the simulation is needed. A further tandem effort can be carried out in the spin wave domain. It is probably going to be a harder effort to get the higher frequency spatiotemporal features imaged and simulated. This work suceeded with the larger features. Ideally, there will come a time when this comparison can definitively show a breakdown of the LLG theory and provide insight into what physics is needed beyond it. This will lead to a definitive test of the damping function in micromagnetic dynamics. Micromagnetics will grow beyond its existing phenomenological framework. Exactly how to go beyond LLG in mesoscale magnetic systems is a hot topic of interest in both industry and academia today.

Bibliography

[1] http://www-3.ibm.com/chips/bluelogic/manufacturing/makechip/ is a good summary of microelectronics
[2] October 2001 Physics Today is a good introduction to nanoelectronics
[3] Special Issue on Magnetoelectronics, Phys. Today **48** (4), 24-63 (1995).
* The Special 200th Issue of JMMM had invited articles *to "assess the present state of magnetism and magnetic materials and discuss its future prospects*" (from preface (Magnetism beyond 2000) by A. J. Freeman and S. D. Bader
[4] The disovery of GMR:

S. S. P. Parkin, Giant magnetoresistance and oscillatory interlayer coupling in polycrystalline transition metal multilayers," Section in *Ultrathin Magnetic Structures II*, Edited by B. Heinrich and J. A. C. Bland, Springer Verlag, Berlin, Heidelberg (1994).

New Scientist magazine, vol 149 issue 2016, 10/02/1996, page 34, "Giants in their field".

M. N. Baibich, J. M. Broto, A. Fert, F. Nguyen Van Dau, F. Petroff, P. Eitenne, G. Creuzet, A. Friederich, and J. Chazelas, Giant magnetoresistance of (001)Fe/(001)Cr magnetic superlattices," Phys. Rev. Lett. **61** (21), 2472-2475 (1988).

P. Grünberg, R. Schreiber, Y. Pang, M. B. Brodsky, and H. Sowers, "Layered magnetic structures: evidence for antiferromagnetic coupling of Fe layers across Cr interlayers," Phys. Rev. Lett. **57** (19), 2442-2445 (1986).

[5] J. Fontcuberta, Colossal magnetoresistance," Phys. World, February 1999, 33-38 (1999).

S. Jin, T. H. Tiefel, M. McCormack, R. A. Fastnacht, R. Ramesh, and L. H. Chen, "Thousandfold change in resistivity in magnetoresistive La-Ca-Mn-O films," Science **264**, 413-415 (1993).

R. von Helmolt, J. Wecker, B. Holzapfel, L. Schultz, and K. Samwer, "Giant negative magnetoresistance in perovskitelike $La_{2/3}Ba_{1/3}MnO_x$ ferromagnetic films," Phys. Rev. Lett. **71** (14), 2331-2333 (1993).

[6] Special issue of IBM Journal of Research and Development. Vol 42, No. 1, 1998, GMR, oscillatory coupling and related studies.

Ultrathin Magnetic Structures II, Edited by B. Heinrich and J. A. C. Bland, Springer Verlag, Berlin, Heidelberg (1994).

[7] P. Ball, "Meet the spin doctors… (news feature)," Nature **404**, 918-920 (2000).

M. Johnson, "Magnetoelectronic memories last and last…" IEEE Spectrum, February 2000, 33-40 (2000).

G. A. Prinz, "Magnetoelectronics applications," J. Magn. Magn. Mater. (Special 200th Issue*) **200**, 57-68 (1999).

J. de Boeck and G. Borghs, "Magnetoelectronics," Phys. World, April 1999, 27-32 (1999).

G. A. Prinz, "Magnetoelectronics," Science **282**, 1660-1663 (1998).

J. L. Simmonds, "Magnetoelctronics today and tomorrow," Phys. Today **48** (4), 26-32 (1995).

[8] N. Bohr, Ph.D thesis 1911 Copenhagen

J. H. van Leeuwen, Ph.D thesis 1919 Leiden

good derivation in A. Aharoni, *Introduction to the theory of ferromagnetism*, Oxford University Press Inc., New York, 1996.

[9] R. Fiederling , M. Keim, G. Reuscher, W. Ossau, G. Schmidt, A. Waag, L. W. Molenkamp, "Injection and detection of a spin-polarized current in a light-emitting diode," Nature **402**, 787-790 (1999).

Y. Ohno, D. K. Young, B. Beschoten, F. Matsukara, H. Ohno, and D. D. Awschalom, "Electrical spin injection in a ferromagnetic semicondcutor heterostructure," Nature **402**, 790-792 (1999).

P. R. Hammar, B. R. Bennet, M. J. Yang, and M. Johnson, "Observation of spin injection at a ferromagnet-semiconductor interface," Phys. Rev. Lett. **83** (1), 203-206 (1999).

[10] D. D. Awschalom and J. M. Kikkawa, "Electron spin and optical coherence in semiconductors," Phys. Today, **52**, 33-38 (1999).

J. M. Kikkawa and D. D. Awschalom, "Lateral drag of spin coherence in gallium arsenide," Nature **397**, 139-141 (1999).

[11] D. P. DiVincenzo, "Quantum computation," Science **270**, 255-261 (1995).

[12] Good reviews and discussions of contemporary (at least, public) magnetic recording issues can be found on IBM's Storage Systems and Technology and Recording Head Technology web site:

---

www.almaden.ibm.com/sst/ and several links can also be found on "Magnetic Recording Websites" at www.wsrcc.com/alison/magrec.html.

[13] Toshiba announces this at http://maccentral.macworld.com/news0204/09.toshiba.php

[14] M. Johnson, "The all-metal spin transistor," IEEE Spectrum, **31** (5), 47-51 (1994).

S. Datta, and B. Das, "Electronic analog of the elctro-optic modulator," Appl. Phys. Lett **56** (7), 665-667 (1990).

M. Johnson and R. H. Silsbee, Phys. Rev. Lett. **55**, 1790-1793 (1985).

[15] P. Weiss, "L'hypothese du champ moleculaire et la propriete ferromagnetique." J. de Phys. Rad. **6**, 661-690 (*The hypothesis of the molecular field and the property of ferromagnetism)*

good review in C. Kittel, *Introduction to Solid State Physics: Sixth Edition,* John Wiley and Sons Inc., New York (1986).

[16] T. L. Gilbert, "A Lagrangian formulation of the gyromagnetic equation of the magnetization field," Phys. Rev. **100**, 1243 (1955).

[17] L. D. Landau and E. Lifshitz, "On the theory of the dispersion of magnetic permeability in ferromagnetic bodies," Phys. Z. Sowjetunion **8**, 153-169 (1935).

[18] J.C.Mallinson, "On damped gyromagnetic precession," IEEE Trans. Magn. **23**, 2003-2004 (1987).

[19] M. Cyrot, ed., *Magnetism of Metals and alloys,* North Holland, Amsterdam (1982).

[20] W. Heisenberg, Z. Physik **49**, 619 (1928).

[21] W. D. Doyle, S. Stinnett, C. Dawson, and L. He, "Magnetization reversal at high speed – an old problem in a new context," J. Magn. Soc. Jpn. **22**, 91-106 (1998).

[22] W. K. Hiebert, "Experimental Micromagnetic Dynamics: Ultrafast Magnetization Reversal Using Time Resolved Scanning Kerr Effect Microscopy," PhD thesis, University of Alberta, Canada, 2001.

[23] W. F. Brown, Jr., "Criterion for uniform micromagnetization," Phys. Rev. **105**, 1479-1482 (1957).

E. H. Frei, S. Strikman, D. Treves, "Critical size and nucleation of ideal ferromagnetic particles," Phys. Rev. **106**, 446-455 (1957).

[24] A. Aharoni, *Introduction to the theory of ferromagnetism*, Oxford University Press Inc., New York, 1996.

[25] K. J. Sixtus and L. Tonks, "Propagation of large Barkhausen discontinuities," Phys. Rev. **37**, 930-958 (1931).

[26] W. Döring, "Über die Trägheit der Wände zwischen Weiβscehn Bezirken," Z. Natuforshung **3a**, 373-379 (1948) (*On the inertia of walls between Weiss domains)*.

[27] L. R. Walker, Bell Telephone Laboritories Memorandum, 1956 (unpublished). An account of this work is found in J. F. Dillon Jr., Magnetism, Vol. III, edited by G. T. Rado and H. Suhl (Academic, New York, 1963)

[28] E. C. Stoner and E. P. Wohlfarth, Phil. Trans. Roy. Soc. **A240**, 599 (1948).

[28] J. C. Anderson, *Magnetism and Magnetic Materials*, Chapman and Hall Ltd., London, 1968.

[30] D. O. Smith, "Static and dynamic behaviour of thin permalloy films", JAP **29** (3), 264 (1958).

[31] E. M. Gyorgy, JAP **28**, 1011 (1958).

[32] D. D. Stancil, *Theory of Magnetostatic Waves*, Springer-Verlag (1993).

[33] L. R. Walker, Phys. Rev. **105**, 390 (1957).

L. R. Walker, J. Appl. Phys. **29**, 318 (1958).

[34] R. W. Damon and J. R. Eschbach, J. Phys. Chem. Solids **19**, 308-320 (1961).

[35] R. M. White, *Quantum Theory of Magnetism*, Springer-Verlag, Berlin, 1983.

[36] T. Holstein and H. Primakoff, Phys. Rev. **58**, 1098 (1940).

[37] C. Kittel, Phys. Rev. **73**, 155 (1948).

[38] B. E. Storey, A. O. Tooke, A. P. Cracknell, and J. A. Przystawa, "Magnetostatic modes in thin films of YIG," J. Phys. C **10**, 875 (1977).

[39] P. H. Bryant, J. F. Smyth, S. Schultz and D. R. Fredkin, "Magnetostatic mode spectrum of rectangular ferromagnetic particles," Phys. Rev. B., **47** (17), 11255 (1994)

[40] A. Hubert, R. Schäfer, *Magnetic Domains: The Analysis of Magnetic Microstructures*, Springer, 1998.

[41] H. W. Fuller and M. E. Hale, JAP **31**, 238 (1960).

H. Hoffmann, "Theory of magnetization ripple," IEEE Trans. Mag. **4**, 32-38 (1968).

[42] W. H. Rippard and R. A. Buhrman, "Ballistic electron magnetic microscopy: imaging magnetic domains with nanometer resolution," Appl. Phys. Lett., **75**, 1001-1003 (1999)

---

[43] J. Pollmann et al, “Magnetic imaging of a buried SmCo layer in a spring magnet,” J. Appl. Phys., **89** (11) 7165-7167 (2001)

[44] J. A. Sidles et al, “Magnetic resonance force microscopy,” Rev. Mod. Phys., **67** (1), 249-265 (1995).

[45] M. Lederman, S. Schultz, and M. Ozaki, “Measurement of the dynamics of the magnetization reversal in individual single-domain ferromagnetic particles,” Phys. Rev. Lett. **73** (14), 1986-1989 (1994).

[46] R. H. Koch, G. Grinstein, G. A. Keefe, Y. Lu, P. L. Trouilloud, and W. J. Gallagher, “Thermally assisted magnetization reversal in submicron-sized magnetic thin films,” Phys. Rev. Lett. **84** (23), 5419-5422 (2000).

[47] C. H. Back, R. Allenspach, W. Weber, S. S. P. Parkin, D. Weller, E. L. Garwin, and H. C. Siegmann, “Minimum field strength in precessional magnetization reversal,” Science **285**, 864-867 (1999).

C. H. Back, D. Weller, J. Heidmann, D. Mauri, D. Guarisco, E. L. Garwin, and H. C. Siegmann, “Magnetization reversal in ultrashort magnetic field pulses,” Phys. Rev. Lett. **81** (15), 3251-3254 (1998).

H. C. Siegmann, E. L. Garwin, C. Y. Prescott, J. Heidmann, D. Mauri, D. Weller, R. Allenspach, and W. Weber, “Magnetism with picosecond field pulses,” J. Magn. Magn. Mater. **151**, L8-L12 (1995).

[48] M. Bauer, R. Lopusnik, J. Fassbender, and B. Hillebrands, “Magnetization reversal in ultrashort magnetic field pulses,” J. Magn. Magn. Mater. **218**, 165-176 (2000).

M. Bauer, J. Fassbender, B. Hillebrands, and R. L. Stamps, “Switching behaviour of a Stoner particle beyond the relaxation time limit,” Phys. Rev. B **61** (5), 3410-3416 (2000).

[49] H. Suhl, “Theory of the magnetic damping constant,” IEEE Trans. Magn. **34** (4), 1834-1838 (1998).

[50] T. J. Silva, C. S. Lee, T. M. Crawford, and C. T. Rogers, “Inductive measurement of ultrafast magnetization dynamics in thin-film permalloy, “J. Appl. Phys.**85** (11), 7849-7862 (1999).

T. J. Silva and T. M. Crawford, “Methods for determination of response times of magnetic head materials,” IEEE Trans. Magn. **35** (2), 671-676 (1999).

T.. M. Crawford, T. J. Silva, C. W. Teplin, and C. T. Rogers, “Subnanosecond magnetization dynamics measured by the seond-harmonic magneto-optic Kerr effect,” Appl. Phys. Lett. **74** (22), 3386-3388 (1999).

[51] V. L. Safonov and H. N. Bertram, “Magnetization reversal as a nonlinear multmode process,” J. Appl. Phys. **85** (8), 5072-5074 (1999).

[52] E. D. Boerner, H. N. Bertram, and H. Suhl, “Dynamic relaxation in thin films,” J. Appl. Phys. **87** (9), 5389-5391 (2000).

[53] W. K. Hiebert, A. Stankiewicz, M. R. Freeman, “Direct observation of magnetic relaxation in a small permalloy disk by time-resolved scanning Kerr microscopy,” Phys. Rev. Lett. **79** (6), 1134-1137 (1997).

M. R. Freeman, M. J. Brady, J. Smyth, “Extremely high frequency pulse magnetic resonance by picosecond magneto-optic sampling,” Appl. Phys. Lett. **60**, 2555-2557 (1992).

A. Stankiewicz, W. K. Hiebert, G. E. Ballentine, K. W. Marsh, and M. R. Freeman, “Dynamics of magnetization reversal in a 20x4 μm permalloy microstructure,” IEEE Trans. Magn. **134**, 1003-1005 (1998).

M. R. Freeman, W. K. Hiebert, and A. Stankiewicz, “Time-resolved scanning Kerr microscopy of ferromagentic structures (invited),” J. Appl. Phys. **83** (11), Part 2, 6217-6222 (1998).

A. Stankiewicz, W. K. Hiebert, G. E. Ballentine, and M. R. Freeman, “Time-resolved scanning Kerr microscopy in magnetic dynamics investigations,” Critical Reviews vol CR72, “Optical Metrology”, SPIE Optical Engineering Press. CR72: 181-210 (1999).

G. E. Ballentine, W. K. Hiebert, A. Stankiewicz, and M. R. Freeman, “Ultrafast microscopy and numerical simulation study of magnetization reversal dynamics in permalloy,” J. Appl. Phys. **87** (9), 6830-6832 (2000).

B. C. Choi, M. Belov, W. K. Hiebert, G. E. Ballentine, and M. R. Freeman, “Ultrafast magnetization reversal dynamics Investigated by time domain imaging,” Phys. Rev. Lett. **86** (4), 728-731 (2001).

[54] R. H. Koch, J. G. Deak, D. W. Abraham, P. L. Trouilloud, R. A. Altman, Y. Lu, W. J. Gallagher, R. E. Scheuerlein, K. P. Roche, and S. S. P. Parkin, “Magnetization reversal in micron-sized magnetic thin films,” Phys. Rev. Lett. **81** (20), 4512-4515 (1998).

[55] J. –C. Diels and W. Rudolph, *Ultrashort laser pulse phenomena*, Academic Press, San Diego, 1996.

W. Kaiser (ed.), *Topics in Applied Physics Vol 60 : Ultrashort Laser Pulses and Applications,* Springer-Verlag, New York (1988).

[56] M. Mansuripur, *The Physical Principles of Magneto-optical Recording*, Cambridge University Press, Cambridge, 1995.

[57] M.J.Freisen, IEEE Trans. Magn. **4** (2), 152 (1968).

---

[58] M. Mansuripur, J. Appl. Phys. **63** (12)**,** 5809-5823 (1988).

N. Hayashi, T. Inoue, Y. Nakatani, and H. Fukushima, IEEE Trans. Magn. **24** (6)**,** 3111-3113 (1988).

J. –G. Zhu and H. N. Bertram, “Micromagnetic studies of thin metallic films (invited),” J. Appl. Phys. **63** (8), 3248-3253 (1988).

B. Yang and D. R. Fredkin, J. Appl. Phys. **79** (8)**,** 5575-5577 (1996).

[59] P. Rhodes and G. Rowlands, “Demagnetizing energies of uniformly magnetized rectangular blocks,” Proc. Leeds Phil. Liter. Soc. **6**, 191-210 (1954)

[60] Y. Nakatani, Y. Uesaka and N. Hayashi, J. Appl. Phys., **28** (12), 2485-2507 (1989)

[61] R. D. McMichael, M. J. Donahoe and D. G. Porter, “Switching dynamics and critical behavior in standard problem No. 4,” J. Appl. Phys., **89**, 7603 (2001)

[62] H. Fukushima, Y. Nakatani and N. Hayashi, “Volume average demagnetizing tensor of rectangular prisms,” IEEE Trans. Magn., **34** (1), 193 (1998)

[63] Schrefl, T., Fidler, K., Kirk, K. J. & Chapman, J. N. J. Appl. Phys. 85 (8), 6169-6171 (1999).

[64] R. W. Brankin, I. Gladwell and L. F. Shampine, RKSUITE: a suite of Runge-Kutta codes for the initial value problerm for ODEs, Softreport 92-S1, Dept of Mathematics, Soutehrn Methodist University, Dallas, TX, 1992

[65] www.fftw.org

[66] information can be found at www.ctcms.nist.gov/%7Erdm/mumag.html

[67] including those of Jimmy Zhu (magsoft), Mike Scheinfein (LLG) and Bob McMichael (OOMMF)

[68] B. C. Choi, G. E. Ballentine, M. Belov and M. R. Freeman “Bias-field dependence of the spatiotemporal evolution of magnetization reversal in a mesoscopic $Ni_{80}Fe_{20}$ element,” Phys. Rev. B., **64** 144418 (2001)

[69] E. D. Dahlberg and J.-G. Zhu “Micromagnetic microscopy and modelling,” Physics Today **48** (4) 34-40 (1995)

[70] F.J.A. den Broeder, W. Hoving, P.H.J. Bloemen “Magnetic anisotropy of multilayers,” J. Magn. Magn. Matt., **93**, 562-570 (1991)

[71] A. E. Labonte, “Two dimensional Bloch-type domain walls in ferromagnetic film,” J. Appl. Phys., **40** 2450-2458 (1969)

K. Kosavisutte and N. Hayashi, “Acceleration of the micromagnetic calculation based on LaBonte’s iteration,” Jpn. J. Appl. Phys., **34** 5599-5605 (1995)

[72] F. Bloch, Phys. Rev. **70**, 460 (1946).

N. Bloembergen, Phys. Rev. **78**, 572 (1950).

[73] V. G. Bar’yakhtar, B. A. Ivanov, A. L. Sukstanskii, and E. Y. Melikhov, Phys. Rev. B **56** (2), 619 (1997).

E. G. Galkina, V. G. Bar’yakhtar, and K. A. Safaryan, JETP **84** (1), 87 (1997).

V. G. Bar’yakhtar, Sov. Phys. JETP **67** (4), 757 (1988).

V. G. Bar’yakhtar, Sov. Phys. Solid State **29** (5), 1754 (1987).

V. G. Bar’yakhtar, Sov. J. Low Temp. Phys. **11** (11), 662 (1985).

V. G. Bar’yakhtar, Sov. Phys. JETP **60** (4), 863 (1984).

[73] W.K. Hiebert, MSc thesis, University of Alberta, Canada (1998).

[74] D. H. Auston, “Picosecond optoelectronic switching and gating in silicon,” Appl. Phys. Lett., **26**, 101-103 (1975)

[75] A. Y. Elezzabi, M. R. Freeman and M. Johnson, “Direct measurement of the conduction electron spin-lattice relaxation time T_1 in gold,” Phys. Rev. Lett., **77** (15), 3220-3223 (1996).

[76] C. Kittel, “Theory of the structure of ferromagnetic domains in films and small particles,” Phys. Rev., **70**, 965-971 (1946)

[77] C. Kittel, *Introduction to Solid state Physics: Sixth Edition*, John Wiley and Sons, New York (1986)

[78] H. A. M. Van den Bergh and D. K. Vatvani, “Wall clusters in soft ferromagnetic configurations,” J. Appl. Phys., **52**, 6830-6839 (1981)

[79] H. Hoffman. IEEE Trans. Magn., **4**, 32 (1968)

[80] W. F. Brown. Phys. Rev., **130**, 1677 (1963)

[81] D. O. Smith in *Magnetism III* (eds. G. T. Rado and H. Suhl), Academic Press, New York (1963), p. 465-523.

[82] E. M. Gyorgy and F. B. Hagedorn, J. Appl. Phys. (Suppl.) **30** (4) 308S (1959)

[83] W. Scholz, Ph.D thesis 1999 Wein, Austria

---

[84] D. T. Gillespie, *Markov Processes: An Introduction for Physical Scientists*, Academic Press, New York (1992)

N. G. van Kampen, *Stochastic Processes in Physics and Chemistry*, Elsevier, Amsterdam (1989)

[85] W. Horstemke and R. Lefever, *Noise-Induced Transitions*, Springer, New York, (1984)

[86] H. B. Callen, M. L. Barasch and J. L. Jackson, Phys. Rev., **88**, 1382 (1952)

[87] L. Neel, Ann. Geophys., **5**, 99-136 (1949)

[88] J. A. H. Stotz and M. R. Freeman, "A stroboscopic scanning solid immersion lens microscope," Rev. Sci. Instrum., **68**, 4468-4477 (1997)

[89] C. L. Jahncke and H. D. Hallen, "A versatile, stable scanning proximal probe microscope," Rev. Sci. Instrum., **68**, 1759 (1997)

[90] M. R. Freeman, R. W. Hunt and G. M Steeves, "Noise imaging in stroboscopic ultrafast microscopy," Appl. Phys. Lett., **86**, 728 (2001)

M. R. Freeman, G. M. Steeves, G. E. Ballentine and A. Krichevsky, "Noise imaging using magneto-optical sampling techniques," to appear in J. Appl. Phys. May 15, 2002 issue

[91] R. W. Schoenlein et al, "Generation of femtosecond pulses of synchotron radiation," Science **287**, 2237-2240 (2000)

[92] A. T. Young, H. A. Padmore and N. V. Smith, " X-ray magnetic microscopy and spectroscopy using a third generation synchrotron radiation source," J. Vac. Sci. Tech B **14**, 3119-3125 (1996)

[93] S. Anders et al, "Photoemission electron microscope for the study of magnetic materials," Rev. Sci. Instrum, **70**, 3973-3981 (1999)

[94] H. Shinada et al, "Time-resolved measurement of micro-magnetic field by stroboscopic electron beam tomography," IEEE Trans. Magn., **28**, 3117-3121 (1992)

[95] A. D. Gavrin and J. Ungaris, "SEMPA imaging of domain dynamics in amorphous metals," J. Magn. Magn. Matt., **213**, 95-100 (2000)

[96] W. Wulfhekel and J. Kirschner, "Spin-polarized scanning tunnelling microscopy on ferromagnets," Appl. Phys. Lett., **75**, 1944-1946 (1999)

[97] Z.-P. Shi, W. K. Hiebert and M. R. Freeman, "Ultrafast laser diagnostics and modelling for high-speed recording heads," IEEE Trans. Magn., **35** (2), 632-636 (1999)